Universidade do Minho
Escola de Engenharia

Sandro Filipe Monteiro Queirós

Fast Fully Automatic Myocardial Segmentation in 4D cine Cardiac Magnetic Resonance datasets

Tese de Mestrado
Mestrado Integrado em Engenharia Biomédica

Trabalho realizado sob a orientação de:
Professor Doutor Jaime Francisco Cruz Fonseca
Professor Doutor Jan D'hooge

Setembro de 2013

Declaração

Nome: Sandro Filipe Monteiro Queirós

Endereço electrónico: sandroqueiros@ecsaude.uminho.pt

Telefone: (+351) 964954393

Número do Cartão de Cidadão: 13809146

Título da dissertação:

Fast Fully Automatic Myocardial Segmentation in 4D cine Cardiac Magnetic Resonance datasets

Segmentação Rápida e Automática do Miocárdio em sequências 4D de Ressonância Magnética Cardíaca

Orientadores:

Professor Doutor Jaime Francisco Cruz Fonseca

Professor Doutor Jan D'hooge

Ano de conclusão: 2013

Designação do Mestrado: Mestrado Integrado em Engenharia Biomédica

É AUTORIZADA A REPRODUÇÃO PARCIAL DESTA TESE, APENAS PARA EFEITOS DE INVESTIGAÇÃO, MEDIANTE DECLARAÇÃO ESCRITA DO INTERESSADO, QUE A TAL SE COMPROMETE.

Universidade do Minho, _____/_____/_____

Assinatura: ____

Acknowledgements/Agradecimentos

"*Audaces fortuna juvat*"

This thesis represents the end of a journey in my life, during which I learnt, lived and grown as person. Over the past five years, I had the opportunity to share knowledge and experiences with an amazing group of people, to whom I wish to express my most sincere gratitude.

Esta tese representa o fim de uma etapa na minha vida, durante a qual muito aprendi, vivi e cresci como pessoa. Ao longo dos últimos 5 anos, tive a oportunidade de partilhar conhecimento e experiências com um extraordinário grupo de pessoas, aos quais quero manifestar o meu mais sincero agradecimento.

To Prof. Dr. Jan D'hooge from the Medical Image Research Center (MIRC), Leuven, Belgium, I express my sincere gratitude for giving me the opportunity to join him and his team during a great part of my thesis. I am grateful for his continuous support, guidance, motivation and immense knowledge, as well as his confidence in me and in my work.

Ao Daniel Barbosa, pela supervisão diária, incentivo e entusiasmo no meu projeto. Daniel, obrigado pela tua disponibilidade, pelas horas infindáveis de *brainstorming*, pela boa disposição e pelo apoio (e muita paciência!). Agradeço por abdicares do teu tempo em prol da minha tese, esta não teria o mesmo valor se não fosse pela tua constante ajuda.

Ao Prof. Doutor João Vilaça, estou-lhe grato pela oportunidade de trabalhar no "*ICVS Engineering group*" ao longo destes últimos 3 anos. Obrigado por ter acreditado em mim e pelas diversas oportunidades, que, sem dúvida, me fizeram crescer pessoalmente e profissionalmente. Obrigada pelos conselhos, pela ajuda e pela disponibilidade demonstrada ao longo destes anos.

Ao Prof. Doutor Jaime Fonseca, agradeço-lhe a sua orientação, o seu apoio e a sua sempre disponibilidade ao longo das diferentes fases da minha tese. Quero também agradecer-lhe a sua prontidão quando foi necessário marcar a defesa da tese tão apressadamente.

To Brecht Heyde, I want to thank his support, insightful comments and remarks during our weekly meetings and T-confs. I extend my appreciation to many other people in MIRC, for their friendship and good mood.

Ao Pedro Morais, pela amizade e companheirismo, pelo debate de ideias e pela disponibilidade para ajudar ao longo de toda a tese. Aos restantes colegas de casa, pelo convívio e suporte ao longo da nossa estadia em Leuven, bem como pela enorme quantidade de risos que geraram boa disposição. Aos meus colegas de gabinete, António, Pedro, João, Spranger, Nuno e Mafalda, pelo apoio, pelo espírito de grupo e pelos momentos de descontração.

A todos os meus professores de curso, pelos vastos conhecimentos e ensinamentos que me permitem hoje ser aquilo que sou, um futuro Engenheiro Biomédico. Aos meus colegas e amigos de curso, pelo companheirismo, espírito de entreajuda e convívio ao longo dos últimos 5 anos.

Aos meus pais e irmãos, agradeço todo o apoio e carinho inestimáveis. Agradeço-lhes os esforços que me proporcionaram estar hoje a terminar um curso, mas também a compreensão pelas noites, fim de semanas e feriados “perdidos” para que eu pudesse estudar, trabalhar e alcançar os resultados dos quais espero que se orgulhem. A toda a minha família mais próxima, agradeço a preocupação, o apoio e a ajuda dada nas diferentes etapas da minha vida pessoal e académica.

Por fim, devo a mais profunda gratidão à Céline, pela ajuda, pelo apoio e motivação, pela enorme paciência e compreensão, e por acreditar sempre nas minhas capacidades e me incentivar a dar o máximo de mim. Céline, obrigado por seres um alicerce na minha vida!

A todos, o meu sincero muito OBRIGADO!

Summary

Cardiovascular diseases (CVDs) are the leading cause of death in the world, representing 30% of all global deaths. Among others, assessment of the left ventricular (LV) morphology and global function using non-invasive cardiac imaging is an interesting technique for diagnosis and treatment follow-up of patients with CVDs. Nowadays, cardiac magnetic resonance (CMR) imaging is the gold-standard technique for the quantification of LV volumes, mass and ejection fraction, requiring the delineation of endocardial and epicardial contours of the left ventricle from cine MR images. In clinical practice, the physicians perform this segmentation manually, being a tedious, time consuming and unpractical task. Even though several (semi-)automated methods have been presented for LV CMR segmentation, fast, automatic and optimal boundaries assessment is still lacking, usually requiring the physician to manually correct the contours.

In the present work, we propose a novel fast fully automatic 3D+time LV segmentation framework for CMR datasets. The proposed framework presents three conceptual blocks: 1) an automatic 2D mid-ventricular initialization and segmentation; 2) an automatic stack initialization followed by a 3D segmentation at the end-diastolic phase; and 3) a tracking procedure to delineate both endo and epicardial contours throughout the cardiac cycle. In each block, specific CMR-targeted algorithms are proposed for the different steps required. Hereto, we propose automatic and feasible initialization procedures. Moreover, we adapt the recent B-spline Explicit Active Surfaces (BEAS) framework to the properties of CMR image segmentation by integrating dedicated energy terms and making use of a cylindrical coordinate system that better fits the topology of CMR data. At last, two tracking methods are presented and compared.

The proposed framework has been validated on 45 4D CMR datasets from a publicly available database and on a large database from an ongoing multi-center clinical trial with 318 4D datasets. In the technical validation, the framework showed competitive results against the state-of-the-art methods, presenting leading results in both accuracy and average computational time in the common database used for comparative purposes. Moreover, the results in the large scale clinical validation confirmed the high feasibility and robustness of the proposed framework for accurate LV morphology and global function assessment. In combination with the low computational burden of the method, the present methodology seems promising to be used in daily clinical practice.

Resumo

As doenças cardiovasculares (DCVs) são a principal causa de morte no mundo, representando 30% destas a nível global. Na prática clínica, uma técnica empregue no diagnóstico de pacientes com DCVs é a avaliação da morfologia e da função global do ventrículo esquerdo (VE), através de técnicas de imagiologia não-invasivas. Atualmente, a ressonância magnética cardíaca (RMC) é a modalidade de referência na quantificação dos volumes, massa e fração de ejeção do VE, exigindo a delimitação dos contornos do endocárdio e epicárdio a partir de imagens dinâmicas de RMC. Na prática clínica diária, o método preferencial é a segmentação manual. No entanto, esta é uma tarefa demorada, sujeita a erro humano e pouco prática. Apesar de até à data diversos métodos (semi)-automáticos terem sido apresentados para a segmentação do VE em imagens de RMC, ainda não existe um método capaz de avaliar idealmente os contornos de uma forma automática, rápida e precisa, levando a que geralmente o médico necessite de corrigir manualmente os contornos.

No presente trabalho é proposta uma nova *framework* para a segmentação automática do VE em imagens 3D+tempo de RMC. O algoritmo apresenta três blocos principais: 1) uma inicialização e segmentação automática 2D num corte medial do ventrículo; 2) uma inicialização e segmentação tridimensional no volume correspondente ao final da diástole; e 3) um algoritmo de *tracking* para obter os contornos ao longo de todo o ciclo cardíaco. Neste sentido, são propostos procedimentos de inicialização automática com elevada robustez. Mais ainda, é proposta uma adaptação da recente *framework “B-spline Explicit Active Surfaces”* (BEAS) com a integração de uma energia específica para as imagens de RMC e utilizando uma formulação cilíndrica para tirar partido da topologia destas imagens. Por último, são apresentados e comparados dois algoritmos de *tracking* para a obtenção dos contornos ao longo do tempo.

A *framework* proposta foi validada em 45 *datasets* de RMC provenientes de uma base de dados disponível ao público, bem como numa extensa base de dados com 318 *datasets* para uma validação clínica. Na avaliação técnica, a *framework* proposta obteve resultados competitivos quando comparada com outros métodos do estado da arte, tendo alcançado resultados de precisão e tempo computacional superiores a estes. Na validação clínica em larga escala, a *framework* provou apresentar elevada viabilidade e robustez na avaliação da morfologia e função global do VE. Em combinação com o baixo custo computacional do algoritmo, a presente metodologia apresenta uma perspetiva promissora para a sua aplicação na prática clínica diária.

Contents

Acknowledgements/Agradecimentos iii

Summary v

Resumo vii

Abbreviations xiii

Figures list xv

Tables list xviii

1. Introduction 3

    1.1 Anatomy and physiology of the heart 3

    1.2 Cardiovascular diseases 7

    1.3 Non-invasive Cardiovascular imaging 10

        1.3.1 Ultrasound imaging 10

        1.3.2 Magnetic resonance imaging 11

        1.3.3 Computed Tomography 12

        1.3.4 Nuclear imaging 13

    1.4 Quantification of cardiac function 13

    1.5 Motivation 17

    1.6 Aims and contributions 18

    1.7 Thesis Overview 19

2. Cardiac Segmentation 23

    2.1 Computed-assisted manual contouring in CMR datasets 23

    2.2 (Semi-)Automated CMR segmentation 26

        2.2.1 Image-based methods 27

        2.2.2 Pixel classification methods 28

        2.2.3 Deformable models 29

        2.2.4 Shape-prior based deformable models 30

2.2.5 Active Shape and Appearance Models 30

2.2.6 Atlas-guided segmentation 31

2.2.7 Automatic localization of the heart and left ventricle 32

2.3 Commercial Software Packages 33

2.4 B-spline Explicit Active Surfaces (BEAS) 34

3. Methodology 39

3.1 General Overview 39

3.2 Automatic Mid-ventricular Initialization 40

3.2.1 LV Localization 40

3.2.2 Elliptical Annular Template Matching Algorithm 42

3.3 Coupled Myocardial 2D Segmentation 43

3.3.1 Endocardial and Epicardial Contour Coupling 44

3.3.2 2D Region-based Energy Functional 44

3.4 Automatic Stack Initialization 48

3.5 Coupled Myocardial 3D Segmentation 51

3.5.1 BEAS 3D Extension 51

3.5.2 3D Hybrid Energy Functional 52

3.6 3D+time Tracking 55

3.6.1 BEAS Profile Matching 56

3.6.2 Anatomical Affine Optical Flow 58

3.7 Implementation Details 61

3.7.1 BEAS Contours’ Evolution 61

3.7.2 Segmentation parameters 61

4. Results 67

4.1 Data 67

4.2 Evaluation Metrics 67

4.3 Automatic Mid-ventricular Initialization 69

4.4 Coupled Myocardial 2D Segmentation 71

4.5 Coupled Myocardial 3D Segmentation 73

4.6 3D+time Tracking 76

5. Discussion 83

5.1 Automatic Mid-ventricular Initialization 83

5.2 Coupled Myocardial 2D Segmentation 84

5.3 Coupled Myocardial 3D Segmentation 85

5.4 3D+time Tracking 87

5.5 Preliminary conclusions.. 90

6. Clinical Validation 93

6.1 Data 94

6.2 Experiments... 94

6.2 Results 94

6.3 Discussion 100

6.3.1 Feasibility study 100

6.3.2 Segmentation Accuracy... 101

6.3.3 Clinical indices validation 102

7. Main Conclusions... 107

References... 111

Appendixes 123

Appendix A: Combined global and local region-based energy................................ 123

Appendix B: Influence of energy features in 3D segmentation accuracy 124

Appendix C: Sensitivity Analysis 126

Abbreviations

1D	one-dimensional
2D	two-dimensional
3D	three-dimensional
4D	four-dimensional
AAMs	Active Appearance Models
AGFs	Active Geometric Functions
APD	average perpendicular distance
ASMs	Active Shape Models
BEAS	B-spline Explicit Active Surfaces
BEASPM	BEAS Profile Matching
bpm	beats per minute
CC	customized evaluation code
CHD	Coronary Heart Diseases
CMR	Cardiac Magnetic Resonance
CO	cardiac output
CPU	Central Processing Unit
CT	Computed Tomography
CVDs	Cardiovascular Diseases
DALYs	disability-adjusted life years
DCVs	"Doenças Cardiovasculares"
DP	Dynamic Programming
ECG	electrocardiogram
ED	end-diastole
EDV	end-diastolic volume
EF	ejection fraction
EM	Expectation-Maximization
ES	end-systole
ESV	end-systolic volume
GMM	Gaussian Mixture Model
GPU	Graphics Processing Unit
GVF	Gradient Vector Flow
HF	Heart failure
HF-I	patients with heart failure and myocardial infarction
HF-NI	patients with heart failure without myocardial infarction
HIV/AIDS	Human Immunodeficiency Virus infection/Acquired Immunodeficiency Syndrome
HR	heart rate
HYP	patients with hypertrophic cardiomyopathy
LA	left atrium
LAX	long-axis
LCV	localized Chan-Vese
LOA	limits of agreement
LV	left ventricle
LVM	left ventricular mass
LVOT	left ventricular outflow tract

LY	localized Yezzi
MATLAB	MATrix LABoratory
MM	Mathematical Morphological
MR	Magnetic Resonance
MRI	Magnetic Resonance Imaging
myoGL	combined global and local region-based energy
N	normal subjects
NRR	non-rigid registration
OC	original evaluation code
OFT	Optical Flow Tracking
PET	Positron Emission Tomography
PVE	partial volume effects
RA	right atrium
RMC	"Ressonância Magnética Cardíaca"
ROI	region of interest
RV	right ventricle
SAD	sum of absolute differences
SAX	short-axis
SLY	signed localized Yezzi
SPECT	Single Photon Emission Computed Tomography
SSFP	Steady-State Free Precession
SV	stroke volume
TPMs	trabeculae and papillary muscles
US	ultrasound
VE	"ventrículo esquerdo"
WHO	World Health Organization

Figures list

Figure 1.1 - Internal heart anatomy [1]........ 3

Figure 1.2 - (A) Heart wall and pericardium. (B) Transverse view of ventricular walls showing difference in myocardial thickness (adapted from [3]). 4

Figure 1.3 - Conduction system of the heart [1]........ 5

Figure 1.4 - (A) Stages of the cardiac cycle [1]. (B) Electrocardiogram trace of a cardiac cycle (adapted from [4])........ 6

Figure 1.5 - World distribution of estimated age-standardized mortality rate due to cardiovascular diseases and diabetes, by 2008 [13]........ 9

Figure 1.6 - Steady-state free precession (SSFP) cardiac magnetic resonance (CMR) images in: (A) two-chamber long-axis (LAX); (B) four-chamber LAX; and (C) short-axis (SAX) views. 11

Figure 1.7 - 17-segment frame of references used for LV division. 16

Figure 2.1 - An example manual contouring of endocardial and epicardial contours in all slices covering the LV, from the atrioventricular ring to the apex, in the end-diastolic phase...... 23

Figure 2.2 - Different methodologies for endocardial contouring........ 24

Figure 2.3 - Left ventricle shape and thickness variability at mid-ventricular slice across patients. 26

Figure 2.4 - Overview of the evolution towards B-spline Explicit Active Surfaces (BEAS). 36

Figure 3.1 - General overview of the proposed fully automatic 3D+time myocardial segmentation framework for CMR datasets........ 39

Figure 3.2 - LV localization algorithm proposed by Lu *et al.* [67]. 41

Figure 3.3 - Proposed LV localization algorithm. 42

Figure 3.4 - Annular template matching algorithm. 43

Figure 3.5 - Conceptual diagram of the coupled formulation used to represent both endo and epicardial contours [118]. 44

Figure 3.6 - Principle of localized region-based energies. 45

Figure 3.7 - Principle of the proposed weighted localized region-based energies........... 47

Figure 3.8 - Proposed automatic stack initialization procedure. 49

Figure 3.9 - Principle of threshold-based BEAS to obtain coarse endo and epicardial delineations. 50

Figure 3.10 - Misalignment correction based on the LV cavity's center estimated during stack initialization. 52

Figure 3.11 - Endocardial LV 3D-surface representation through an explicit function in the cylindrical domain.......... 53

Figure 3.12 - Edge map computation for hybrid epicardial energy functional. 54

Figure 3.13 - Principle of BEAS Profile Matching (BEASPM) methodology for LV tracking. 57

Figure 3.14 - Effect of contours' subsampling in analyzed region of interest for motion estimation. 60

Figure 4.1 - Evaluation metrics used for segmentation performance assessment. 68

Figure 4.2 - Comparison between proposed LV localization procedure and method in [67] for datasets N-7 and HF-NI-15.......... 69

Figure 4.3 - Automatic template matching initialization and segmentation result for the proposed energy in two mid-ventricular SAX images (from datasets HF-NI-13 and HYP-3).......... 70

Figure 4.4 - LV localization and elliptical template matching limitations. 71

Figure 4.5 - 2D segmentation results for (A)-(D) the chosen benchmark energy from [98] and (E)-(F) the proposed modified energy functional in 4 example mid-ventricular SAX images. 72

Figure 4.6 - Segmentation results for 8 mid-ventricular SAX images, after automatic initialization. 73

Figure 4.7 - Segmentation results for 8 mid-ventricular SAX images, after manual initialization. 73

Figure 4.8 - Boxplots of computed (A) Dice metric, (B) APD and (C) Hausdorff distance for both endo and epicardial contours using the proposed automatic 3D segmentation (# = 45). 74

Figure 4.9 - Boxplots for APD and Hausdorff metrics distribution from basal to apical slices using the proposed automatic 3D segmentation (# = 45). 75

Figure 4.10 - Automatic 3D segmentation results for three example CMR datasets. 75

Figure 4.11 - 3D LV surface from the three datasets presented in Figure 4.10. 76

Figure 4.12 - Automatic 3D+time segmentation result using BEAS profile matching (BEASPM) and global optical flow method (OFT) for an example CMR dataset. 77

Figure 4.13 - 3D LV surface evolution from ED phase to ES phase using global optical flow method for an example CMR dataset.......... 78

Figure 4.14 - Complete 3D LV surface evolution using global optical flow method for an example CMR dataset. 78

Figure 4.15 - Linear regression for (A) end-diastolic volume (EDV); (B) end-systolic volume (ESV); (C) left ventricular mass (LVM); and (D) ejection fraction (EF) using BEAS profile matching. 79

Figure 4.16 - Bland-Altman analysis for (A) end-diastolic volume (EDV); (B) end-systolic volume (ESV); left ventricular mass (LVM); and (D) ejection fraction (EF) using BEAS profile matching. 80

Figure 6.1 - Left ventricle variability at mid-ventricular slice across subjects in the clinical trial data. 93

Figure 6.2 - Causes of incorrect analysis of datasets in the clinical trial database. 95

Figure 6.3 - Boxplots of computed (A) Dice metric, (B) APD and (C) Hausdorff distance for both endo and epicardial contours using the proposed 3D+time framework (# = 302). 96

Figure 6.4 - Boxplots for APD and Hausdorff metrics distribution from basal to apical slices using the proposed automatic 3D+time framework (# = 302). 96

Figure 6.5 - Automatic 3D segmentation results for 3 CMR datasets from the clinical trial database. 97

Figure 6.6 - Automatic 3D+time segmentation and tracking result using global optical flow method for dataset 5192 from the clinical trial database. 97

Figure 6.7 - Automatic 3D+time result for dataset 6509 from the clinical trial database. 98

Figure 6.8 - Complete 3D LV surface evolution for dataset 5050 from the clinical trial database. 98

Figure 6.9 - Complete 3D LV surface evolution for dataset 5145 from the clinical trial database. 98

Figure 6.10 - Linear regression for (A) end-diastolic volume (EDV); (B) end-systolic volume (ESV); (C) left ventricular mass (LVM); and (D) ejection fraction (EF). 99

Figure 6.11 - Bland-Altman analysis for (A) end-diastolic volume (EDV); (B) end-systolic volume (ESV); left ventricular mass (LVM); and (D) ejection fraction (EF). 99

Figure A.1 - Influence of the variation of 8 parameters in the 3D segmentation performance. 127

Tables list

Table 4.1 - 2D Segmentation performance for endo and epicardium (# = 41, $\mu \pm \sigma$).... 72

Table 4.2 - 3D segmentation performance for endo and epicardium (# = 45, $\mu \pm \sigma$).... 74

Table 4.3 - 3D+time segmentation performance for endo and epicardial contours using BEAS profile matching, categorized by pathology and average result (# = number of datasets, $\mu \pm \sigma$)........ 77

Table 4.4 - 3D+time segmentation performance for endo and epicardial contours using global optical flow tracking, categorized by pathology and average results (# = number of datasets, $\mu \pm \sigma$)........ 77

Table 4.5 - Comparison of segmentation performance between proposed approaches and state-of-the-art (# = number of datasets)........ 78

Table 4.6 - Average computational time for each step of the proposed approach (# = 45, $\mu \pm \sigma$)........ 79

Table 4.7 - Linear regression and Bland-Altman analysis for clinical cardiac indices for both tracking methodologies (# = 45)........ 79

Table 6.1 - 3D+time segmentation performance for endo and epicardial contours for the clinical trial database (# = 302, $\mu \pm \sigma$)........ 95

Table 6.2 - Linear regression and Bland-Altman analysis for the clinical indices studied (# = 302)........ 99

Table A.1 - 2D Segmentation performance for endo and epicardium with multiple combinations of the proposed features in the energy functional (# = 41, $\mu \pm \sigma$)........ 124

Table A.2 - 3D Segmentation performance for endo and epicardium with multiple combinations of the proposed features in the energy functional (# = 45, $\mu \pm \sigma$)........ 125

1. INTRODUCTION

1. Introduction

1.1 Anatomy and physiology of the heart

The heart is a hollow, cone-shaped muscular organ designed to pump the blood throughout the blood vessels to the entire body [1]. Although its relatively small size (roughly the size of a closed fist) and weight (an average mass of 250g in adult females and 300g in adult males), the heart is able to contract an estimate of 42 million times a year and pumps 2.5 million liters of blood during this period [1, 2]. This important organ is located in the thoracic cavity between lungs in the mediastinum, resting in a tilted position on the diaphragm, with its base (broad superior end) pointing toward the right shoulder and its apex (pointed inferior end) pointing to the left hip [1-3].

Besides pumping the blood through the systemic and pulmonary vascular systems, the heart is responsible for regulating the blood supply according to the current body needs and for keeping the oxygenated blood separated from deoxygenated one [1]. To accomplish its goal, the heart is divided in four chambers: two ventricles and two atria [Figure 1.1]. The atria contract simultaneously and send blood into adjacent ventricles, which are then responsible for pumping it to the main vessels that will deliver it to the body organs. Between the two atria and the two ventricles are the muscular interatrial and interventricular septums, respectively [1-3].

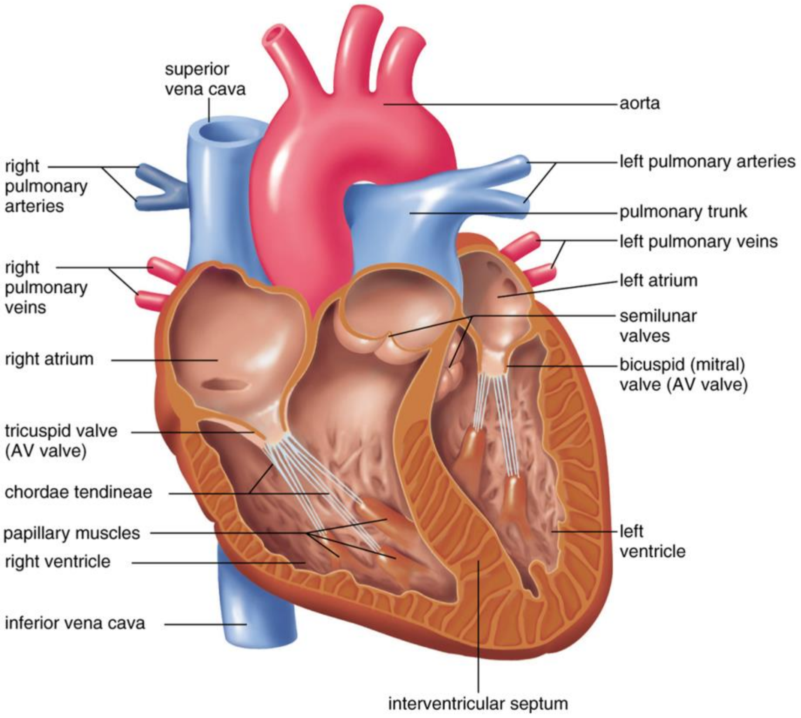
superior vena cava
aorta
right pulmonary arteries
left pulmonary arteries
pulmonary trunk
left pulmonary veins
right pulmonary veins
left atrium
semilunar valves
right atrium
bicuspid (mitral) valve (AV valve)
tricuspid valve (AV valve)
chordae tendineae
papillary muscles
left ventricle
right ventricle
inferior vena cava
interventricular septum

Figure 1.1 - Internal heart anatomy [1].

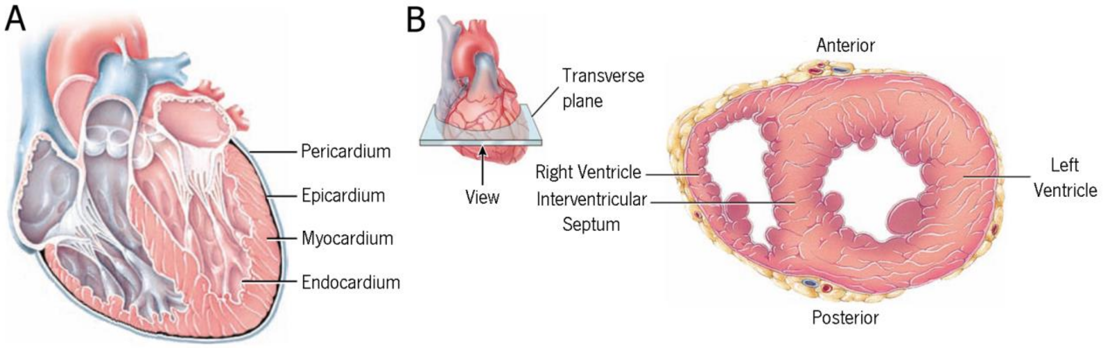

Figure 1.2 - (A) Heart wall and pericardium. (B) Transverse view of ventricular walls showing difference in myocardial thickness (adapted from [3]).

The heart is enclosed by a two-layered membrane, the pericardium [Figure 1.2A], which are separated by a thin film of lubricating serous fluid. The outer layer, the parietal pericardium, anchors the heart to the wall of the mediastinum, while allowing enough freedom for its fast contraction. The inner layer, called visceral pericardium, forms the outer surface of the heart, also designated as epicardium [1, 3, 4]. Regarding the heart wall, it is formed by three distinct layers [Figure 1.2A], namely the epicardium (external layer), the myocardium (muscular middle layer) and the endocardium (inner layer) [1-4]. The myocardium consists of the cardiac muscle tissue and represents 95% of the heart, being responsible for its ability to contract and for its pumping function [3]. The myocardial thickness varies accordingly to the required contraction force for blood ejection [Figure 1.2B]. Thus, it is thicker in the left ventricle and thinner around the atria [1, 2]. Finally, the endocardium is a thin layer of endothelium and covers the heart chambers and valves [1-3].

The cardiovascular system is divided in two main circuits: the pulmonary circuit and the systemic circuit [Figure 1.1]. The first relates to the blood oxygenation, while the second delivers blood rich in oxygen to different body organs [1-4]. In this sense, the right atrium (RA) receives blood from three veins, namely the superior and inferior vena cavas and coronary sinus, and passes it to the right ventricle (RV) through the tricuspid valve (with three leaflets). The RV is filled and then contracts to eject the blood through the pulmonary valve into the two pulmonary arteries. After oxygenation, the blood enters the heart again from the pulmonary veins into the left atrium (LA), which then transfers it to the left ventricle (LV) through the bicuspid (mitral) valve (with two leaflets). The LV is responsible for the main contraction, pumping the blood through the aortic valve into the ascending aorta for further delivery [1-3]. In both ventricles, conical muscular projections of the myocardium, called papillary muscles, are responsible for securing the chordae

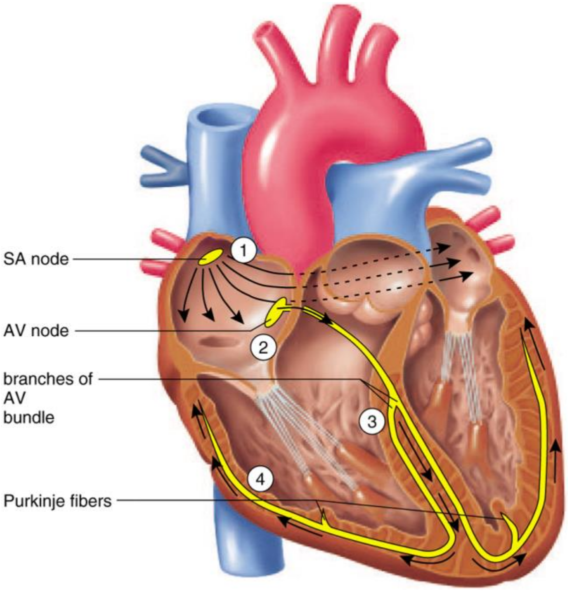

Figure 1.3 - Conduction system of the heart [1].

tendineae that held each valvular cusp in position [1, 3]. The heart perfusion itself is performed by the coronary circulation, of critical importance as it is related with heart attacks.

The heart's pumping behavior is a coordinated sequence of events controlled by the conduction system of the heart, which is intrinsic to it [1-4]. In other words, the heart presents self-excitable cardiac cells capable of generating a contraction rhythm without the need for external nervous stimulation [1, 2]. The conduction system consists of specialized fibers that generate and distribute electrical impulses through the heart and stimulate the contraction of the atria and ventricles [Figure 1.4]. The cardiac impulse is automatically generated in the sinoatrial node at a given rate, the heart rate (HR), and is propagated through the atria, causing their simultaneous contraction and forcing the blood to pass into the ventricles. After reaching the atrioventricular node in the base of the right atrium, the impulse is slightly delayed, allowing the atrial contraction to finish before ventricular excitation occurs. After this delay, the impulse is conducted through the two branches of the atrioventricular bundle until it reaches the Purkinje fibers. Both are responsible for the contraction of the ventricles, which occurs almost simultaneously, slightly earlier in the apex and spreading upward to eject the blood out of the ventricles into the arteries [1-5].

The cardiac cycle is controlled by this cyclic pattern of excitations and depolarizations, which is repeated approximately every 0.85s, leading to a normal HR of about 70 beats per minute (bpm). A normal adult HR can vary between 60 to 100 bpm [1]. The cardiac cycle can be described in three phases based on its electrical behavior [Figure 1.4A], using the terms systole (contraction of heart muscle) and diastole (relaxation of heart muscle) [1, 3]. The first phase

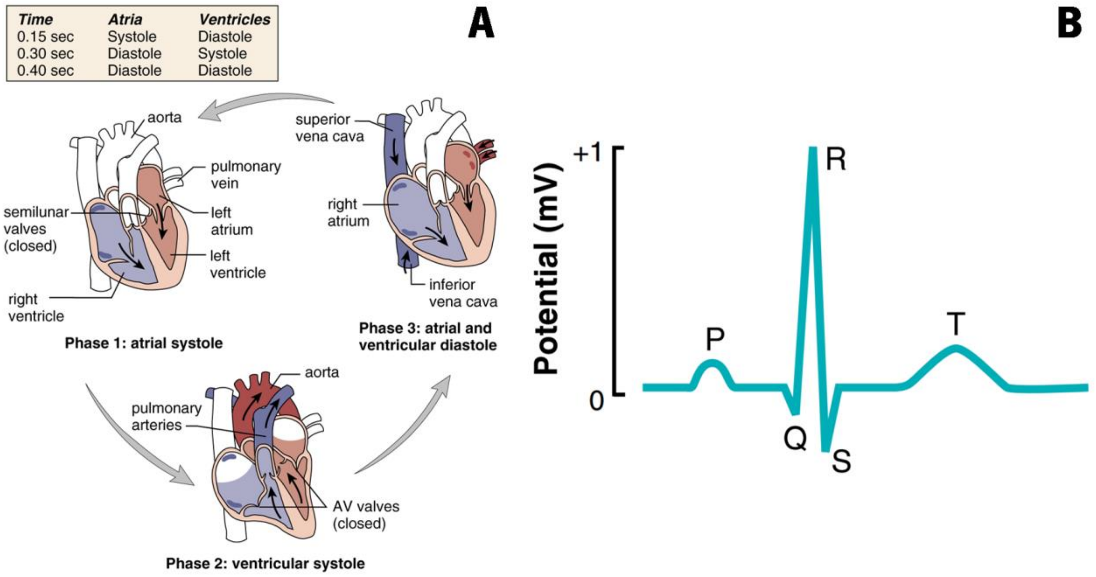
A
B
Time
Atria
Ventricles
0.15 sec
Systole
Diastole
0.30 sec
Diastole
Systole
0.40 sec
Diastole
Diastole
aorta
pulmonary vein
semilunar valves (closed)
left atrium
left ventricle
right ventricle
Phase 1: atrial systole
superior vena cava
right atrium
inferior vena cava
Phase 3: atrial and ventricular diastole
aorta
pulmonary arteries
AV valves (closed)
Phase 2: ventricular systole
Potential (mV)
+1
0
P
Q
R
S
T

Figure 1.4 - (A) Stages of the cardiac cycle [1]. (B) Electrocardiogram trace of a cardiac cycle (adapted from [4]).

corresponds to the atrial systole and lasts 0.15s. During this stage, the remaining blood in the atria is ejected into the ventricles. Thus, both atrioventricular valves are open and the semilunar valves are closed. The second phase is the ventricular systole and lasts about 0.30s. During this stage, the isovolumetric contraction of both ventricles occurs while the atria are in diastole (relaxed). The blood is ejected from the ventricles to the arteries through the open semilunar valves, and retrograde flow is avoided by closing the atrioventricular valves. Finally, the third and last phase corresponds to the atrial and ventricular diastole (lasts 0.40s), all four chambers are relaxed and the blood fills the atria and flows passively into the ventricles. Again, both atrioventricular valves are open to allow communication between corresponding atrium and ventricle, while the semilunar valves are closed [1, 3, 4].

The described electrical phenomenon is responsible for an electrical current flowing through the myocardium, which can be recorded in an electrocardiogram (ECG) trace [1-6]. This record helps the physician to evaluate the electrical activity of the heart, allowing him to detect possible irregular heartbeats, such as arrhythmias. The recording is possible by using several skin electrodes placed in known locations on the limbs and chest [5, 6]. A typical normal ECG has three deflections [Figure 1.4B], the P wave (atrial depolarization), the QRS complex (ventricular depolarization) and the T wave (ventricular repolarization) [1-6]. Although abnormal electrical activity can be detected and diagnosed, an ECG doesn't give any information regarding the mechanical activity of the heart as it doesn't affect its electrical behavior [4].

1.2 Cardiovascular diseases

Cardiovascular diseases (CVDs) include all anomalies of the heart and circulatory system, such as coronary heart diseases (CHD), cerebrovascular accident (or stroke), congenital heart defects (a defect present at birth), cardiomyopathies (typically associated with progressive thickening and stiffening of the myocardium), arrhythmias (heart rhythm disorder), valvular heart diseases, rheumatic heart diseases (damage to heart muscle and valves due to rheumatic fever), among others [6-9].

Heart failure (HF) is, by definition, "a clinical syndrome that occurs in patients who, because of inherited or acquired abnormality of cardiac structure and/or function, develop a constellation of clinical symptoms (dyspnea and fatigue) and signs (edema and rales) that lead to frequent hospitalizations, poor quality of life and shortened life expectancy" [6]. In practice, HF corresponds to the loss of pumping efficiency by the heart, making it unable to maintain blood flow to meet the required body needs [3, 6, 9]. By decreasing its pumping efficiency, there is an accumulation of blood in the ventricles at the end of each cycle and gradually the end-diastolic volume (EDV - Section 1.4) increases [3]. Such increase is responsible for the overstretching of the heart, which eventually starts contracting less forcefully and can compromise the fraction of blood that is ejected during one cardiac cycle (i.e., the ejection fraction, EF - Section 1.4) [3, 6]. Therefore, this conditions can be associated with a depressed ejection fraction (<40, also referred as systolic failure) or a preserved ejection fraction (>40-50%, also referred as diastolic failure or heart failure with normal ejection fraction). Among the several causes of HF, the first type can be associated with CHD, non-ischemic dilated cardiomyopathy, toxic/drug-induced damage or arrhythmias. The second type includes pathological hypertrophy, restrictive cardiomyopathy or, simply, aging [6]. Despite recent advances in healthcare, HF is still associated with poor prognosis, with 30-40% of patients dying within 1 year after diagnosis and 60-70% within 5 years [6].

CHD is the predominant cause of HF and is responsible for 60-75% of all cases, commonly also associated with hypertension [6]. CHD results from the effects of the accumulation of atherosclerosis plaques (cholesterol and fatty deposits) on the inner walls of the coronary arteries, reducing the blood supplied to the myocardium [3, 6, 9]. As a result of these deposits, a partial obstruction occurs, limiting blood flow into the myocardium and the patient acquires myocardial ischemia. Such condition can be asymptomatic, having no prior notice of an impending heart attack. A heart attack, also known as myocardial infarction, is related with a complete obstruction of blood flow in a coronary artery. The term infarct is associated with partial tissue death due to interrupted blood supply, resulting in a loss of muscle strength due to the myocardial tissue death and replacement by noncontractile scar tissue [3, 6, 9]. Both myocardial ischemia and infarction can normally be detected by the evaluation of the heart structure and function, namely by the detection of a reduced ejection fraction [6].

Cardiomyopathy is a progressive disorder in which ventricular structure or function is impaired due to an abnormality in the heart muscle, usually enlarged, thickened and/or stiffened [3, 6, 9]. In non-ischemic dilated cardiomyopathy, the most common form of cardiomyopathy, the ventricles are enlarged and stretched (dilated), becoming weaker and slowing their pumping action. In hypertrophic cardiomyopathy, the wall thickens and hence the myocardial mass increases, again diminishing the pumping efficiency of the affected ventricle. However, the ventricle contraction is largely normal, which results in a normal ejection fraction [3, 6].

Concerning valvular heart diseases, any disease involving a valve of the heart is included and the two most common disorders are valve stenosis (narrowing and blood flow restriction) and valve insufficiency (also referred as regurgitation and associated with an incomplete closing of the affected valve) [3, 6, 9]. Among these diseases, some are associated with a reduced left ventricular EF, namely aortic valve stenosis and aortic insufficiency, both linked with a disorder in the communication between left ventricle and aorta [6, 9].

The most relevant behavioral risk factors for CVDs include tobacco use, insufficient physical activity, unhealthy diet and harmful use of alcohol [6, 7, 10]. Regarding metabolic risk factors, high cholesterol levels, hypertension, obesity and diabetes mellitus are among the most relevant factors for CVD death rates. In fact, it is estimated that 4.4 million deaths annually are related with cholesterol levels and 7 million with hypertension [6]. The change in diet habits (consumption of fruits and vegetables), regular physical activity, cessation of tobacco use and responsible consumption of alcohol have been shown to reduce the risk of cardiovascular diseases. Moreover, by preventing or treating hypertension, diabetes and raised blood lipids, the risk for CVDs can also be reduced [6, 7].

Cardiovascular diseases are the leading cause of death in the world [7, 10-12]. According to the World Health Organization (WHO), an estimated 17.3 million people died from CVDs in 2008, which represent 30% of all global deaths [7, 10]. Among these, 7.3 million deaths were due to CHD and 6.2 million due to stroke. Moreover, by 2030, it is expected an increase to 23.3 million deaths, annually, from CVDs [7, 10]. The worldwide death distribution is

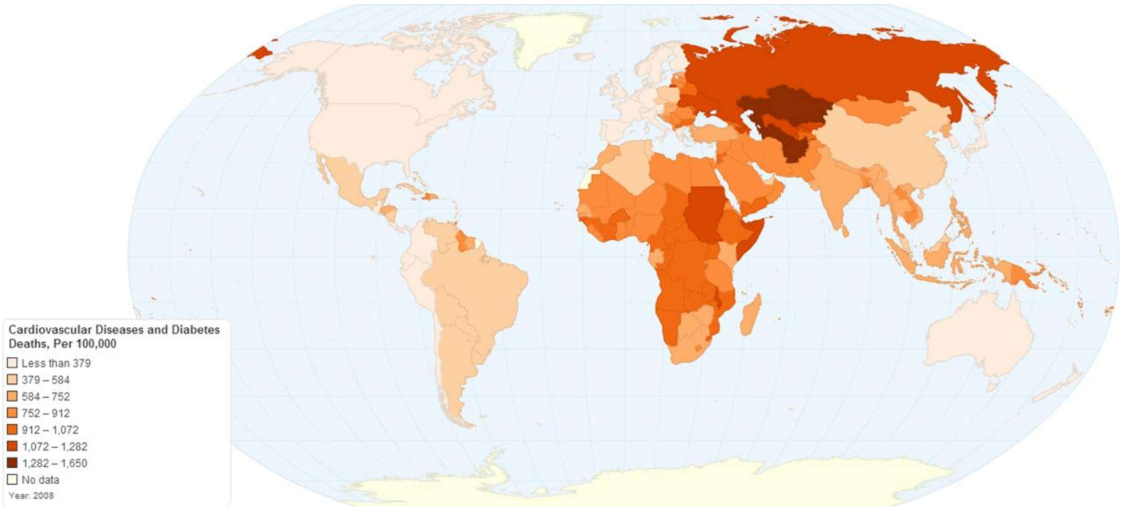

Figure 1.5 - World distribution of estimated age-standardized mortality rate due to cardiovascular diseases and diabetes, by 2008 [13].

disproportional, with over 80% of CVD deaths taking place in low- and middle-income countries [Figure 1.5]. Such remark is probably related to the limited prevention efforts and limited access to effective health care services in these countries, which leads to little screening and impaired early diagnosis and treatment of CVDs. Regarding gender distribution, the global deaths are quite similar between men and women [7, 10]. In disability-adjusted life years (DALYs) lost, seen as healthy years of life lost, cardiovascular diseases are responsible for 10% of DALYs lost in low- and middle-income countries and 18% in high-income countries [8]. After HIV/AIDS, CHD and stroke are the leading diseases in DALYs lost, with 6.8% and 5% of all DALYs lost in men, respectively, and 5.3% and 5.2% in women [8]. Moreover, from 47 million DALYs lost globally in 1990 due to CHD, an increase to 82 million DALYs lost in 2020 is expected. In turn, stroke was responsibility for 38 million DALYs lost globally in 1990, with an expected increase to 62 million DALYs lost by 2020 [8]. Overall, CVD rates are declining in the high income countries, but increasing in low- and middle-income countries, leading to an increase of mortality and morbidity rates, family suffering and staggering economic costs [6].

In Portugal, specifically, by 2009, CVDs were responsible for 31.9% of all deaths (33.4 thousand people), which 44.3% and 55.7% of them were men and women, respectively [12]. According to WHO, the estimated age-standardized mortality associated with CVD and diabetes is 185 and 125 per 100000 for men and women, respectively [Figure 1.5], which is similar to most high income countries [13, 14]. Moreover, 12% and 10% of years lost in men and women, respectively, were related to CVDs (representing 559 and 221 years lost per 100000 males and females, respectively) [12]. In comparison to Europe, Portugal has similar CVD-related death mortality and DALYs lost for CHD, but a higher DALYs lost due to stroke [8, 12]. By 2009, such numbers represented a health care cost associated with CVDs of € 1.2 billion, which represented 6% of Portugal's total health care expenditure [12].

In summary, all these reports and the known global population aging highlight the increasing need for powerful and efficient techniques for diagnosis and treatment follow-up of patients with CVDs. Among others, assessment of global left ventricular function using non-invasive cardiac imaging seems to be an interesting technique for such purpose.

1.3 Non-invasive Cardiovascular imaging

Cardiovascular imaging revolutionized the practice of cardiology and became a valuable tool for visualization of cardiac structures and assessment of cardiac function [6, 15-17]. Nowadays, multiple modalities and approaches are available to assist the physicians, with specific advantages for the study of different aspects, areas and diseases [15]. Among the multitude of modalities, the most frequently used in cardiology are ultrasound (US) imaging, magnetic resonance imaging (MRI), computed tomography (CT) and nuclear imaging (Single Photon Emission Computed Tomography, SPECT, and Positron Emission Tomography, PET) [6, 15, 17-22]. As stated, the study of different aspects request different modalities: the study of the myocardium is normally performed using MRI, SPECT or PET; cardiac function is assessed essentially by US and MRI; valve structure and function is evaluated using US; coronary arteries and associated diseases can be assessed by CT angiography; and vessels by MRI and CT, as well as ultrasound for peripheral vessels [15]. Each modality has its technical principles, equipment, advantages and disadvantages, which will be shortly discussed in the following sections. Further technical and clinical description can be found in subject-specific literature [15-17, 19-22].

1.3.1 Ultrasound imaging

Ultrasound imaging uses the principle of ultrasound reflection at the interface between different structures to produce images of the inner structures of the body, namely the heart [3, 15, 17, 22]. The ultrasound wave is generated by a piezoelectric crystal, is then reflected in the internal interfaces and detected by the same piezoelectric crystal. The measurement of such reflections as a function of time (amplitude versus time delay) gives information about the position of the interface and the acquired data can be reconstructed to obtain a 2D image [19]. Nowadays, certain transducers are even able to obtain 3D images over time, giving real-time dynamic images of the heart. Echocardiography is used for visualization and assessment of myocardium, cardiac chambers, valves and pericardium [6, 19]. Moreover, by using the Doppler effect, Doppler echocardiography allows to measure the blood flow velocity across valves, within cardiac chambers and through great vessels [6, 19, 22].

In summary, US is a non-invasive, relatively inexpensive and portable imaging modality able to acquire cardiac images with excellent temporal resolution and without the need for ionizing radiation [15, 17, 19, 22]. Despite the presence of artifacts, it is one of the most used modalities in cardiology practice, being used for guidance during interventions and ideal for cardiac emergencies [19]. However, the use of echocardiography is limited by operator dependence, image quality and the need for an adequate acoustic window [22, 23].

1.3.2 Magnetic resonance imaging

Magnetic resonance imaging (MRI) is an imaging modality based on the measurement of the magnetic properties of hydrogen nuclei distributed in the body [6, 15, 17, 19]. In the presence of a large constant magnetic field, usually 1.5 or 3 Tesla, the protons in the body are aligned, being then perturbed by the use of radio-frequency pulses. After excitation, they relax back to their initial state, resulting in a signal that can be detected and processed to generate an image [6, 17, 20]. Due to the huge amount of sequences (combinations of radio-frequency and magnetic field gradient pulses), MRI has the ability to generate a plenitude of different images with distinct characteristics and goals [23]. Although cardiac motion can be a challenge, one is able to obtain both static and cine (dynamic) images (by prospective or retrospective gating with an ECG), allowing the study of anatomy and function. Currently, cardiac magnetic resonance (CMR) is the gold-standard modality for accurate quantification of ventricular volumes, mass and ejection fraction, presenting a high accuracy, reliability and reproducibility [6, 24-27]. To this end, both long-axis (LAX) and short-axis (SAX) images can be acquired [Figure 1.6], consisting in the imaging of the structure axis and orthogonal views, respectively. Normally, a stack of SAX cuts is

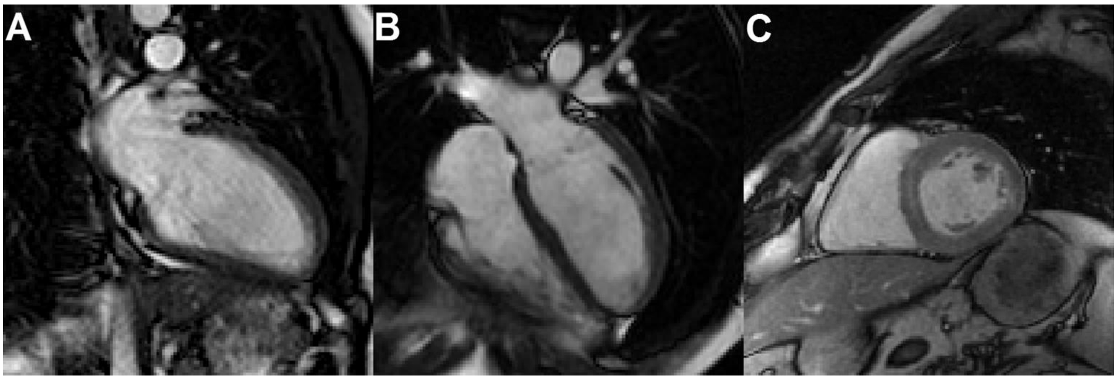

Figure 1.6 - Steady-state free precession (SSFP) cardiac magnetic resonance (CMR) images in: (A) two-chamber long-axis (LAX); (B) four-chamber LAX; and (C) short-axis (SAX) views.

acquired to cover the studied structure, while one or two LAX views (two-chamber or four-chamber views) allow further evaluation [16, 17].

The main advantages of MRI are its non-invasiveness and lack of ionizing radiation, as well as its flexibility to acquire images in any image plane [6, 15, 17-20, 22-24]. Moreover, it provides a better contrast between different soft tissues than other modalities, namely CT. In cardiology practice, the variety of MR sequences and its moderately high spatial resolution permit the assessment of ventricular function, as well as information on morphology, myocardial perfusion, tissue viability and contractility, metabolism or even blood flow [6, 19, 23-25]. Thus, it is used for the diagnosis and follow-up of congenital heart diseases, cardiomyopathies, cardiac masses and other CVDs [6, 25]. However, MRI has the disadvantage of presenting a relatively low temporal resolution, relatively long scan time, high exam cost and contraindications in the presence of implanted cardiac devices. In certain sequences, the use of contrast, e.g. gadolinium, can be a limiting feature in patients with a renal disease [6, 17, 20]. Nevertheless, given its excellent accuracy and reproducibility [27], it remains the gold-standard modality for left ventricular morphology and global function assessment. Thus, the present study will focus on this modality.

1.3.3 Computed Tomography

Computed tomography (CT) is a fast, simple and non-invasive technique that produces images representing the X-ray attenuation properties of the scanned tissues [6, 15, 19, 21]. By transmitting an X-ray beam through the body, a 2D projection of such attenuation image is obtained, which can be acquired for several angles. By reconstruction algorithms, the set of 2D projections can be combined to create an image of the actual attenuation at each point scanned. At the end, a stack of 2D cross-sectional images are acquired with excellent spatial resolution and good soft tissue contrast [6, 19, 21]. After several technological advances, the use of multi-slice CT led to the improvement of the temporal resolution as well [19]. To obtain dynamic 3D images, the acquisition of volumes can be prospectively or retrospectively gated with an ECG, allowing the reconstruction of these images at specific phases of the cardiac cycle [6, 21].

In cardiology practice, CT has become the standard modality for the visualization of the coronary arteries, with assessment of coronary calcification, stenosis grading and atherosclerosis plaques characterization by coronary CT angiography (requiring contrast agents) [6, 21]. Moreover, CT allows to assess anatomy and global function of the heart, pericardium and masses [6]. In contrast, the use of ionizing radiation and the need for iodinated contrast agents are some limiting factors associated with this modality [6, 21, 23].

1.3.4 Nuclear imaging

Nuclear imaging is a modality based on detecting radioactive labeled biochemical compounds (tracers) administrated to the patient usually by intravenous injection. Once inside the body, these specifically designed radioisotopes are able to trace physiological processes. Due to its active form, during radioactive decay they emit radiation in the form of photons that can be detected and used to create images of their distribution [6, 15, 18, 19, 22]. There are two main techniques in diagnostic nuclear medicine: SPECT and PET. In SPECT, gamma-emitting radionuclides are used and one or more gamma cameras detect the released gamma photons. After obtaining several 2D projections at different angles, a tomographic reconstruction can be performed to create a cross-sectional image of the tracer distribution which is linked to the process being studied [19]. In PET, positron-emitting radionuclides are used and a coincidence detector registers the emission events as a function of position and time. Afterwards, a processing unit is able to create a 3D volume of the radionuclide distribution [18, 19]. In contrast to CT and MR, designed mainly for anatomical imaging, SPECT and PET are designed for physiologic, metabolic and molecular imaging, being able to describe specific processes undergoing inside our body [6, 15, 18, 19]. Nowadays, hybrid scanners are combining PET or SPECT with high spatial resolution CT, or even MR, to associate the anatomical information given by the latter with the functional evaluation obtained with nuclear imaging, which is increasing their usefulness in clinical practice [19, 22].

In cardiology, these modalities are considered robust, accurate and reliable for clinical imaging of several diseases, namely for the assessment of myocardial perfusion, metabolism and viability, as well as the study of CHD and ventricular function. Its main disadvantages are the need for radiation and the limited spatial resolution obtained [15, 19, 22].

1.4 Quantification of cardiac function

The accurate assessment of cardiac performance is clinically important to determine the disease severity and to evaluate the efficiency of the treatment. Non-invasive imaging is part of the daily clinical examination and has a primary role in the clinical assessment and patient management. Such clinical evaluation comprises both global and regional function of the heart [16, 17, 28, 29]. Although all four chambers have their clinical value in cardiac performance assessment, the left ventricle has a vital role in cardiac function, thus explaining the interest in characterizing its global and regional function [29]. Therefore, the assessment of global left ventricular function (in CMR datasets) will be the main purpose of the present work.

Assessment of global left ventricular function comprises the measurement of the adequacy of the LV to pump the blood into the aorta. Concerning CVDs diagnosis and follow-up, physicians are especially interested in computing left ventricular volumes and mass at two moments of the cardiac cycle, corresponding to the time of maximal filling/relaxation (end-diastole, ED) and maximum emptying/contraction (end-systole, ES) [16, 28, 29]. Although ideally the changes in volumes and mass, as well as the rate of changes, could be essential for completely describe the global function, clinical routine only focuses on these two time points [16]. Thus, two cardiac indices are measured for global morphological assessment, namely end-diastolic volume (EDV) and end-systolic volume (ESV). From these two volumetric parameters, other global cardiac functional parameters can be deduced, such as stroke volume (SV), cardiac output (CO) and ejection fraction (EF) [16, 28, 29]. SV is defined as the volume ejected between the end-diastole and end-systole moments and is given by equation (1.1). In turn, cardiac output measures the quantity of oxygenated blood supplied to the body. It depends on the patient's heart rate, is expressed in liters per minute and is given by equation (1.2). Lastly, EF is the volumetric fraction of blood pumped out in each cardiac cycle, being computed from SV and EDV according to equation (1.3). EF is normally considered one of the most meaningful measures of the LV function [28, 29], with clinical value in HF, valvular heart disease, among others [6, 30-33]. Note that the accuracy by which both EDV and ESV are determined limit the reliability of the deduced cardiac parameters, which in turn can have an influence in patient management and disease diagnosis [16]. Another important global ventricular parameter is left ventricular mass (LVM) [16, 28, 29], which was proven to have a role in predicting morbidity and mortality in CHD [16, 34]. The computation of LVM can be obtained by multiplying the myocardial volume (volume between endocardium and epicardium, V_{myo}) with the specific density of this tissue, according to equation (1.4). These clinically relevant functional parameters can then be used by a physician to assess the global cardiac function of the subject by comparing them to established ranges of normal CMR values for healthy subjects [6, 35].

$$SV(cm^3) = EDV - ESV \tag{1.1}$$

$$CO(l/min) = SV \times HR \tag{1.2}$$

$$EF(\%) = \frac{SV}{EDV} \times 100\% = \frac{EDV - ESV}{EDV} \times 100\% \qquad (1.3)$$

$$LVM(g) = V_{myo} \times 1.05\, g/cm^3 \qquad (1.4)$$

In order to compute these cardiac parameters, two different approaches can be used, namely geometric assumptions and true volumetric quantification [16, 36]. Geometric assumptions use standardized measurements of the cavity to compute its volume by assuming a specific geometric model. To this end, both SAX images (hemisphere cylinder model, modified Simpson's technique or Teichholz model) and LAX images (biplane ellipsoid and single-plane ellipsoid model) or a combination of both (e.g., combined triplane model) can be used, with specific assumptions and, therefore, limitations [16, 36]. The main advantage of geometric assumptions is the rapid quantification, as only a limited number of measurements should be performed. However, the geometric model and its assumptions are only reliable if they coarsely correspond to the real patient-specific LV shape, which may not be the case in locally diseased ventricles [16]. Moreover, the intra- and inter-observer variability associated with all these models is considerably high for clinical, or even academic, use [36]. On the other hand, using the aforementioned non-invasive imaging modalities, namely 3D-echocardiography, CT and MRI, a true volumetric quantification is feasible by relying on the Simpson's rule, i.e. the sum of multiple smaller volumes of similar configuration. According to this method, the quantification of separate volumes (one for each image in a stack covering the LV) and their summation result in the total ventricle volume [16, 28, 29, 36]. Such volumetric quantification generally leads to more reliable volumes and mass estimation, but it is more time-consuming, both in terms of image acquisition and post-processing [16]. In practice, true volumetric quantification is generally used for its accuracy and reproducibility, therefore being addressed in the present work.

Thus, in order to quantify the above cardiac indices, the delineation of both endocardial and epicardial contours of the left ventricle from a stack of cardiac images, namely cine MR images, is required. From the endocardial delineation, one is able to compute the corresponding LV cavity's area. Then, this area is multiplied by the interslice distance (slice thickness plus slice gap, if present), resulting in the volume calculation for the studied slice. By repeating this process for all slices covering the LV, from the atrioventricular ring to the apex, and summing them, the total ventricular volume is obtained [16]. Therefore, EDV, ESV, SV, CO and EF can be computed and used for clinical evaluation. For LVM computation, both delineated contours should be used. In this sense, the myocardial volume (V_{myo}) correspond to the subtraction of the cavity's volume (area inside endocardium) from the epicardial volume (area inside epicardium). Again, by

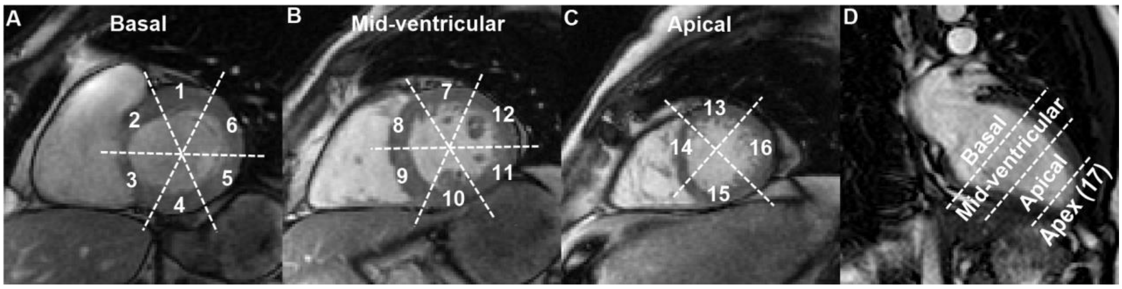

Figure 1.7 - 17-segment frame of references used for LV division.
The 17-segment division separates the SAX slices into **(A)** 6 basal, **(B)** 6 mid-ventricular and **(C)** 4 apical segments, with **(D)** segment 17 being the apex in LAX image. Nomenclature of the segments: 1, 7 and 13: anterior; 2 and 8: anteroseptal; 3 and 9: inferoseptal; 4, 10 and 15: inferior; 5 and 11: inferolateral; 6 and 12: anterolateral.

computing the area for each slice and multiplying by the interslice distance, LVM is then obtained by summing all volumes and multiplying by the myocardium density (equation (1.4)) [16].

In addition to clinical cardiac indices computation, the delineated contours are also important for analysis of wall abnormalities and comparison with other images of the same subject (other CMR sequences or even other modalities, such as CT). In this sense, a 17-segment frame of reference is usually used [16], dividing the left ventricle into three SAX planes along the LV long-axis: basal, mid-ventricular (or mid-cavity) and apical slices [Figure 1.7]. Each SAX plane is further radially divided into segments: 6 segments for basal and mid-ventricular levels and 4 segments for the apical level [Figure 1.7A-C]. The 17th segment corresponds to the apex, being only visualized in LAX images. Such division will be used throughout this work to locate and analyze the delineation (in)accuracy.

Besides global ventricular function, also regional function can be assessed, namely myocardial wall thickness, systolic wall thickening and circumferential and longitudinal wall motion or shortening [16, 28]. Myocardial thickness can be calculated taking into account both endocardial and epicardial contours. Concerning wall thickening, its absolute or percentual value can be computed by considering both ED and ES regional wall thickness. Moreover, the internal deformation of the myocardial wall can also be studied and quantified by strain analysis [28]. Note that the LV division scheme presented above is fundamental in such regional assessment of LV performance [Figure 1.7]. Although important for several cardiac diseases, these regional cardiac indices will not be addressed in the present work. Notwithstanding, it is crucial to keep in mind the importance of longitudinal wall motion in the computation of volumes, in order to correct for through-plane motion [16].

1.5 Motivation

In clinical practice, manual segmentation is usually performed for LV contouring, being a tedious, time consuming and unpractical task [29], normally requiring between 6 to 20 minutes to segment all slices covering the LV only in the ED and ES cardiac phases [29, 36, 37]. Moreover, manual delineation is prone to intra- and inter-observer variability, mainly associated with the choice of ED and ES phases, the choice of the most basal LV slice and the chosen endocardial edge selection approach (Section 2.1) [35, 36]. In fact, the analysis methodology used is a major source of variability in a "real-world" scenario, leading to significant differences in the quantification of LV indices. In practice, such differences would request specific reference ranges depending on the contouring methodology used [36]. Although manual segmentation is still extensively used in clinical practice for left ventricle delineation in CMR datasets, its disadvantages allow us to understand the importance of developing a robust, efficient, accurate and fast segmentation method. Such solution would permit to compute relevant cardiac parameters without the user-induced variability and in a more time efficient manner.

To date, several methods have been presented for (semi-)automated LV CMR segmentation (Section 2.2) [29]. Moreover, several commercial software packages are nowadays available for manual, semi-automated or automated analysis of CMR datasets (Section 2.3). Notwithstanding, due to the difficulties in designing a solution able to deal with the segmentation challenges presented in CMR images (Section 2.2) [29, 38], fast, automatic and optimal boundaries assessment from base to apex is still lacking, usually requiring the physician to manually correct the contours [36, 37, 39, 40]. Thus, LV CMR segmentation remains an open problem with significant clinical value, easily noticed by the constant attention in the research field [29, 38, 41-46].

Both available (semi-)automated methods in research and their commercial counterparts are still requiring user interaction (in different levels) or lack accuracy and robustness for having success in daily clinical practice [39, 40]. Moreover, only a few allow tracking of the contours throughout the cardiac cycle by segmenting every cardiac phase. Such delineation of the full 3D+time CMR dataset can introduce further knowledge about the variation of left ventricular volumes and other quantitative parameters, which may be used to complement the heart contractile function characterization [3]. At last, the time required to obtain these segmentations is a limiting factor, being a critical aspect for success when introducing a methodology in daily clinical practice.

1.6 Aims and contributions

The focus of the present work was to develop a fast fully automatic 3D+time LV myocardial segmentation framework for CMR datasets with accurate shape delineation and low computational burden, to be of interest in daily clinical practice, allowing both left ventricular morphology and global function assessment. Hereto, the recent B-spline Explicit Active Surfaces (BEAS) framework developed by Barbosa *et al.* [47] (Section 2.4) was used as starting point to design the LV CMR-specific segmentation platform.

The main goals/contributions of the present work are as follow:

1. Study of the state-of-the-art of LV segmentation for CMR datasets, along with the challenges and difficulties present in these images;
2. Development of a CMR myocardial segmentation framework and subsequent validation of each step of the methodology, including:
    a) Development of a novel automatic initialization procedure, based on thresholding and elliptical template matching, for LV detection and initialization in mid-ventricular SAX cuts.
    b) BEAS algorithm implementation for coupled 2D CMR segmentation;
    c) Development of a hybrid CMR-targeted segmentation energy designed to tackle the specific challenges of this modality;
    d) Development of an automatic stack initialization algorithm, using a threshold-based BEAS formulation, and a method for correction of misalignment between slices;
    e) 3D extension of the BEAS framework, including reformulation of the segmentation problem for a cylindrical space, suited to deal with the CMR data anisotropy;
    f) Implementation and study of two tracking methodologies, namely a profile matching based BEAS and an anatomical affine optical flow method, for endo and epicardial boundary detection throughout the cardiac cycle.
3. Clinical validation of the developed framework in an extensive database with “real-world” variability in both contrast and anatomical and functional characteristics.

1.7 Thesis Overview

The current chapter introduced the clinical context of the present work, giving an overview on the cardiovascular system and related diseases, along with a description of non-invasive imaging modalities used in cardiology. Moreover, an explanation of the quantification methods for left ventricular global function assessment was given. Finally, the motivation, the goal and the main contributions were presented. The next chapters will be devoted to the development of the introduced topics.

The second chapter aims to present the state-of-the-art on LV CMR segmentation, including research and commercial solutions. Manual contouring techniques, challenges and pitfalls are also discussed to better understand how a (semi-)automated method can help in clinical practice. At last, the B-spline Explicit Active Surface framework, which will be used as starting point to design the LV CMR-specific segmentation platform, is described.

The third chapter presents the methodologies developed in the present thesis to achieve the main goal of this work, comprehending an automatic 2D mid-ventricular initialization and segmentation method, an automatic stack initialization and a 3D segmentation algorithm for the ED phase, and two tracking procedures to delineate both endo and epicardial contours throughout the cardiac cycle.

The fourth chapter focuses on the achieved results, on a publicly available database, for each developed module of the proposed framework. In addition, a comparison against state-of-the-art methods is given to understand the relevance of the present work in the scientific context.

The fifth chapter discusses the main results and gives some insights on the accuracy and robustness of the proposed framework for LV CMR segmentation.

The sixth chapter reveals the clinical validation of the proposed automatic segmentation framework in an extensive multi-center database with "real-world" variability, ultimately assessing the interest from the daily clinical practice point-of-view.

Finally, the seventh chapter presents the main conclusions of the present thesis and gives some perspectives about possible future developments/improvements.

2. Cardiac Segmentation

2. Cardiac Segmentation

2.1 Computed-assisted manual contouring in CMR datasets

In daily clinical practice, manual contouring is the method of choice for true volumetric quantification of left ventricular global function in CMR datasets. To this end, the physician or radiologist has to delineate both endocardial and epicardial contours in all slices covering the LV, from the atrioventricular ring to the apex, in at least two cardiac phases: ED and ES [Figure 2.1]. Usually, 6 to 20 min are required for this delineation [29, 36, 37], which affects the time taken to execute a full cardiac exam. In fact, adding the relatively long scan time associated with MRI [17, 20], a basic cardiac exam spends between 45 to 60 min for acquisition and analysis, which has implications for patient management and health costs. Nevertheless, when appropriately ordered, CMR can be cost effective by triggering major improvements in diagnostic accuracy, risk assessment and therapeutic decision making, therefore decreasing the overall exam use, shortening diagnosis time, improving patient outcome, decreasing hospitalizations and length of stay and reducing invasive procedures use [48, 49].

In order to be meaningful, the cardiac parameters quantified after contouring should be compared to normal reference ranges for healthy subjects. To this end, several studies have been performed to assess these ranges for different MRI acquisition sequences, such as SSFP [35, 50-52], Fast Low Angle Shot [53] or Turbo Gradient Echo [50]. Moreover, some of these studies evaluate the influence of gender, body surface area or age in these values [35, 50, 52], allowing a personalized management according to the patient' characteristics [52].

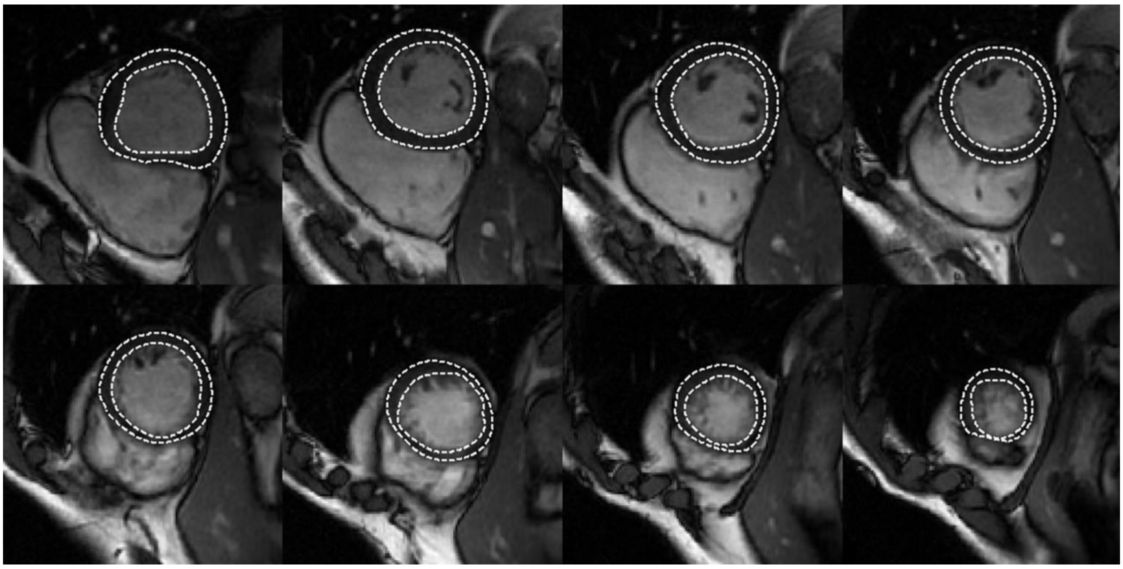

Figure 2.1 - An example manual contouring of endocardial and epicardial contours in all slices covering the LV, from the atrioventricular ring to the apex, in the end-diastolic phase.

Notwithstanding the high reproducibility of CMR [26, 27, 54, 55], the variability in cardiac parameters associated with contouring is still substantial to be underestimated. Several studies have tried to quantify it and determine its major sources [35, 36, 56-61], in order to better understand it and ultimately mitigate its effects. One of the potential sources for variability is associated with the imaging parameters used in acquisition. Hogan *et al.* studied its effects in SSFP images and concluded that similar measurements in LV volumes, mass and EF are obtained for slight variations in slice thickness and interslice gap, flip angle, repetition time, echo time, matrix size and field of view, giving comparable and interchangeable values [60]. Therefore, the main variations are not associated with acquisition, but primarily with the subsequent analysis. In fact, manual contouring is responsible for the majority of variability in cardiac parameters quantification, with both intra- and inter-observer variability present [36, 56]. Among the plenitude of possible causes of variability, the choice of ED and ES phases, the choice of basal slice and the edge selection approach are the main sources [35, 36, 58, 59].

The edge selection approach was identified as the fundamental problem in manual contouring, with different delineation methodologies being employed by different physicians [35, 36, 59]. Such problem is less significant in epicardial border tracing, as little confounding edges are found and only mass is affected, but it is huge in endocardial contouring [36]. The difficulty with endocardial contour is associated with trabeculae and papillary muscles (TPMs), yielding variability and affecting the measurement reproducibility [59, 61]. Depending on the physician, clinical center or software used, four main possibilities for endocardial delineation are employed: 1) contouring of the "compacted" endocardial border [Figure 2.2A]; 2) detailed tracing of TPMs, only delineating LV blood pool [Figure 2.2B]; 3) delineation of the "compacted" endocardial border and major papillary muscles [Figure 2.2C]; and 4) contouring of the "compacted" endocardial border, followed by intensity-based thresholding technique to distinguish blood pool

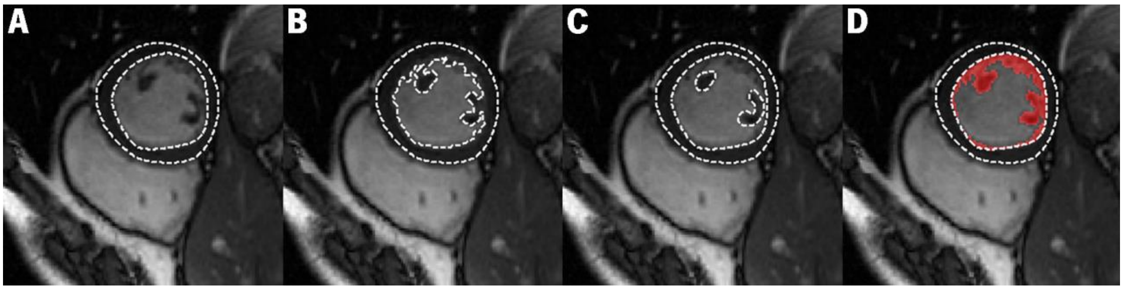

Figure 2.2 - Different methodologies for endocardial contouring.
(A) Delineation of "compacted" endocardial border; **(B)** Detailed tracing of TPMs; **(C)** Contouring of "compacted" endocardial boundary and major papillary muscles; **(D)** Delineation of "compacted" endocardial border, plus computer-based signal intensity distinction between LV cavity and TPMs.

from TPMs [Figure 2.2D]. Regarding the quantification of LV parameters, case 1 includes TPMs in volumetric measurements of the cavity, while case 2 includes them in the LV mass (excluding them from cavity volumes). In cases 3 and 4, the two options can be obtained, including TPMs in mass calculation or including them in the ventricular cavity for cavity volumes computation, with different approaches regarding the trabeculae.

Besides edge contouring, LV base identification contributes substantially to the variability [35, 36]. In this context, two main possibilities can be employed depending on the images used: short-axis or long-axis derived LV base positioning. Note that often only SAX images are acquired for analysis, therefore impeding the use of LAX-derived identification. In SAX-derived identification, an arbitrary criterion has to be used, such as the inclusion of the slice having 50% or 75% of the cavity surrounded by myocardium. Alternatively, when both ventricular and atrial myocardium are present, some physicians prefer to delineate the LV cavity followed by a straight or curved line through the blood pool. In LAX-derived positioning, the mitral valve is identified in the LAX image and subsequently related with the stack of SAX cuts, possibly falling between two slices and including only the respective percentage of thickness. According to [36], if LAX images are available, LAX LV base identification is suggested as it has proven to be more robust. Moreover, the LV base should be tracked throughout the cardiac cycle, allowing to detect and correct for longitudinal contraction [16, 58].

Finally, the choice of end-diastole and end-systole moments was reported as the third major source of variability, although considerably less influent than the previous two [35, 36]. In practice, both moments are identified visually by selecting the largest and smallest cavities associated with maximum relaxation (ED) and contraction (ES), respectively. In this sense, ED is normally easy to identify, while ES can be less evident. Nevertheless, normally only one single frame of difference is seen [35]. Alternatively, automatic ES determination is sometimes employed using specific software, being more accurate and involving less manual input [36].

In summary, the variability in contouring methodology used in the “real-world” scenario leads to significant differences in the quantified LV indices [36]. In practice, such differences would request specific reference ranges depending on the contouring methodology used, which is cumbersome and impractical. Thus, (semi-)automated segmentation methods are fundamental to mitigate the effects introduced by manual contouring/input and, ultimately, obtain more confident, accurate and robust quantifications.

2.2 (Semi-)Automated CMR segmentation

Due to the importance of developing an accurate and robust framework, to date, several methods have already been presented for (semi-)automated LV CMR segmentation, most of them gathered in the recent review of Petitjean and Dacher [29]. Despite such effort, fast, automatic and optimal boundaries assessment from basal to apical slices is still lacking, usually requiring the physician to manually correct the contours. Thus, LV segmentation is still an open problem, whose efforts seen in the research field reinforce the difficulties in designing a framework that can deal with the segmentation challenges presented in CMR images [29, 38, 62-64], such as:

- the poor contrast between myocardium and surrounding structures (e.g., lungs and liver) [Figure 2.3B];
- the heterogeneities in the LV cavity brightness due to blood flow [Figure 2.3D];
- the presence of TPMs with similar intensities to the myocardium [Figure 2.3G];
- the partial volume effects (PVE) in apical slices due to limited MRI resolution;
- the inherent noise associated with cine CMR and caused by motion artifacts, heart dynamics and intensity inhomogeneity;
- and the considerable shape and intensity variability of the left ventricle across patients [Figure 2.3], notably in pathological cases.

According to [29], the plenitude of methodologies found in the literature for LV CMR segmentation can be divided in two main categories: weak or no prior methods and strong prior methods. The first category uses weak assumptions, like spatial relations (e.g., the RV is to the left of the LV), anatomical assumptions (e.g., circular geometry of the LV) or intensity-based

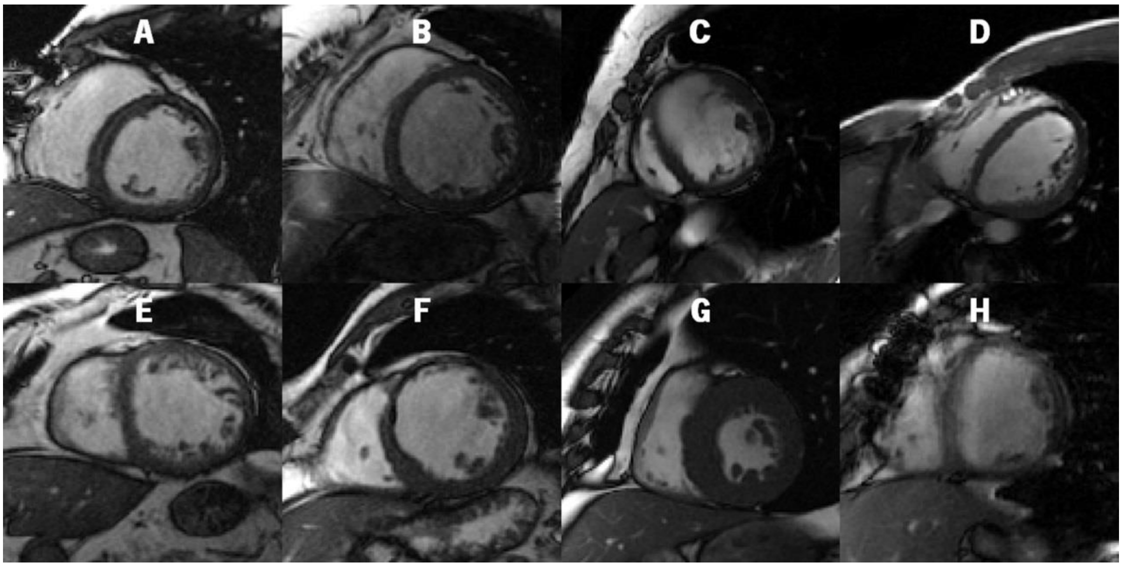

Figure 2.3 - Left ventricle shape and thickness variability at mid-ventricular slice across patients.

relationships (e.g, myocardium is darker than the LV cavity in SSFP CMR images) to guide and constrain the LV segmentation, increasing its robustness and accuracy. Thus, weak or no prior category includes image-based techniques (thresholding [65-67], dynamic programming [43, 44, 68], etc.), pixel classification methods (gaussian mixture model fitting [69-71], clustering [72, 73], etc.) and deformable models (active contours, level-sets and variants) [38, 45, 62-64, 74-83]. The second category, strong prior methods, include shape prior based deformable models [64, 84], active shape and appearance models (ASM/AAM) [85-89] and atlas based methods [90-92], which focus on higher-level shape and intensity information and normally require a training dataset with manual segmentations. By imposing constraints based on learned features from manual delineations, these methods are normally able to overcome some of the aforementioned imaging challenges (presence of TPMs, intensity heterogeneities and low contrast) without user interaction [29]. However, building a training set with manual contours is time-consuming and extremely difficult. Moreover, although efficient in most cases, the use of training datasets intrinsically links the method's ability to handle clinical variability to the amount of different morphological and physiological cardiac information included in the training phase. Due to the vast amount of methods present in the literature, we chose to give a general overview of each mentioned technique by shortly describing their principles (in Sections 2.2.1 to 2.2.6).

Besides prior information, the level of user interaction associated with a given methodology is also crucial. In this sense, 3 levels can be distinguished: fully automated; limited user interaction (e.g., pointing the LV center or dragging a circle); and advanced user interaction (e.g., requiring a manual segmentation in the first image of a sequence). Taking into account the prior information division, weak or no prior methods tend to require minimal or advanced user interaction, while strong prior methods tend to be fully automatic [29]. Such observation clearly shows a tradeoff between used prior information and required user interaction. In this sense, Section 2.2.7 will focus on the state-of-the-art in automatic localization of the heart and LV.

2.2.1 Image-based methods

Image-based techniques rely mainly on intensity information and geometric assumptions to delineate both contours, usually using thresholding [65-67] and/or dynamic programming (DP) [43, 44, 68]. While thresholding rely uniquely on the image intensity, DP searches for the optimal path in a cost matrix that assigns a low cost to object boundaries. The design of the cost matrix is the main problem in DP and can be computed based on simple thresholding [68], fuzzy logic, radial lines or image gradient values [43, 44, 93], giving DP more flexibility.

Independently on the approach used, most image-based methods conceptually divide the problem in 3 steps: endocardial contouring, epicardial contouring and contours smoothing. Typically, the two contours are differently and separately segmented, relying on the endocardial contour in the second step to delineate the epicardium [43, 44, 66, 67]. Moreover, because TPMs present a similar intensity to the myocardium, these methods usually lead to the wrong inclusion of TPMs in the myocardium, either when using thresholding or gradient-based DP. Therefore, computation of the endocardial contour's convex hull [68], mathematical morphological (MM) operators [93] or smoothing by Fast Fourier Transform or Bezier curve fitting [43, 44, 66, 67] are used to smooth the endocardial contour and completely or partially overcome TPMs, obtaining roughly circular LV shapes.

2.2.2 Pixel classification methods

Pixel classification is the process of assigning a label for each pixel (or voxel) to be segmented, thus including them in a particular class (e.g., blood pool vs. myocardium) [19]. The classification process is possible by analyzing a set of representative features (e.g., image intensity, local entropy, etc.), followed by a labeling to the most likely class. In the end, all pixels assigned for the same class share the same features' characteristics. Pixel classification includes unsupervised and supervised techniques. While unsupervised techniques only use weak assumptions and no user interaction is needed for the classification process, supervised ones require a learning phase, for which labeled example pixels need to be available (by manual or automatic learning) [19, 29].

In LV CMR segmentation, gray level values are often used as features and mostly unsupervised techniques are employed, namely Gaussian Mixture Model (GMM) fitting [43, 69-71] and clustering [72, 73]. The principle of GMM is to describe the image histogram by a mixture of gaussian distributions using the Expectation-Maximization (EM) algorithm [94]. To this end, the number of classes has to be set *a priori*, usually considering two to five distributions (e.g., blood pool, myocardium and background [71]). The classification is an iterative process, where in each stage the distributions' parameters are estimated while trying to maximize the likelihood of each pixel belonging to a given class [94]. After pixel classification, each connected component can be post-processed using MM to reduce noise [72] and/or smoothing operations [43], yielding the final contours. On the other hand, clustering is the process of data aggregation in clusters in a feature space [29]. Clustering is commonly performed through K-means algorithm [73] or, more generally, fuzzy C-means (allowing partial membership in classes). After this step, each cluster is studied to determine the object of interest (e.g., considering the LV's circular aspect or gray level intensity) and then post-processed to obtain smooth contours [73].

2.2.3 Deformable models

Active contours, or snakes, were one of the first methodologies of deformable models to be presented [95]. They are a flexible framework where the shape to recover is captured by propagating an evolving interface while minimizing an energy functional that reflects the object's properties [47]. Their flexibility is mainly related to the easy incorporation of prior knowledge about the object's shape and expected intensity distribution, as well as of temporal constraints [29]. In this sense, the energy functional comprises internal forces (or regularization terms, constraining the curve evolution) and image forces (or data-driven terms, derived from image features) [29, 47]. In the classical parametric formulation, the energy functional minimization is solved using partial differential equations [95]. Later, Osher and Sethian [96] proposed the level-set framework, where the desired contour corresponds to the zero level of a higher-dimensional signed distance function. This framework brought topological flexibility and increased their applicability by allowing multiple objects segmentation [97].

In LV CMR segmentation, these methods have been used extensively during the last decades, allowing 2D, 3D and even 3D+time approaches to be developed [29]. About their technological evolution, the focus is mainly in the design of data-driven terms, where information about the ventricle's shape and intensity can be introduced in several different ways. Data-driven terms are usually classified as edge-based or region-based. Edge-based energy terms use image gradients to identify object boundaries and attract the contours toward edges [45, 63, 74-78], while region-based ones use regional properties inside and outside the object to evolve the contour [47, 63, 74-77, 98]. Among edge-based energies, Gradient Vector Flow (GVF) algorithm [99] is one of the most widely employed [45, 74, 78, 79], where the image gradient is diffused to create an edge map used to attract contours towards boundaries (even into concavities). The regularization terms are frequently based on curvature or smoothing constraints, although some frameworks implicitly incorporate such regularization in the curve's parameterization [47]. To improve accuracy, some authors combine both edge-based and region-based terms, while also adding smoothness constraints, contour interaction and/or shape priors [63, 64, 74-77]. For contour interaction, coupled formulations have been proposed to obtain a globally optimal segmentation for both endo and epicardial contours. The central idea is to halt the propagation when the distance between contours goes locally beyond the acceptable limits [74] or globally beyond an average thickness [63]. Moreover, temporal constraints can be added to obtain consistent contours through temporal sequences of images [62, 64, 80], either by sequential approach (segmentation in time *t* used at time *t+1*), by encoding prior knowledge about cardiac temporal evolution or using segmentation/registration coupled approaches.

The main limitation of active contours, level-sets and variants are their sensitivity to initialization, requiring some user interaction either in a minimal way [63, 74, 76] or in an advanced way (e.g. required a manual contour in the first frame) [64, 80]. Nevertheless, several authors proposed automatic initialization procedures, focusing on obtaining a robust initialization for subsequent segmentation (see Section 2.2.7).

Besides active contours and level-sets, some methodologies use biomechanical models to constrain the segmentation [81-83], including information on fiber orientation (to mimic myocardial contractility), material's elastic properties, among other features. Such models are usually solved using finite element methods and require solid knowledge of cardiac motion and tissue deformation (strain) [29]. The main idea of these models is to study myocardial contraction during the cardiac cycle by tracking it over the acquired image sequences.

2.2.4 Shape-prior based deformable models

Shape-prior based deformable models use the same energy minimization principles discussed in the previous section, but add anatomical constraints into the contours' evolution. To this end, anatomical reference models can be used, generated from a manually segmented first frame or a set of binary training images, and embedded as multiplicative or additive terms in the energy functional to be minimized [29]. When using a manually segmented first frame, the model usually incorporates both geometry and intensity in the evolution, trying to retain the known shape and intensity distribution over time [64]. The geometry consistency can be introduced as a mean distance to the reference shape model [84] or an overlapping measurement between the current segmentation and the reference manual contour [64]. One should note that when using training data, spatial (and temporal if required) alignment of the manually segmented images is fundamental to compensate for ventricle's position and size differences among datasets [29].

2.2.5 Active Shape and Appearance Models

Active Shape Models (ASMs) are strong-prior methods where a statistical model comprising the typical shape and typical shape variability of an object of interest is iteratively deformed to fit the searched object in a new image [100]. To generate the statistical model, a set of training images (labeled examples of the object of interest) are combined by means of statistical methods, namely by Principal Component Analysis, to describe the average points' position and its main modes of variation. This model is called a "point distribution model" and is then used to segment the object in a new image. The segmentation process comprises two steps: first, the points' position are estimated to best fit the image data (using data-driven terms); and second, the model parameters are updated to best match the new positions, while still constraining the object's shape to remain close to the typical shape and its usual variability. Later, Active Appearance Models (AAMs) were described [101], learning both shape and texture variability in the training phase, which constrains the geometry and intensity distributions of the searched object. Note that all images in the training set should be aligned in order to create the statistical model, but also normalized for their intensities in the case of AAMs. In summary, ASM/AAM can be seen as "smart snakes", where the shape and/or intensity variation in a population are defined explicitly to constrain the segmentation of the object [100, 101].

In LV CMR segmentation, both methods were already reported separately [85, 86], but usually they are combined to complement their unique advantages and mitigate their pitfalls [87, 88]. In this sense, a hybrid model uses an AAM for global appearance estimation, followed by a hybrid ASM/AAM stage for position refinement, as ASMs have greater ability to find local structures [29]. Moreover, an extension of these methods towards temporal segmentation was already reported for 2D+time LV delineation and denominated Active Appearance Motion Model [89]. In this methodology, is important to keep in mind the required huge training set to encompass all the typical shape, appearance and contraction patterns of the LV across subjects. Obviously, the computational burden associated with all these methods, especially in 3D and 2D+time cases, is substantially higher than the aforementioned categories, hampering their use in clinical practice. Moreover, the computation of a statistical model with only a typical shape and shape variability disregard pathological variability, frequently outnumbered in the training set [29, 41]. To overcome this limitation, recently, Eslami *et al.* proposed a framework based on guided random walks with high-level prior knowledge but without the need for statistical shape models [41]. Instead, they guide the segmentation using the closest subject in the database, which brings advantages in pathological cases. Nevertheless, their ability is still linked to the amount of morphology and physiological clinical variability present in the labeled examples.

2.2.6 Atlas-guided segmentation

Like other strong-prior methods, the key idea behind atlas-guided segmentation is to use an atlas (labeled example of the anatomy to be segmented) to incorporate both intensity and spatial information during the segmentation process [90, 91]. The atlas is created from a single subject example (single-subject or topological atlases) or from a population of labeled examples (statistical or probabilistic atlases). In the second type, each dataset in the population should be manually segmented and later registered to each other to fuse them into one single statistical atlas [29]. Then, the principle is to register the labeled atlas onto the new image to be segmented. In this process, non-rigid registration (NRR) is frequently used to allow elastic deformations, while trying to maximize the similarity (sum of squared differences, mutual information, etc.) between the atlas and the target image. After the registration process, the transformation between the atlas and the new image is used to obtain the final subject-specific labeling [29, 90, 91]. As NRR has a lot of degrees of freedom, regularization terms (smoothing terms, statistical models, etc.) have to be implemented to constrain the deformation process, being one of the main focuses of research in these methods [29].

In CMR segmentation, atlas-based segmentation enables whole heart segmentation, by including in the atlas the expected anatomy of ventricles, atria and main vessels [91, 92]. These atlases use labeled examples in the ED frame and are applied in this cardiac phase in the new dataset. Then, to propagate the segmentation throughout the cardiac cycle, the same principle of NRR is employed [90]. Although it is a flexible framework, since the atlas is only used as a starting point in the registration process, the anatomic prior used has little influence in the final segmentation, which limits its ability to accurately constrain the segmentation [47, 91].

2.2.7 Automatic localization of the heart and left ventricle

In the above sections, several frameworks used in LV CMR segmentation were described. However, their majority is still only semi-automated methods, needing minimal or advanced user interaction. Thus, several authors focused on developing automatic initialization procedures to obtain fully automatic frameworks [69, 70, 102-110]. The multitude of methods proposed in the literature can be mainly divided in two categories, namely time-based approaches and object detection techniques, many times fused in hybrid strategies to increase their robustness [29]. Moreover, these methods are frequently divided in two steps: the localization of the heart and the detection of the left ventricle's center, approximate shape and/or size [104, 106, 107].

Time-based techniques rely on the assumption that the heart is the only moving object in the image (or the one with higher mobility) [29]. In this sense, the temporal sequence of images is used to create a motion map, which is afterwards analyzed to detect the brightest object corresponding to a moving object, the heart. This motion map is usually created using a difference [70, 102-104] or variance [69, 105-108] image by analyzing through the time dimension. In the end, a rough location of the heart is obtained, defining a region of interest (ROI) including the LV. After the heart location, thresholding [69, 102, 104, 107] and/or object detection techniques [70, 106] are used to further restrain the defined ROI to only include the LV and, ultimately, obtain its center and/or approximated size. Note that these approaches, being mainly image-based, depend on the image intensities, as well as on the acquired MRI sequence.

In object detection techniques, the principle is to locate the LV taking into account its expected shape, namely the circular aspect of the LV cavity or the annular ring shape of the myocardium [29]. To this end, most methods use a circular Hough transform, which searches for circular objects within a given image/ROI [70, 106, 109]. The principle is to search for multiple circles with different radius and account for their adjustability to the input image, in order to find the circle that best fits the feature space given (e.g., binary image with edge points). Interestingly, for US, a Hough transform for annular shapes was proposed, searching for two concentric circles and increasing the detection robustness [111]. In a similar way, a template matching approach was proposed in [110] to detect the myocardium, using a radially-symmetric kernel modeling a dark ring to mimic the myocardium appearance in SSFP CMR sequences. All the aforementioned object detection techniques rely on the assumption of one (or two) circular shape(s), reducing their detection robustness in subjects with elliptical LV shapes.

2.3 Commercial Software Packages

From the methodologies developed in research, several commercial software packages were created and made available for manual and (semi-)automated analysis of CMR datasets.

Currently, all the major vendors of MRI machines have their own post-processing software package for LV and RV function assessment, myocardial perfusion evaluation and flow analysis [16]. In fact, *Cardiac Explorer* (Philips, Netherlands), *ReportCard 4.0* (GE Healthcare, United Kingdom) and *syngo Argus 4DVF* (Siemens, Germany) are currently being introduced in clinical practice, allowing (semi-)automated LV segmentation in CMR datasets [35, 56, 60, 61]. Moreover, they provide comprehensive clinical reports, encompassing global function parameters and regional myocardial function plots and analyses. According to their manufacturers, they are easy to use and take between a few seconds to a minute to perform the analyses and generate a report. The *syngo Argus 4D VF* uses a heart model-based algorithm to perform the segmentation, requiring the identification of some landmarks, namely the center of the LV apex and base in SAX slices and the mitral valve location in ED and ES phases in the corresponding LAX views. Nevertheless, an integrated tool is also available, denominated *Inline VF* (Siemens, Germany), allowing real-time functional analyses during image acquisition. To this end, both basal and apical slices should be located during the exam acquisition preparation and then these are automatically tracked by a motion compensation algorithm. During acquisition, the heart is being located automatically and both endo and epicardial contours are segmented without user interaction. In the end, both images and analysis report can be visualized. The other two solutions, *Cardiac Explorer* and *ReportCard 4.0*, are not freely described by their manufacturers. Note that all these solutions allow manual correction and the inclusion or exclusion of TPMs according to the user selection.

Besides machine vendors' software, also independent solutions are currently available, namely *CMRTools* (Cardiovascular Imaging Solutions, United Kingdom), *QMass MR* (Medis, Netherlands), *4D LV-Analysis MR* (TomTec, Germany), *cmr*^{42} (Circle Cardiovascular Imaging, Canada), *CAAS MRV* (PIE Medical Imaging, Netherlands) and *Segment CMR* (Medviso, Sweden). As an example, *CMRTools* uses a semi-automated framework, requiring both SAX and LAX views to be used for analysis. The user identifies the apex and the LV blood pool axis (in a LAX view) and then an automated endo and epicardial delineation is performed. Afterwards, the user can control an intensity-based thresholding tool to distinguish blood pool from TPMs, therefore including these in the myocardial mass rather than in the cavity volume. Before computing the cardiac indices and to correct for longitudinal contraction, the motion of the mitral valve plane should be defined by the user [52]. In summary, the majority of these solutions incorporate long-axis motion correction by including LAX views in the analyses to optimize the short-axis contours. For this process (mitral valve positioning) or for LV localization, usually some degree of user interaction is still required to obtain accurate results. Nevertheless, manual contouring tools are also available for correction of automated contours or complete manual delineation, if preferred.

2.4 B-spline Explicit Active Surfaces (BEAS)

Recently, Barbosa *et al.* [47] proposed the B-spline Explicit Active Surfaces (BEAS) framework with the intent to achieve real-time 3D segmentation. This framework arises from the fusion of three previously presented formalisms [Figure 2.4]: the variational B-spline level-set formulation of Bernard *et al.* [112], the Active Geometric Functions (AGFs) of Duan *et al.* [113] and the localized region-based active contours of Lankton and Tannenbaum [98].

As stated in Section 2.2.3, active contours were initially presented as a variational framework where the shape to be recovered is captured by propagating an evolving interface [95]. Later, the level-set framework [96] was proposed to handle topological changes by describing the contour as the zero level of a higher-dimensional function. However, by increasing the dimensionality of the problem, it increases the computational cost. Although strategies like narrow-banding or fast marching schemes were later proposed to optimize its evolution, level-sets remain a computationally demanding approach [113]. To overcome such problem, two new formulations were recently proposed. Bernard *et al.* [112] presented a variational B-spline level-set formulation, where the implicit level-set function is modeled as a combination of B-spline basis functions and its minimization is expressed as a sequence of 1D convolutions. Therefore, an efficient algorithm is obtained, while still keeping the topological flexibility of level-sets. In parallel, Duan *et al.* [113] proposed an explicit representation of active contours using geometric functions and, therefore, reduced the dimensionality of the segmentation problem, yielding real-time segmentation. However, such computational advantage brought topological limitations due to the explicit formulation employed. For further principles, mathematical background and applications description on active contours and level-sets, the reader is referred to subject-specific literature, such as the seminal books written by Stanley Osher [114, 115].

Concerning the used energy functional, the first methodologies used edge-based terms, making the segmentation sensitive to noise and dependent on the initial position of the contour [116]. To mitigate such problems, Chan and Vese [116] proposed their “active contours without edges” by using global region-based energies. Instead of depending on the gradient of the image, it assumes nearly piecewise-constant regions and use regional properties inside and outside the object to evolve the contour. Thus, it increases the robustness against initial curve placement and giving robustness to image noise. Notwithstanding, global region-based energies fail to segment heterogeneous objects. To this end, Lankton and Tannenbaum [98] proposed a localized region-based formulation, considering a local region around each contour point to locally evolve it. However, such localization increases the associated computational cost.

Based on these formulations, the BEAS framework [47] was proposed by expanding AGFs to a B-spline formulation [Figure 2.4] and, thus, presenting several advantages, namely:

- it achieves real-time performance for 3D segmentation by expressing the active contours evolution as a succession of fast 1D convolutions;

- it allows explicit control over the smoothness of the interface through the scale factor of the underlying B-spline formulation, without requiring regularization terms to be added to the energy (implicit smoothing);
- it allows using local and global region-based energies initially designed for level-set framework by relating both explicit and implicit formulations.

In terms of formalism, the key concept is to regard the boundary of an object as an explicit function, where one of the coordinates of the points within the surface, $x = x_1, \dots, x_n$, is given explicitly as a function of the remaining coordinates, i.e. $x_1 = \psi(x_2, \dots, x_n)$. Such explicit representation of the interface limits the topology flexibility, which is a mild constraint for the goal of this work as only one connected object, the myocardium, needs to be segmented. Moreover, it can be seen as introducing prior information in the model since the segmented object will have the topology induced by the coordinate system (and associated geometric function used) [47]. According to this framework [47], ψ is defined as a linear combination of B-spline basis function:

$$x_1 = \psi(x_2, \dots, x_n) = \psi(\boldsymbol{x}^*) = \sum_{k \epsilon \mathbb{Z}^{n-1}} c[\boldsymbol{k}]\beta^d\left(\frac{\boldsymbol{x}^*}{h} - k\right) \qquad (2.1)$$

where $\beta^d(.)$ is the uniform symmetric $(n-1)$-dimensional B-spline of degree *d*. The knots of the B-spline are located on a rectangular grid defined on the chosen coordinate system, with a regular spacing given by *h*. The coefficients of the B-spline representation are gathered in $c[\boldsymbol{k}]$, which controls the object's surface. Therefore, the energy minimization is performed with respect to these B-spline coefficients, ultimately yielding the desired segmentation.

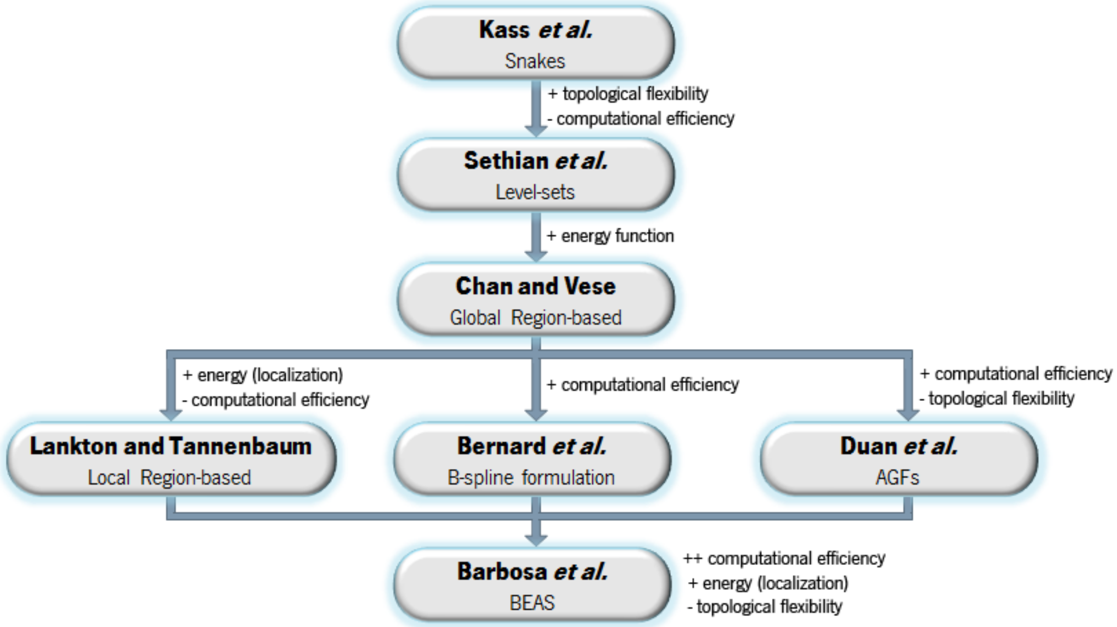
Kass et al.
Snakes
+ topological flexibility
- computational efficiency
Sethian et al.
Level-sets
+ energy function
Chan and Vese
Global Region-based
+ energy (localization)
- computational efficiency
+ computational efficiency
+ computational efficiency
- topological flexibility
Lankton and Tannenbaum
Local Region-based
Bernard et al.
B-spline formulation
Duan et al.
AGFs
Barbosa et al.
BEAS
++ computational efficiency
+ energy (localization)
- topological flexibility

Figure 2.4 - Overview of the evolution towards B-spline Explicit Active Surfaces (BEAS).

3. Methodology

3. Methodology

3.1 General Overview

The ultimate goal of the present thesis was to obtain an accurate and fast 3D+time LV segmentation framework for CMR datasets, in order to assess both cardiac morphology and global function. To this end, based on the studied state-of-the-art methods, we propose to divide our approach into three conceptual blocks [Figure 3.1].

The first block corresponds to an automatic 2D mid-ventricular segmentation, divided in two modules. The first one focuses on obtaining an initial contour for a mid-ventricular slice at the ED phase. Hereto, a fast and robust automatic initialization procedure is proposed (Section 3.2). The second module uses the BEAS framework to segment the considered mid-ventricular slice. As stated in Section 2.2.3, the energy functional is the main factor for an accurate segmentation, thus a specifically designed energy for SSFP CMR images was developed (Section 3.3).

The second block focuses on 3D segmentation for the ED phase. Again, two modules should be addressed to accomplish this task. The first one comprehends an automatic stack initialization to obtain initial contours for all slices covering the LV (Section 3.4). The second one presents a 3D extension of the BEAS framework to effectively segment these slices (Section 3.5). Once more, the energy functional was designed to best match the needs of CMR images.

At last, the third block focuses on tracking the segmented contours of the ED phase over all cardiac phases, ultimately obtaining both endo and epicardial contours at the ES phase (Section 3.6). To this end, two strategies have been compared, namely a local tracking methodology and a global tracking method.

Using the resulting delineations, one is able to compute several clinical cardiac indices, namely end-diastolic volume, end-systolic volume, stroke volume, left ventricular mass and ejection fraction, with a fully automatic pipeline.

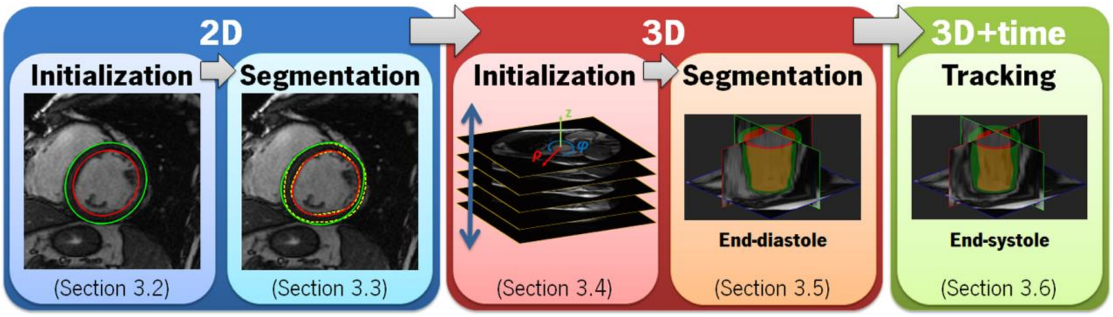

Figure 3.1 - General overview of the proposed fully automatic 3D+time myocardial segmentation framework for CMR datasets.

3.2 Automatic Mid-ventricular Initialization

In order to effectively segment the LV, its location and its approximate shape and/or size are required for constraining the segmentation process in a given region of interest. However, the variability in LV shape, myocardial thickness, image intensities and contrast seen in CMR images hampers automatic LV detection [29]. In many cases, such initialization demands user input to obtain accurate results and surpass the abovementioned challenges. Nevertheless, we intend to develop an automatic initialization algorithm consisting in two steps. The first step focuses on the LV localization in a mid-ventricular slice, in order to define a ROI centered in the left ventricle. Despite many authors propose to first detect the heart and afterwards detect the LV [104, 106, 107], we aim to directly locate the left ventricular cavity using prior knowledge about its relative intensity and shape. After locating the cavity, the second step of the initialization algorithm focuses on obtaining two initial contours of the endocardium and epicardium to be used in the subsequent segmentation (Section 3.3). In summary, we propose to combine and improve the two methods described in [67] and [110] to develop a fast automatic initialization approach capable of detecting LV elliptical annular shapes. Note that we propose to address the initialization problem only in the mid-ventricular level at ED phase to reduce possible variability, to increase the robustness of our assumptions and, therefore, to increase the method's feasibility. After dealing with the mid-ventricular slice, one can use the added knowledge to better initialize and segment the remaining slices covering the LV (Section 3.4 and 3.5).

3.2.1 LV Localization

To detect the LV centroid, Lu *et al.* [67] binarize a mid-ventricular slice using Otsu thresholding [117] and analyze each object in the brighter class [Figure 3.2]. The more circular object, evaluated based on a roundness metric, is assumed to be the LV cavity. However, the method is highly dependent on the binarization, which may fail due to other structures in the image or due to artifacts [Figure 3.2D].

In order to increase the feasibility and robustness of the LV localization step, we propose to improve Lu's method by replacing the classical Otsu thresholding by its multilevel version [117], followed by a more comprehensive search procedure. Thus, we assume that the image's content can be divided into four classes: blood, soft tissues (myocardium plus surrounding tissues), background and one related to artifacts. Moreover, three other assumptions are made, namely: 1) the heart is nearly in the center of the mid-ventricular image, as it is the object of interest and is usually centered during image acquisition; 2) the LV cavity is more circular than

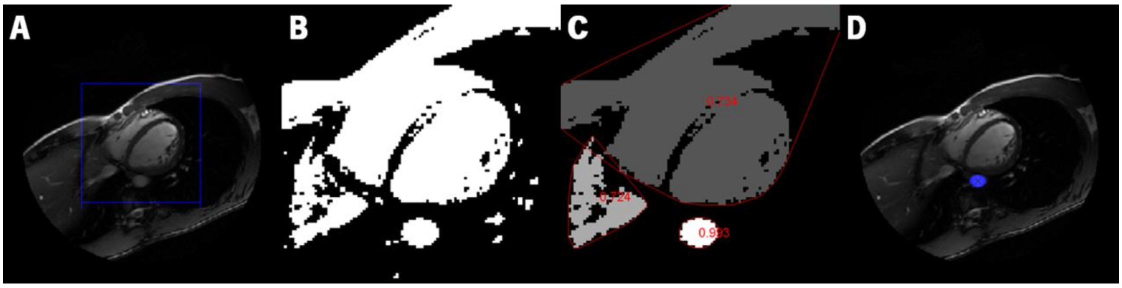

Figure 3.2 - LV localization algorithm proposed by Lu *et al.* [67].
(A) Original image and used ROI; **(B)** Otsu thresholding; **(C)** LV object search, computing the roundness metric (values in red) for each object's convex hull (red lines); and **(D)** detected LV object and its centroid.

the right ventricle (RV) cavity, allowing to distinguish them based on their shape; and 3) the blood intensity is higher than the myocardial one in the used images (SSFP sequences), although no intensity relation between RV and LV blood pools is assumed.

First, a centered, fixed rectangular ROI is specified with half the image size [Figure 3.3A], which takes into account the assumed central position of the heart in the image. Then, a multilevel Otsu thresholding [117] is used to divide the image in four classes [Figure 3.3B]. In the multilevel Otsu thresholding, an exhaustive search for optimal intensity thresholds that minimize the inter-class variance is performed in order to divide the image histogram into *N* classes of pixels [117]. Obviously, the subsequent object's analysis should be adapted to account for the increased number of classes and for the possible division of the structures across these classes. Since the blood pool is usually the brightest object in the image, it is expected to be included in the brighter class. However, the presence of artifacts can shift the LV cavity to the second brightest class. Moreover, if heterogeneities exist due to blood flow, it can even be divided between the two brightest classes. At last, in the cases where strong artifacts exist, the LV cavity can be shifted to the third brightest class. Thus, the subsequent analysis includes 3 independent images: one with the brighter class alone, a second combining the two brightest classes and a third with only the third brightest class [Figure 3.3C]. The background in the fourth class is always discarded, usually associated with air signal intensity (e.g., lungs).

After obtaining the 3 referred images, the objects of each image are filtered to remove the smallest ones (a threshold empirically set to 150 pixels) and the convex hull of the remaining ones is computed. The filter step reduces the computational burden of the method by discarding small objects, hardly corresponding to the LV blood pool, from the subsequent analysis. To locate the LV cavity, the roundness metric [67] of each considered object is calculated using both area (A_i) and perimeter (P_i). This metric measures the approximation of the object's shape to a circle (in a range of 0 to 1). To improve the method's accuracy, the distance of the objects' centroid to

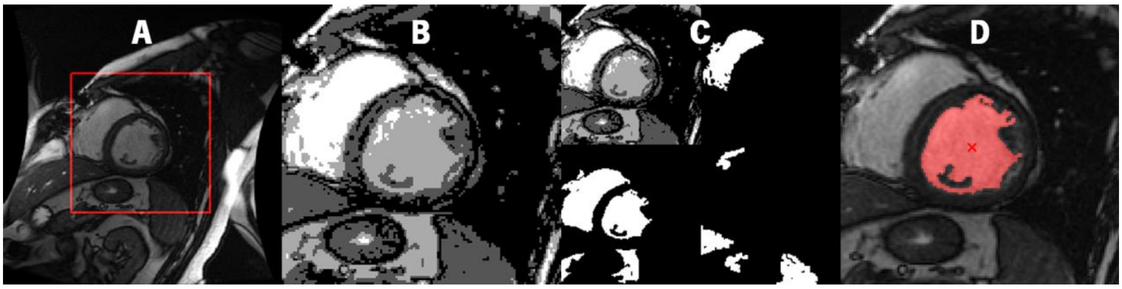

Figure 3.3 - Proposed LV localization algorithm.
(A) Original image and used ROI; **(B)** multilevel Otsu thresholding; **(C)** class decomposition for LV object search (from left to right and top to bottom: multilevel Otsu thresholding, brighter class, two brightest classes combined and third brightest class); and **(D)** detected LV object and its centroid based on equation (3.1).

the image center is added and used as feature to locate the cavity. Therefore, the LV blood pool, and its centroid, is identified as the object with highest C_i value [Figure 3.3D], defined as:

$$C_i = \frac{4\pi A_i}{P_i} + d_i \tag{3.1}$$

where $\frac{4\pi A_i}{P_i}$ is the roundness metric and d_i is the normalized distance of centroid i to the image's center.

3.2.2 Elliptical Annular Template Matching Algorithm

After locating the LV cavity, its size and shape has to be estimated to initialize two contours to be used in the segmentation. Instead of roughly delineating the endocardial boundary and, subsequently, the epicardial one (as stated in Section 2.2.1), we propose to use an object detection technique (Section 2.2.7) to identify the myocardium and obtain both contours in a single step. Since the myocardium has a darker appearance compared to both blood pools in SSFP sequences, a radially-symmetric kernel modeling a dark ring was used by Ciofolo *et al.* [110] to detect the myocardium and initialize both endo and epicardial contours. However, their template matching fails to detect elliptical LV shapes, as only a circular ring is considered.

We propose to improve their template matching by applying an affine transformation (scaling plus rotation) to the used kernel, thus obtaining a dark elliptical ring, which theoretically increases the overall LV detection robustness. The key idea is to create several kernels describing different possible shapes, thicknesses and sizes of the myocardium and apply a template matching algorithm to detect the optimal fitting. Therefore, we construct kernels of different radii (ρ) and standard deviations (σ, according the expected wall thickness) and an affine transformation is applied for different orientations (θ) and major/minor axis ratios (major and minor axis radii as a and b, respectively), using the following equations (based on cartesian to polar space conversion, image coordinates mapping and inverse transformation):

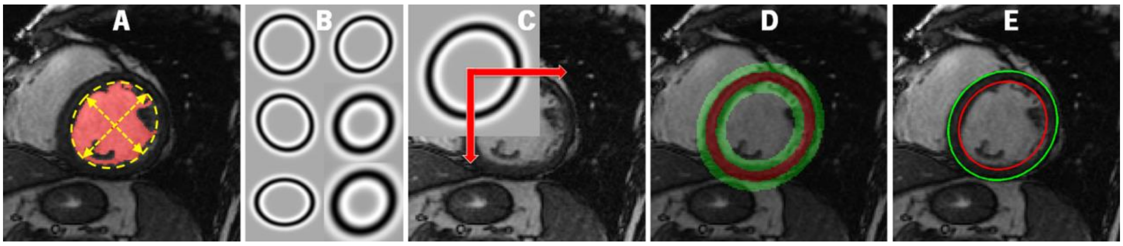

Figure 3.4 - Annular template matching algorithm.
(A) LV object from LV localization, overlay with fitted ellipse and estimated major and minor radius; **(B)** several constructed kernels for template matching with different orientations, radius, standard deviations and ellipse eccentricities; **(C)** principle of block matching strategy using normalized cross correlation; **(D)** original image overlay with optimal kernel; and **(E)** resulting elliptical initial contours.

$$f_\rho(x,y) = f_\rho(r) = \Delta\left(\frac{1}{\sigma\sqrt{2\pi}}e^{-\frac{(r-\rho)^2}{2\sigma^2}}\right) \tag{3.2}$$

$$f_{\rho,T}(x,y) = f_\rho(T^{-1}_{\theta,a,b}(x,y)) = f_\rho\left(\begin{bmatrix}\left(b/_a\right)\times cos\,\theta & -sin\,\theta\\ \left(b/_a\right)\times sin\,\theta & cos\,\theta\end{bmatrix}^{-1}\cdot\begin{bmatrix}x\\y\end{bmatrix}\right) \tag{3.3}$$

To reduce the search space, the detected object from the LV localization method is used to fit an ellipse and estimate the major axis radius and orientation [Figure 3.4A]. We then use 5 orientations around the estimated one (0, ±45° and ±90°). Moreover, 3 variations of the measured radius combined with 4 standard deviations allow covering the myocardial size and thickness range, while also accounting for errors in the estimated radius. Finally, 4 axes ratios are used to consider different ellipse eccentricity values to best fit the subject-specific LV shape. In total, 240 kernels will be considered in the analysis [Figure 3.4B]. For every constructed kernel, a block matching search within the image ROI is performed using normalized cross correlation [Figure 3.4C]. The position maximizing the cross correlation value defines the optimal center for the kernel under evaluation. The kernel having the maximum cross correlation value among all kernels analyzed [Figure 3.4D] then defines the optimal center, orientation, radius and axes ratio, used to draw two ellipses to be used as initial contours [Figure 3.4E].

3.3 Coupled Myocardial 2D Segmentation

In this section, a 2D version of the B-spline Explicit Active Surfaces [47] framework will be described for segmenting the mid-ventricular slice. Within this framework, several details should be addressed to obtain accurate results, namely the properties of the energy functional used, the employed formulation for both endo and epicardial contours and the control over the contours' smoothing.

3.3.1 Endocardial and Epicardial Contour Coupling

In typical active contour formulations, the endo and epicardial boundaries are defined separately and additional penalties guarantee their coupling [63, 74]. Since the segmentation is assessed in both endo and epicardial interfaces, a coupled formulation would allow controlling the contours' evolution towards a global optimum. Inspired by the strategy used in [118] for LV segmentation in US images, we model the endo and epicardial contours as a combination of two explicit functions representing the myocardial wall position and wall thickness [Figure 3.5], respectively. Thereby, each contour is defined as:

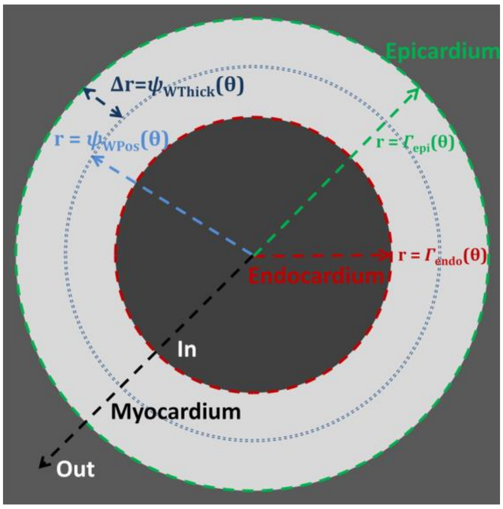
Epicardium
$\Delta r=\psi_{WThick}(\theta)$
$r = \psi_{WPos}(\theta)$
$r = \Gamma_{epi}(\theta)$
$r = \Gamma_{endo}(\theta)$
Endocardium
In
Myocardium
Out

Figure 3.5 - Conceptual diagram of the coupled formulation used to represent both endo and epicardial contours [118].

$$\Gamma_{endo}(\theta) = \psi_{W_{Pos}}(\theta) - \psi_{W_{Thick}}(\theta) \tag{3.4}$$

$$\Gamma_{epi}(\theta) = \psi_{W_{Pos}}(\theta) + \psi_{W_{Thick}}(\theta) \tag{3.5}$$

where $\psi_{W_{Pos}}(\theta)$ gives the center position of the myocardial wall (dashed light blue line in Figure 3.5) as a function of θ and $\psi_{W_{Thick}}(\theta)$ encodes half of the myocardial wall thickness. Both Γ_{endo} and Γ_{epi} act as interfaces between the blood pool (in), the myocardium (myo) and the surrounding structures (out). Note that this representation is defined in the polar domain and therefore the geometric function used in BEAS is defined as $r = \psi(\theta)$.

The fundamental advantage of such formulation is that, by applying different scales to $\psi_{W_{Pos}}(\theta)$ and $\psi_{W_{Thick}}(\theta)$, one can implicitly smooth the local variation of the myocardial thickness (in order to keep it smooth) without affecting the overall ability to capture more complex myocardial shapes [118]. In other words, there are two distinct degrees of freedom to control the myocardium shape and thickness smoothing. Moreover, it allows global shape constraints to be applied as shape penalties in the energy functional, controlling the coupled segmentation instead of each separated contour [118] and increasing the algorithm robustness by driving the segmentation towards a combined global optimum.

3.3.2 2D Region-based Energy Functional

As described in Section 2.4, Lankton and Tannenbaum [98] have recently introduced the concept of localized region-based energies, which overcome the limitations of classical edge-based and global region-based energy functionals. The idea is that objects with heterogeneous statistics can be successfully segmented by analyzing a local region around each point. In this sense, it assumes local homogeneous regions, although no assumption of global uniform regions is made. By considering each point separately, each contour point evolves based on its own local regional statistics, so as to minimize the combined global energy [98]. In order to compute these statistics, a local neighborhood has to be considered and afterwards separated into local interior and local exterior regions according to the curve's position at a given iteration. Figure 3.6 schematically represents the principle of localized region-based energies considering a squared neighborhood. One should keep in mind that the computation of local statistics is associated with an increased computational cost compared to global region-based energies. Moreover, localized energies are inherently more sensitive to the initial contour position than their global counterparts. Therefore, and besides ensuring a good initialization, the size of the chosen neighborhood region should be defined based on the scale of the object of interest and the presence and proximity of surrounding structures [98].

In CMR images, the left ventricle appears as a heterogeneous structure due to noise, blood flow and the presence of TPMs. In this sense, localized region-based energies seem to be the primary choice for its segmentation. We thus propose to use two different localized region-based energies for the endo and epicardial contours by taking into account their respective characteristics. Since the cavity is always brighter than the myocardial tissue in SSFP sequences, a signed version of the localized Yezzi (LY) energy [98] is used for the endocardial contour (henceforward referred as signed localized Yezzi – SLY). This energy explicitly introduces the expected intensity relation between in and myo regions, forcing the contour to evolve towards

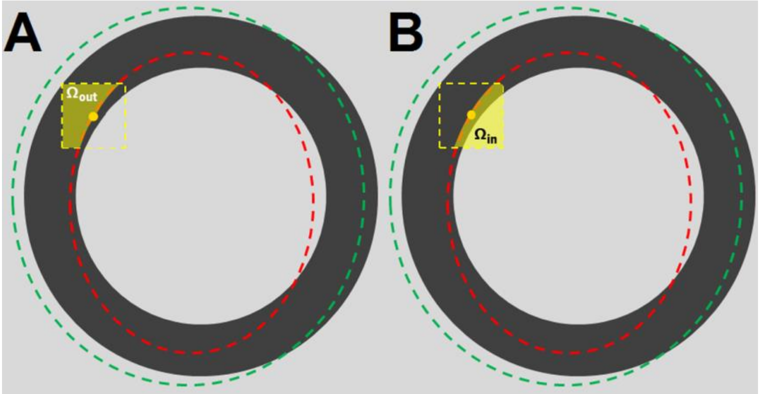

Figure 3.6 - Principle of localized region-based energies.
The squared region corresponds to the neighborhood of the contour point (yellow dot), separated according to the contour's position into **(A)** local exterior ($\boldsymbol{\Omega_{out}}$) and **(B)** local interior ($\boldsymbol{\Omega_{in}}$) regions, whose statistics are later used to evolve the contour.

an interface whose internal region is brighter than the external one. On the other hand, since the external region (out) is relatively unpredictable due to the variability in structures encountered (e.g., lungs, RV or soft tissues – [Figure 3.3A]), an unsigned constant intensity model is chosen by using the localized Chan-Vese (LCV) energy [98]. Besides the choice of signed or unsigned version, LY and LCV energies slightly differ on their segmentation principles. While the LCV energy assumes two uniform regions and tries to find the contour for which the interior and exterior regions best approximate two given local means, LY energy relies on the assumption that the two regions should have maximally separate mean intensities, so that local internal and external means have the largest difference possible [98]. Therefore, the Yezzi energy is suitable for endocardial segmentation as two distinct signal intensities are expected, although not applicable for epicardium as no assumption can be made (e.g., myocardium and surrounding tissues can have locally similar signal intensity means). On the other hand, the Chan-Vese energy only tries to find a local homogeneous separation, being suitable for epicardial segmentation.

Additionally, the localized energy functionals were modified by adding weights to the inner and outer regions of the endocardial and epicardial interfaces, respectively. This weighted formulation allows an explicit control over the equilibrium point in between the two regions, therefore pushing the contour towards the myocardial region if a weight smaller than one is considered [Figure 3.7A]. In practice, this strategy mimics the physician's knowledge when manually contouring, where they place the contours closer to the myocardium to avoid TPMs to be included in this region, as illustrated in Figure 3.7B-C.

Given the topology of the segmentation problem, the proposed energy functional is defined as:

$$E = \int_{\Gamma_{endo}} \bar{f}_{endo}(\boldsymbol{x}^*) d\boldsymbol{x}^* + \int_{\Gamma_{epi}} \bar{f}_{epi}(\boldsymbol{x}^*) d\boldsymbol{x}^* \tag{3.6}$$

where

$$\bar{f}_{endo}(\boldsymbol{x}^*) = u_{x,myo} - \omega_{in}. u_{x,in} \tag{3.7}$$

$$\bar{f}_{epi}(\boldsymbol{x}^*) = \bar{f}_{myo}(\boldsymbol{x}^*) H_{\phi_{epi}}(\boldsymbol{x}^*) + \bar{f}_{out}(\boldsymbol{x}^*) \left(1 - H_{\phi_{epi}}(\boldsymbol{x}^*)\right) \tag{3.8}$$

$$\bar{f}_{myo}(\boldsymbol{x}^*) = \left(\bar{I}(\boldsymbol{x}^*) - u_{x,myo}\right)^2 \tag{3.9}$$

$$\bar{f}_{out}(\boldsymbol{x}^*) = \omega_{out}. \left(\bar{I}(\boldsymbol{x}^*) - u_{x,out}\right)^2 \tag{3.10}$$

and ω_i is the scalar weight applied to the region i; $u_{x,in}$, $u_{x,myo}$ and $u_{x,out}$ represent the local intensity means in the vicinity of x for the inner, myocardial and outer regions, as defined in [98],

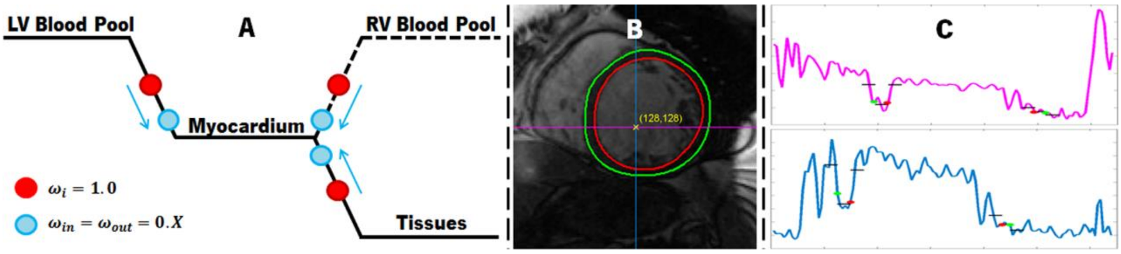

Figure 3.7 - Principle of the proposed weighted localized region-based energies. **(A)** Schematic representation of the weights influence in the proposed weighted energy functionals. **(B)** Example of a mid-ventricular CMR image with manual reference contours. **(C)** Two profile of the image in (B) with indication of reference contour points (indicated in red and green) and local means of $\boldsymbol{in}$, $\boldsymbol{myo}$ and $\boldsymbol{out}$ regions (indicated in black).

respectively. H_{ϕ_j} is the Heaviside operator applied to the level-set like function $\phi_j(x) = \Gamma_j(x^*) - x_1$, representing the region inside the interface j. Moreover, considering a generic function $h(x)$ in $\mathbb{R}^n$, note $\bar{h}$ as the restriction of h over interface Γ. Thus, $\bar{I}(x^*)$ corresponds to the image value at position $x = \{\psi(x^*), x_2, \dots, x_n\}$. Equations (3.7) and (3.8) represent the weighted SLY and LCV energies, respectively. These energies directly influence the resulting segmented object.

Since the model is defined based on the myocardial wall position and thickness, the evolution of the myocardial region can be expressed as:

$$\frac{\partial E}{\partial \psi_{W_{Pos}}} = \frac{\partial E}{\partial \Gamma_{endo}} + \frac{\partial E}{\partial \Gamma_{epi}} \tag{3.11}$$

$$\frac{\partial E}{\partial \psi_{W_{Thick}}} = -\frac{\partial E}{\partial \Gamma_{endo}} + \frac{\partial E}{\partial \Gamma_{epi}} \tag{3.12}$$

Moreover, given the B-spline formulation of BEAS, it can be shown that the energy is directly minimized through the optimization of the B-spline coefficients $c[\boldsymbol{k}]$. This implies the computation of the derivative of the chosen energy functional with respect to each B-spline coefficient $c[\boldsymbol{k}_i]$ [47]. In this sense, the derivative of the energy function with respect to the B-spline coefficients encoding the wall position and wall thickness, respectively, is expressed as:

$$\frac{\partial E}{\partial c_{W_{Pos}}[\boldsymbol{k}_i]} = \frac{\partial E}{\partial \psi_{W_{Pos}}} \cdot \frac{\partial \psi_{W_{Pos}}}{\partial c_{W_{Pos}}[\boldsymbol{k}_i]} \tag{3.13}$$

$$\frac{\partial E}{\partial c_{W_{Thick}}[\boldsymbol{k}_i]} = \frac{\partial E}{\partial \psi_{W_{Thick}}} \cdot \frac{\partial \psi_{W_{Thick}}}{\partial c_{W_{Thick}}[\boldsymbol{k}_i]} \tag{3.14}$$

Thus, using the energy functionals for endo and epicardial contours proposed above, the energy minimization process can be achieved using the following evolution equations:

$$\frac{\partial E}{\partial c_{W_{Pos}}[\boldsymbol{k_i}]} = \int_{\Gamma_{endo}} \bar{g}_{endo}(\boldsymbol{x}^*)\beta^d\left(\frac{\boldsymbol{x}^*}{h} - \boldsymbol{k_i}\right)d\boldsymbol{x}^* + \int_{\Gamma_{epi}} \bar{g}_{epi}(\boldsymbol{x}^*)\beta^d\left(\frac{\boldsymbol{x}^*}{h} - \boldsymbol{k_i}\right)d\boldsymbol{x}^* \quad (3.15)$$

$$\frac{\partial E}{\partial c_{W_{Thick}}[\boldsymbol{k_i}]} = -\int_{\Gamma_{endo}} \bar{g}_{endo}(\boldsymbol{x}^*)\beta^d\left(\frac{\boldsymbol{x}^*}{h} - \boldsymbol{k_i}\right)d\boldsymbol{x}^* + \int_{\Gamma_{epi}} \bar{g}_{epi}(\boldsymbol{x}^*)\beta^d\left(\frac{\boldsymbol{x}^*}{h} - \boldsymbol{k_i}\right)d\boldsymbol{x}^* \quad (3.16)$$

where

$$\bar{g}_{endo}(\boldsymbol{x}^*) = \left(\frac{\bar{I}(\boldsymbol{x}^*) - u_{x,myo}}{A_{u_{myo}}}\right) - \left(\frac{\bar{I}(\boldsymbol{x}^*) - \omega_{in}.u_{x,in}}{A_{u_{in}}}\right) \quad (3.17)$$

$$\bar{g}_{epi}(\boldsymbol{x}^*) = \bar{f}_{myo}(\boldsymbol{x}^*) - \bar{f}_{out}(\boldsymbol{x}^*) \quad (3.18)$$

and $A_{u_{myo}}$ and $A_{u_{in}}$ are the areas of the myocardial and inner regions used to estimate the local means $u_{x,myo}$ and $u_{x,in}$, respectively [98]. Equations (3.17) and (3.18) reflect the features of the myocardial boundaries to be segmented (derived from SLY and LCV energies, respectively), being denominated feature functions.

3.4 Automatic Stack Initialization

The previous sections focused on obtaining an accurate and automatic segmentation for a mid-ventricular slice in the ED phase. Notwithstanding, the goal of the present framework is to segment all SAX slices from base to apex and from ED to ES, which demands a previous initialization in these slices. As stated in Section 3.2, the proposed automatic 2D initialization algorithm was designed to address the initialization problem only in the mid-ventricular level, presenting limitations when applied to other slices (e.g., myocardium at basal and apical levels differs in shape and in the surrounding structures). Nevertheless, the knowledge from the previous 2D segmentation can be used to initialize the remaining slices. In this section, an automatic 3D stack initialization is proposed, avoiding the need for a manual initialization which would require a tremendous user input.

A first concern when designing a stack initialization algorithm is related to the choice of the basal and apical slices, in order to confine the initialization to slices covering the LV. Hereto, the proposed framework assumes that the stack is previously cropped during loading or even during acquisition (e.g., like in *Inline VF* from Siemens), therefore avoiding the user interaction in this step. In case this was not done, a simple solution would be to have the user input two points at run-time, corresponding to the choice of the basal and apical slices in the ED phase. Note that this strategy can be regarded as a minor input and is frequently used in commercial software packages (e.g., *CMRTools*, *CAAS MRV*, *Segment CMR*, *Inline VF*, among others) to increase the methods' feasibility and to reduce errors (see Section 2.3).

The simplest initialization would consist of naively using the segmentation results at the mid-ventricular level as initial contours at other slices in the stack, plus a possible scaling to account for the different sizes of the LV SAX cuts from base to apex. However, this approach makes two unreliable assumptions: it first considers that the relative LV size in different slices is known or can be estimated *a priori*; moreover, it assumes the cavity center is always placed in the same position, which may not be true due to the known misalignment of the slices in CMR datasets. Thus, we propose a threshold-based BEAS formulation to initialize both endo and epicardial contours in the full stack, while at the same time estimating the slices misalignment.

The idea is to use the subject-specific intensity information learned in the mid-ventricular level to obtain coarse delineations at other levels. First, we estimate the intensity distribution of the LV cavity and myocardial wall based on the previous segmentation [Figure 3.8A-B]. To this end, the Expectation-Maximization (EM) algorithm [53] is used, assuming a mixture of two gaussians to describe the LV (cavity plus myocardium) histogram. Although the EM algorithm implicitly classifies each pixel according to their probability of belonging to each considered class, we are not interested in this segmentation but instead in the distributions' parameters. In this sense, after estimating these parameters (mean and standard deviation of both classes: cavity

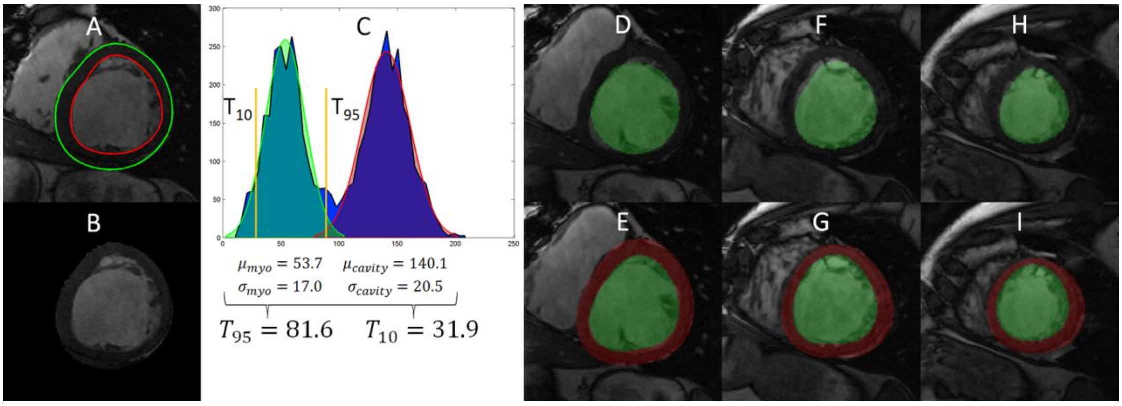

Figure 3.8 - Proposed automatic stack initialization procedure.
(A) Mid-ventricular slice ROI overlay with fully automatic 2D segmentation; **(B)** LV mask obtained using epicardial contour **(C)** LV histogram, corresponding intensity distributions' parameters estimated based on EM algorithm and threshold definition; **(D)**, **(F)** and **(H)** coarse delineation of the endocardium using threshold-based BEAS; **(E)**, **(G)** and **(I)** final initialization for both endo and epicardial contours using coupled threshold-based BEAS. Note that (D) and (E) represent a basal slice, (F) and (G) a mid-ventricular one and (H) and (I) an apical slice.

and myocardium), two thresholds are defined, namely the minimum cavity intensity (T_{95}) and the minimum myocardium intensity (T_{10}) thresholds [Figure 3.8C]. Due to the presence of TPMs and because they should be included in the blood pool, the cavity's distribution is discarded and only the myocardial one is used to define both thresholds. The cavity intensity threshold is defined as the 95 percentile of the myocardial distribution, which is a sufficiently high value to capture the full blood pool plus TPMs, but avoids the contour leakage to the myocardium. On the other hand, the myocardium intensity threshold is defined as the 10 percentile of the myocardial distribution, allowing the algorithm to capture most of the myocardial wall while avoiding the leakage to darker regions, like the lungs. Then, the two defined thresholds can be used to estimate coarse delineations of the endocardium and the epicardium.

To obtain a coarse delineation of the endocardium, we start by placing an initial circular contour with a small radius (2px) centered in the LV cavity's center of the mid-ventricular slice and we evolve it using the minimum cavity intensity threshold [Figure 3.9A]. If the intensity of the contour point is higher than the threshold, the contour is allowed to grow. In contrast, when it is lower than the threshold, the contour is shrunk. This strategy for contours' evolution is inspired in the simplistic intensity-threshold-based data term presented in [119]. Moreover, at each iteration an additional step is performed focusing on re-initializing the cavity's center and consequently resample the contour in the polar domain. The idea behind this step is to improve the estimated center for each slice independently [Figure 3.9A]. Finally, the evolution stops when the area enclosed by the contour does not significantly change for a few iterations.

We then initialize an epicardial contour with the thickness obtained in the 2D mid-ventricular segmentation and we grow it using the minimum myocardium intensity threshold

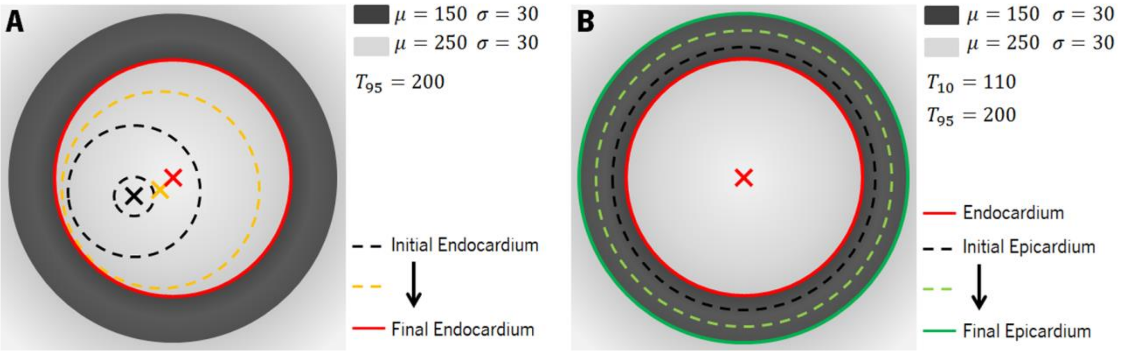

Figure 3.9 - Principle of threshold-based BEAS to obtain coarse endo and epicardial delineations. **(A)** Endocardium delineation by contour's evolution using the minimum cavity intensity threshold ($\boldsymbol{T_{95}}$), with re-initialization of the cavity's center. **(B)** Coupled threshold-based BEAS for epicardial delineation and endocardial contour correction (not shown in this simulated example). Both minimum cavity intensity ($\boldsymbol{T_{95}}$) and minimum myocardium intensity ($\boldsymbol{T_{10}}$) thresholds are used for this stage.

[Figure 3.9B]. To improve the initialization robustness, the coupling strategy described in Section 3.3.1 is used in this second stage. Thus, each contour uses its respective threshold during evolution towards a global optimum. Note that the epicardium uses both thresholds to limit its growth in both sides. This strategy allows the epicardial contour delineation, while also enabling a better endocardial definition by surpassing possible errors in the first stage. Again, the evolution stops when the area enclosed by both contours stays nearly constant for a few iterations. Interestingly, one should note that the implicit smoothing enforced by BEAS is used to smooth the contours while growing, eventually helping surpass papillary muscles during evolution.

The proposed method is applied for each slice in the stack [Figure 3.8D-I], progressively using the LV cavity's center from previously initialized adjacent slices to start the endocardial contour. In the end, it provides a consistent initialization for the subsequent three-dimensional segmentation, while estimating the slices misalignment (given by the center's estimations).

3.5 Coupled Myocardial 3D Segmentation

3.5.1 BEAS 3D Extension

The proposed automatic initialization procedure allows obtaining an initial contour, plus an estimate for the LV cavity's center, for each slice. Using such initialization, the segmentation could be independently applied in each of them. However, it would not take into account the known spatial continuity of the left ventricle. Thus, a 3D segmentation enforcing a spatial continuity allows a more robust segmentation, minimizing possible errors in individual slices. Although we could directly segment the stack of slices, the spatial continuity and smoothing along the third dimension would result in unpredictable shapes due to the misalignment. We thus propose to correct the misalignment prior to the segmentation by considering the LV cavity's centers estimated during the stack initialization. To this end, a translation is applied for each slice correcting the center's position, resulting in a straight LV axis, as illustrated in Figure 3.10, and therefore allowing a true three-dimensional modeling of the LV surface.

The idea is to extend the BEAS framework towards a 3D segmentation in order to enforce spatial continuity and obtain higher accuracy. Taking into account the BEAS formulation [47], an important step towards the 3D LV modeling is the choice of an appropriate coordinate system. As the CMR slices have a relatively large thickness, considering a spherical coordinate system (which would be the most straightforward BEAS extension) is unfeasible, since image data is highly anisotropic and the pixel intensities between slices can't be reliably estimated. Therefore,

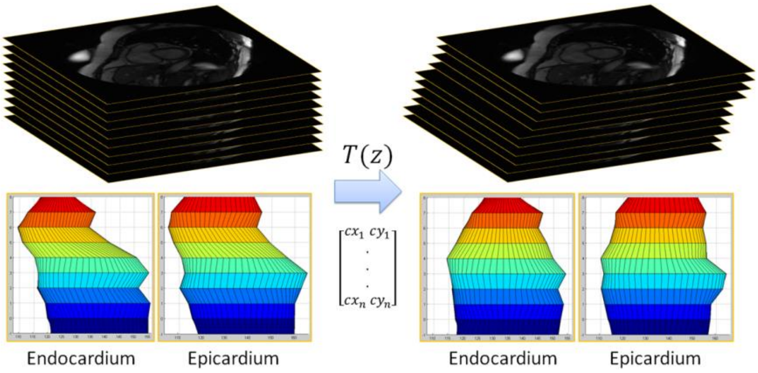
$T(z)$
$\begin{bmatrix} cx_1\ cy_1 \\ \vdots \\ cx_n\ cy_n \end{bmatrix}$
Endocardium
Epicardium
Endocardium
Epicardium

Figure 3.10 - Misalignment correction based on the LV cavity's center estimated during stack initialization.

we propose to use a cylindrical coordinate system, where the third dimension has only a finite number of possible values corresponding to the number of slices in the cropped stack [Figure 3.11]. At the same time, we improve the formulation introduced in [118] for an implicit coupled propagation by extending it to a three-dimensional parameterization of the myocardial region, making use of the cylindrical topology of the CMR data. Thus, the 3D extension of equations (3.4) and (3.5) yields:

$$\Gamma_{endo}(\theta, z) = \psi_{W_{Pos}}(\theta, z) - \psi_{W_{Thick}}(\theta, z) \tag{3.19}$$

$$\Gamma_{epi}(\theta, z) = \psi_{W_{Pos}}(\theta, z) + \psi_{W_{Thick}}(\theta, z) \tag{3.20}$$

where $\psi_{W_{Pos}}(\theta, z)$ gives the center position of the myocardial wall as a function of θ and slice level z, and $\psi_{W_{Thick}}(\theta, z)$ encodes half of the myocardial wall thickness.

One should note that the proposed formulation only allows the surface points to evolve radially, inside its own initial z-plane. Such constrain is crucial as any inter-slice information is unknown. Moreover, several other points are important to ensure a proper surface evolution. On one hand, extending the local neighborhood to a cubic local volume could lead to incorrect local intensity means calculations due to the data anisotropy and considerable slice thickness. As such, we continue to use an in-slice squared region to update the local intensity means around each interface. On the other hand, the introduction of a new dimension requires an additional B-spline scale to be defined in the BEAS formulation. However, it has to be a low scale to avoid over-smoothing of the 3D surface in the third dimension, as a reduced number of slices are acquired to cover the left ventricle.

3.5.2 3D Hybrid Energy Functional

As stated in Section 2.2.3, the energy functional employed for contours' evolution is vital for an accurate contouring. As such, we propose to design an energy functional that best match

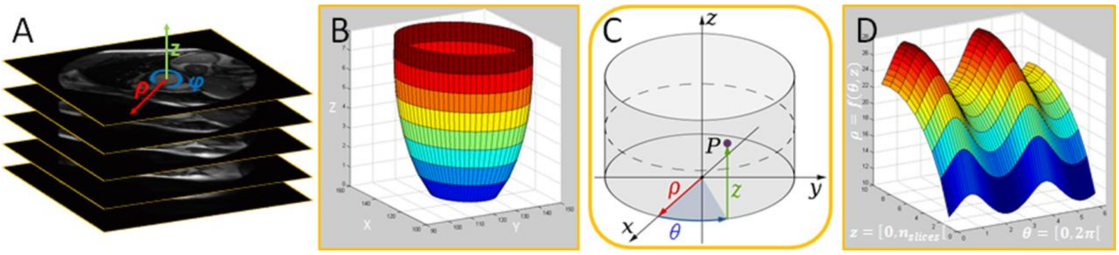

Figure 3.11 - Endocardial LV 3D-surface representation through an explicit function in the cylindrical domain.
(A) Stack of 2D slices; **(B)** LV 3D-surface in Cartesian coordinates; **(C)** Correspondence between the cartesian and cylindrical domains; **(D)** Explicit function in the cylindrical domain.

the needs of CMR images. Although the proposed energy in Section 3.3.2 is suited for the segmentation in mid-ventricular slices, new challenges arise (or become more pronounced) from the inclusion of basal and apical slices in the process. The major remaining challenge concerns the epicardial delineation, where multiple local minima near the boundary may misguide the contours' evolution. Moreover, the outside intensity mean is commonly similar to the myocardial mean (although usually with different variance/homogeneity), preventing contours' evolution towards the right "unseen" boundary when only using region-based energies. This situation is particularly critical in apical slices due to partial volume effects. Similar results are found when the initial contour stays in the middle of the myocardium, which is an almost homogeneous region, as the LCV energy will become null, inhibiting the evolution. These remarks highlight the importance of adding a new energy term, in order to introduce better robustness against initialization and increase the accuracy in finding the correct epicardial boundary.

Due to the contrast in MR images and subsequent clear-sighted edges, several authors use edge-based energy terms to evolve the contours and segment the LV [63, 74, 76]. Although such edges are well defined at the endocardium, they usually lead to wrong contouring when TPMs are present unless other strategy is added. In what concerns epicardial boundary, the edges can help during segmentation in septal segments, although weak edges are found in the remaining segments between myocardium and other tissues. Nevertheless, even with this low contrast between myocardium and surrounding structures (e.g., lungs), it can potentially help in epicardial delineation if properly included. Taking this into account, we propose to use a hybrid energy in the epicardial energy functional by introducing an edge-based term besides the region-based one. This term is only applied in the epicardium, because the presence of TPMs in the blood pool may mislead the contour's evolution due to additional edges. Furthermore, as a result of higher contrast between cavity and muscle, the segmentation result in the endocardium is expected to be better than the epicardial one. The proposed edge-based term relies on the computation of an edge map and its subsequent post-processing. Inspired by Lee *et al.* [120], for each slice in the ED phase an edge map is computed following four steps:

1. The image is mapped to polar space using the LV cavity's center estimated during the automatic stack initialization [Figure 3.12B];
2. A Canny edge detector [121] is applied in the polar domain to extract the edge information [Figure 3.12C];
3. A post-processing step is applied to filter the edge information [Figure 3.12D]. In fact, the initial endocardial contour is used to filter out any edge belonging to the cavity's boundary or inner region. Moreover, the edges in more remote regions are also cleaned as they are associated with an unlikely myocardial thickness;
4. The edge energy map is computed by calculating the unsigned distance of every pixel to the closest edge point [Figure 3.12E], which allows improving the edge detection robustness by filling small gaps in missed edges [122].

Unlike GVF method (Section 2.2.3) [99], a contour evolved using our edge map would be unable to converge to boundary concavities. Notwithstanding, in the LV segmentation, this is not a drawback as only convex shapes need to be delineated. Moreover, it still introduces a high capture range, as presented by GVF, without substantially increasing the methods' computational cost. At last, the use of a distance function to map the edges can even be seen as an advantage, as missed edges (due to weak boundaries) can be filled by this process and thus avoiding leakage of the contour during evolution. Such advantage is particularly vital in apical slices with weak edges or in basal slices with left ventricular outflow tract (LVOT). One should note that this effect is even augmented due to the implicit smoothing enforced by BEAS during evolution.

Using the resulting edge energy map, $\Upsilon(\boldsymbol{x})$, as a new term in the epicardial energy, the complete proposed energy functional for 3D segmentation is defined as:

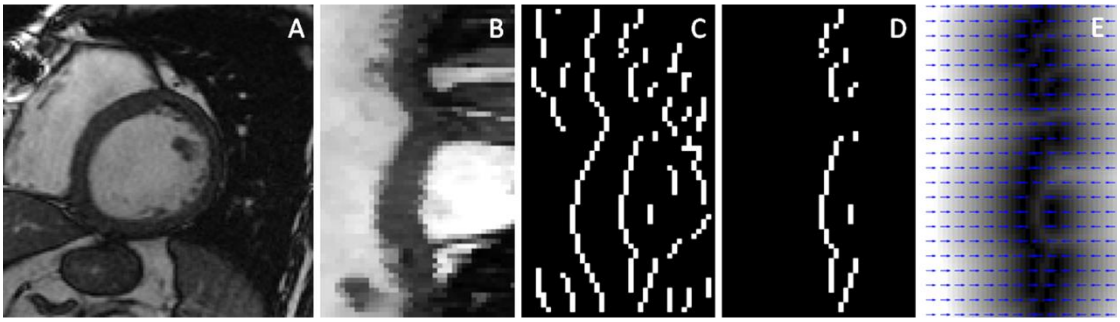

Figure 3.12 - Edge map computation for hybrid epicardial energy functional.
(A) Mid-ventricular slice ROI; **(B)** Image ROI in polar domain; **(C)** Edge information by Canny edge detector; **(D)** Post-processed edge map; **(E)** Edge energy map overlay with radial vector field.

$$E = \int_{\Gamma_{endo}} \bar{f}_{endo}(\boldsymbol{x}^*)d\boldsymbol{x}^* + \int_{\Gamma_{epi}} \left(\bar{f}_{epi}(\boldsymbol{x}^*) + \alpha.\bar{Y}(\boldsymbol{x}^*)\right)d\boldsymbol{x}^* \tag{3.21}$$

where α is a positive hyperparameter to balance the two terms in the epicardial energy.

By applying a similar derivation to the one in Section 3.3.2, the energy minimization process can be achieved using the following evolution equations:

$$\begin{aligned}\frac{\partial E}{\partial c_{W_{Pos}}[\boldsymbol{k_i}]} = &\int_{\Gamma_{endo}} \bar{g}_{endo}(\boldsymbol{x}^*)\beta^d\left(\frac{\boldsymbol{x}^*}{h} - k\right)d\boldsymbol{x}^* \\ &+ \int_{\Gamma_{epi}} \left(\bar{g}_{epi}(\boldsymbol{x}^*) + \alpha.\nabla_r\bar{Y}(\boldsymbol{x}^*)\right)\beta^d\left(\frac{\boldsymbol{x}^*}{h} - k\right)d\boldsymbol{x}^*\end{aligned} \tag{3.22}$$

$$\begin{aligned}\frac{\partial E}{\partial c_{W_{Thick}}[\boldsymbol{k_i}]} = -&\int_{\Gamma_{endo}} \bar{g}_{endo}(\boldsymbol{x}^*)\beta^d\left(\frac{\boldsymbol{x}^*}{h} - \boldsymbol{k_i}\right)d\boldsymbol{x}^* \\ &+ \int_{\Gamma_{epi}} \left(\bar{g}_{epi}(\boldsymbol{x}^*) + \alpha.\nabla_r\bar{Y}(\boldsymbol{x}^*)\right)\beta^d\left(\frac{\boldsymbol{x}^*}{h} - \boldsymbol{k_i}\right)d\boldsymbol{x}^*\end{aligned} \tag{3.23}$$

where $\nabla_r\bar{Y}$ is the edge energy map gradient along the radial direction [Figure 3.12E]. After energy minimization, both endo and epicardial contours in the full stack of slices covering the left ventricle are obtained.

3.6 3D+time Tracking

In the previous sections, a 3D segmentation for all slices covering the LV at the ED phase was achieved, which already allow us to compute end-diastolic volume and left ventricular mass. In order to compute end-systolic volume, stroke volume and ejection fraction, one requires the segmentation to be performed also at the ES phase. Several approaches can be used for this purpose, namely temporal segmentation or tracking procedures. The segmentation approaches focus on delineating the LV in a sequence of images, using specific energy terms for temporal integration [62, 64]. In contrast, tracking-based approaches normally focus on following specific patterns along the sequence of images [80, 123].

The temporal segmentation usually employs a sequential approach for temporal integration, which uses the result from phase t as an initialization for phase $t + 1$ [64]. Thus, the contours would be propagated sequentially and a segmentation step would be applied to properly delineate the contours for the given phase. This approach would assume that the differences between phases (due to contraction of the ventricle) are small in comparison to the local squared region used in our energies. In most cases and as long as the temporal resolution during image acquisition is kept high, such assumption would be valid. Nonetheless, due to the different image characteristics throughout the cardiac cycle (e.g., more pronounced presence of TPMs, less circular shape, among others), the segmentation energy should be redesigned for temporal inclusion [38, 62].

Thus, we propose to use a tracking algorithm to delineate the LV in all cardiac phases. To this end, two approaches will be presented to compare local and global based methods: a profile matching based BEAS inspired by [80] and a global anatomical affine optical flow method, firstly presented for US data [123]. While a localized methodology allows tracking each region separately and accounts for different contraction patterns (present in pathological cases), the global methodology focuses on obtaining a consistent tracking over the cardiac cycle while avoiding contour drifting when there is limited spatiotemporal information. These two methods will be presented and described in the following sections.

3.6.1 BEAS Profile Matching

Hautvast *et al.* [80] presented a fast, robust and accurate propagation method based on profile matching. The method uses the assumption of temporal consistency of the tracked patterns, trying to retain a constant contour environment by matching gray values in profiles perpendicular to the contours. The idea is to use the profile learned by manual contouring at the ED phase to search radially for similar ones in subsequent phases. In their method, each contour (endo or epicardium) is tracked independently over the cardiac cycle. Nonetheless, the same principle has also been previously presented by their colleagues using a coupled strategy [124]. However, their coupled formulation requires a more complex fitting process, as both location and thickness should be adjusted to fit the new image.

We propose to use the profile matching principle to obtain both energy and radial force to drive the contours in a 3D BEAS formulation, which we denominated BEAS Profile Matching (BEASPM). Thus, besides keeping a temporal consistency of patterns, we also ensure a three-dimensional spatial continuity of the contours tracked throughout the cardiac cycle, which was not addressed in [80]. Moreover, due to the implicit smoothing associated with the BEAS framework, one explicitly controls the smoothing of the 3D surface, which potentially reduces errors associated with lack of spatiotemporal information. At last, although each contour’s profile is matched separately, the coupled formulation employed in the framework (see Section 3.3.1 and 3.5.1) ensures a combined global optimization of both endo and epicardial contours during evolution, without requiring explicit constraints over the myocardial thickness.

The profile matching energy, E_{PM}, is computed by considering the sum of absolute differences (SAD) between two radial profiles (at time $t-1$ and t) and a penalization term [Figure 3.13A-F]. Such penalization is designed mainly to avoid large movements, as they are not expected between consecutive frames. Moreover, it avoids over-estimation of the myocardial contraction in the presence of TPMs, which was reported as a drawback of Hautvast and colleagues' method [125]. Thus, denoting I^{t-1} and I^{t} as the intensity images at time $t-1$ and t, respectively, the energy for each contour is given by:

$$E_{PM_j}(x_1, \boldsymbol{x}^*) = \sum_{k=-n_1}^{n_2} \left| I^{t-1}\left(\Gamma_j^{t-1}(\boldsymbol{x}^*) + k, \boldsymbol{x}^*\right) - I^{t}(x_1 + k, \boldsymbol{x}^*) \right| + v_j \left| x_1 - \Gamma_j^{t-1}(\boldsymbol{x}^*) \right| \qquad (3.24)$$

where v_j is a positive hyper-parameter to balance the two terms (SAD and penalization) in the energy functional of each interface j. Moreover, the profiles' size is constant ($n_1 + n_2 = const$) and they are centered on the contours unless a smaller local thickness is present ($n_2 \leq \psi_{W_{Thick}}$ and $n_1 \geq \psi_{W_{Thick}}$ for endo and epicardial contours, respectively). The above equation is used to compute the energy for each slice considered at the ED phase.

By computing the energy gradient in the radial direction, $\nabla_r \bar{E}_{PM_j}$, one obtains a radial force for driving both endo and epicardial contours [Figure 3.13G-H]. The minimization of such energy gives the best global matching surface for a given cardiac phase. Thus, the energy minimization process can be achieved using the following evolution equations:

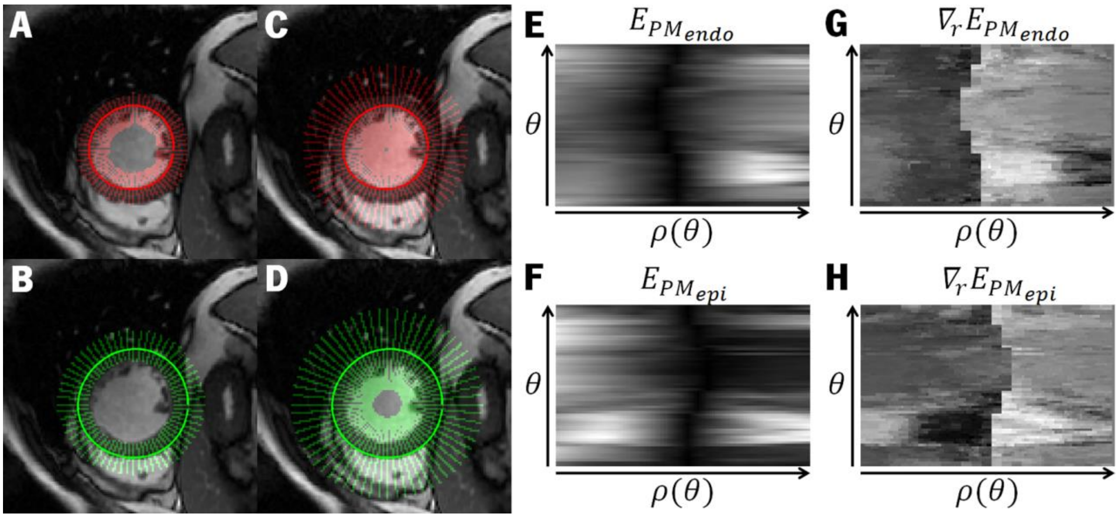

Figure 3.13 - Principle of BEAS Profile Matching (BEASPM) methodology for LV tracking.
(A) Endocardial and **(B)** epicardial reference profiles at reference phase (time $t-1$); **(C)** Endocardial and **(D)** epicardial search profiles at target phase (time t); **(E)** Endocardial and **(F)** epicardial profile matching energy computed using sum of absolute differences and motion penalization; **(G)** Endocardial and **(H)** epicardial radial force for contours' evolution, computed as the energy gradient in the radial direction.

$$\frac{\partial E}{\partial c_{W_{Pos}}[\boldsymbol{k_i}]} = \int_{\Gamma_{endo}} \nabla_r \bar{E}_{PM_{endo}}(\boldsymbol{x}^*)\beta^d\left(\frac{\boldsymbol{x}^*}{h} - \boldsymbol{k_i}\right)d\boldsymbol{x}^* + \int_{\Gamma_{epi}} \nabla_r \bar{E}_{PM_{epi}}(\boldsymbol{x}^*)\beta^d\left(\frac{\boldsymbol{x}^*}{h} - \boldsymbol{k_i}\right)d\boldsymbol{x}^* \tag{3.25}$$

$$\frac{\partial E}{\partial c_{W_{Thick}}[\boldsymbol{k_i}]} = -\int_{\Gamma_{endo}} \nabla_r \bar{E}_{PM_{endo}}(\boldsymbol{x}^*)\beta^d\left(\frac{\boldsymbol{x}^*}{h} - \boldsymbol{k_i}\right)d\boldsymbol{x}^* + \int_{\Gamma_{epi}} \nabla_r \bar{E}_{PM_{epi}}(\boldsymbol{x}^*)\beta^d\left(\frac{\boldsymbol{x}^*}{h} - \boldsymbol{k_i}\right)d\boldsymbol{x}^* \tag{3.26}$$

The propagation is progressively applied to adjacent phases using the previous LV surface, until every cardiac phase has been segmented.

3.6.2 Anatomical Affine Optical Flow

Barbosa *et al.* [123] recently presented a global affine optical flow method for tracking the LV in three-dimensional US data by considering an anatomically constrained affine motion model. The principle is to estimate a global affine motion (translation, rotation, scaling and skew) between two consecutive frames by summing the estimated motion over the reference contour points in the previous frame (initially considering the ED contour). Such constrained estimation only considers anatomical regions of interest by defining a cubic region around each contour point and ultimately avoids the influence of adjacent tissues during motion estimation [Figure 3.14A]. Moreover, by including an iterative displacement refinement scheme, the algorithm is still able to accurately capture large movements [123, 126]. The idea is to sequentially accumulate the estimated displacement fields, thus iteratively reducing the motion left to be estimated.

We propose to use this method for LV tracking in CMR datasets. However, because CMR data is highly anisotropic, the motion can't be reliably estimated in the third dimension. At the same time, describing a three-dimensional ventricle's motion with in-slice movements would lead to overestimation of the displacements in basal and mid-ventricular slices and a motion underestimation in apical slices (note their relative size). Thus, we chose to implement a 2D version of such algorithm and we apply it separately for each slice covering the LV. Furthermore, as both endo and epicardial contours need to be tracked through all phases, the affine motion estimation is performed independently for each contour in a pairwise fashion, starting from the 3D LV surface at the ED phase. Despite performing a two-dimensional motion estimation, since the ED contours were segmented using a 3D formulation and the motion model used integrates information from the entire contour inside each slice (global formulation), a consistent and spatial continuous tracking of the LV surface is expected (although not explicitly enforced).

The principle of optical flow tracking (OFT) is to compute the displacement field of objects in an image based on the assumption that their intensity remains constant [127]. In other words, optical flow assumes that the intensity of a particular point in a moving pattern does not change over time, which implies that any difference in the local appearance of a region over a temporal sequence is uniquely defined by the underlying motion (equation (3.27)) [123]. By estimating such displacements, one can describe the object's motion through the studied sequence. Let $I(x_1, x_2, t)$ denote the pixel intensity at location $\boldsymbol{x} = [x_1, x_2]$ and time t for a given slice temporal sequence. The optical flow assumption can be expressed as:

$$I(x_1 + dx_1, x_2 + dx_2, t + dt) = I(x, y) \tag{3.27}$$

Based on the least square solution of the optical flow equation presented by Lucas and Kanade [127], the 2D affine motion for each slice can be estimated by minimizing the following energy:

$$E_{OFT} = \int_{\mathbb{R}^2} \mathcal{W}(x_1 - c_1, x_2 - c_2)\left(I_{x_1}u + I_{x_2}v + I_t\right)^2 d\boldsymbol{x} \tag{3.28}$$

where

$$u(x_1, x_2) = u_o + u_{x_1}(x_1 - c_1) + u_{x_2}(x_2 - c_2) \tag{3.29}$$

$$v(x_1, x_2) = v_o + v_{x_1}(x_1 - c_1) + v_{x_2}(x_2 - c_2) \tag{3.30}$$

encode the motion field to be estimated along x_1 and x_2, respectively. $\nabla I = [I_{x_1}, I_{x_2}]$ is the local image spatial gradient, whereas I_t corresponds to the temporal derivative. As in [123], in order to reduce the effect of noise in the assessment of the spatial gradient, $\nabla I(x)$ was computed using gaussian derivative kernels along x_1 and x_2, with $\sigma = 1$. I_t was simply estimated with finite forward differences. $\mathcal{W}$ is a local windows function centered in the position $\boldsymbol{c} = [c_1, c_2]$ and, according to the anatomical constraint introduced in [123], is given by:

$$\mathcal{W}(x) = \sum_{x_k \in \mathcal{C}} \mathcal{N}(x_k) \tag{3.31}$$

where $\mathcal{N}(\boldsymbol{x})$ is a neighborhood function defined as a 2D square center in $\boldsymbol{x}$ and $x_k \in \mathcal{C}$ stands for the sampled points in the LV contour being tracked. $\mathcal{N}$ was defined as a 7×7 square centered in the target point. Such region is smaller than the one in US data [123] due to the larger pixel spacing in CMR images and reduced uncertainty associated with this data. To further decrease the method's computational burden, we propose to subsample the contours by a factor of 4, reducing the required local motion estimations. Such subsampling is possible because superposition of local regions can be avoided without losing robustness for the global motion estimation [Figure 3.14].

By differentiating equation (3.28) with respect to the affine motion field components [123], the minimization of the weighted least-square criterion can be expressed as the solution of:

$$\boldsymbol{A}^T \mathcal{W} \boldsymbol{A} \boldsymbol{d} = \boldsymbol{A}^T \mathcal{W} \boldsymbol{b} \tag{3.32}$$

where $\boldsymbol{d}$ encodes the elements of the affine motion, $\boldsymbol{A}^T \mathcal{W} \boldsymbol{A}$ is the spatial gradient vector and $\boldsymbol{A}^T \mathcal{W} \boldsymbol{b}$ is the image mismatch vector**.** These components are expressed as:

$$\boldsymbol{A} = [I_{x_1} \quad I_{x_2} \quad x_1 I_{x_1} \quad x_2 I_{x_1} \quad x_1 I_{x_2} \quad x_2 I_{x_2}]^T \tag{3.33}$$

$$\boldsymbol{A}^T \mathcal{W} \boldsymbol{b} = -\begin{bmatrix} \langle \mathcal{W}, I_{x_1} I_t \rangle \\ \langle \mathcal{W}, I_{x_2} I_t \rangle \\ \langle \mathcal{W}, x_1 I_{x_1} I_t \rangle \\ \langle \mathcal{W}, x_1 I_{x_2} I_t \rangle \\ \langle \mathcal{W}, x_2 I_{x_1} I_t \rangle \\ \langle \mathcal{W}, x_2 I_{x_2} I_t \rangle \end{bmatrix} \tag{3.34}$$

$$\boldsymbol{d} = [u_o \quad v_0 \quad u_{x_1} \quad u_{x_2} \quad v_{x_1} \quad v_{x_2}]^T \tag{3.35}$$

Further, and as stated above, the estimation is performed iteratively for each pair of frames, allowing the accumulation of displacement fields and capturing larger ventricle's movements [123, 126]. Such refinement scheme helps overcome the small displacements assumption made by Lucas and Kanade equation [127]. In order to keep the computational

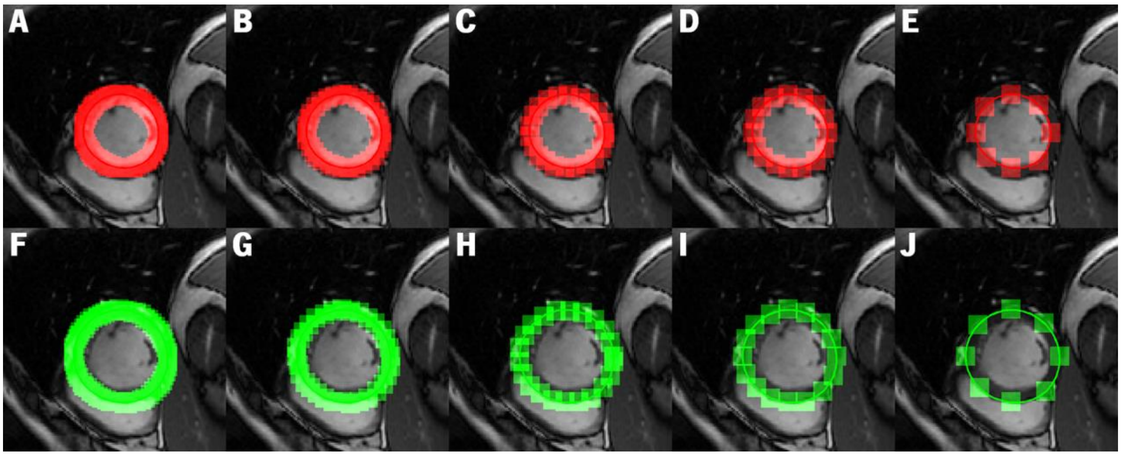

Figure 3.14 - Effect of contours' subsampling in analyzed region of interest for motion estimation. The solid line represents the contour being tracked, while the overlay squares represent the anatomical regions of interest used to estimate the motion. A subsampling factor of 1, 2, 3, 4 and 8 was applied in **(A)** to **(E)** endocardial and **(F)** to **(J)** epicardial contour. The higher the factor, the less overlapping region exists, until no overlap occurs ((E) and (J)). One should avoid subsampling further than a factor of 4 to avoid losing robustness by incomplete region of interest. Nevertheless, until a factor of 4, a lower number of points lead to a reduced number of local motion estimations to be performed, therefore decreasing the computational burden of the method.

burden of the method low, we chose to perform 4 iterations and then exit the algorithm, which already provides a good balance between motion accuracy and overall computational time.

Finally, the propagation is applied sequentially between adjacent phases using the previous LV contours, until every cardiac phase has been delineated. Note that to minimize error accumulation, we ensure a minimal number of propagation steps by propagating the contours in both directions for half the total number of cardiac phases.

3.7 Implementation Details

3.7.1 BEAS Contours' Evolution

In active contours frameworks, gradient descent minimization is the most frequently used optimization scheme to minimize the energy functional for segmentation [63, 74-76]. To this end, a modified version of gradient descent with feedback step adjustment algorithm is used, as proposed in the original BEAS framework [47]. According to this algorithm, the B-spline coefficients will evolve as:

$$c[\boldsymbol{k}]^{(t+1)} = c[\boldsymbol{k}]^{(t)} + \lambda \frac{\partial E}{\partial c[\boldsymbol{k}]^{(t)}} \tag{3.36}$$

At each step, the B-spline coefficients are updated and the corresponding energy is calculated. If the given step leads to a decrease in the global energy, the update is considered successful and the B-spline coefficients of the current iteration, $c[\boldsymbol{k}]^{(t+1)}$, are kept to the next one, while the step size λ is set to 1. If not, $c[\boldsymbol{k}]^{(t+1)}$ are still kept, but the step size of the next iteration is divided by $\eta_f \geq 1$, yielding a more conservative step. If a new energy minimum is not found in a few iterations, the algorithm exits and the last energy minimum, and corresponding contours, are chosen as result. By not exiting the algorithm in the first detected minimum, the algorithm is still able to escape small local minima and better converge to the optimal solution [47]. Obviously, the number of iterations that the algorithm is allowed to continue without finding a new energy minimum should be properly defined to allow escaping local minima, but at the same time without being too big, as the computational time increases with an increased number of iterations. In the presented results, this value was set to 10.

3.7.2 Segmentation parameters

Concerning BEAS-related parameters in the 2D segmentation, h was set to 2^2 and 2^3 for the wall position and thickness respectively, while for the 3D initialization and segmentation a value of 2^3 and 2^4 was used. The increased spacing allows a higher degree of smoothness of the surface's shape and thickness, overcoming possible errors due to the presence of TPMs or in cases of low contrast and reduced spatial information (e.g., in apical slices). Regarding the smoothing across slices, a value of 2^0 was set, which avoids over-smoothing in the third dimension, as specified in Section 3.5.1. Similar to [118], 64 points were used on each boundary for the contour discrete representation. Such value is large enough to capture the level of shape detail required for myocardial segmentation, while also dense enough to extract reliable information taking into account the complexity and heterogeneity of the image properties, as recommended in [47]. Furthermore, a local region of size 15×15 and 11×11 was used to assess local region statistics for the endo and epicardial contours, respectively. The local region is smaller for the epicardium because of the unpredictability of the outer region, which may introduce errors in the local mean estimations. The proposed region weights, w_i, were set to 0.3 for the in and out regions. As stated in Section 3.3.2, values lower than one push the contours towards the myocardial region, surpassing the presence of TPMs. The chosen values allow a good compromise for contour delineation and without leakage into the myocardial region. At last, the parameter α in the hybrid epicardial energy functional was empirically set to 0.05, in order to equally balance the two terms. For further general considerations and implementation details about BEAS, the reader is referred to the work of Barbosa *et al.* [47].

Since it is possible that both contours are attracted towards the same image feature leading to their merging, we included a thickness constraint in the evolution. This prevents the contours' merging by locally penalizing the two interfaces to have a minimum thickness of 1px between them. Let us note that in [63], Chen *et al.* also introduced a thickness constraint in the energy, but they considered it as a global term (a deviation from the average thickness), modeled as two distinct level-sets and not considering its local variation.

Moreover, a curvature-based shape prior is also included in the energy functional to avoid concave shapes. This was simply implemented as a soft inflating balloon force in regions where the contour had negative curvature. The purpose of such prior is to also ensure the correct segmentation of TPMs. To this end, the curvature (k) in each point of the model surface is analyzed according to the following equation (for polar coordinates):

$$k = \frac{r^2 + 2r_\theta^2 - r.r_{\theta\theta}}{(r^2 + r_\theta^2)^{3/2}} \tag{3.37}$$

where r_θ and $r_{\theta\theta}$ represent the first and second order derivatives of r in order of θ.

Regarding BEASPM, in what concerns BEAS-related parameters, we set h to 2^3 and 2^4 for the wall position and thickness, respectively, and 2^0 along the third dimension. Moreover, the profile's size in the reference frame is 15px, while the size of the search profile in the target frame is 41px, allowing enough freedom for contraction/expansion during the cardiac cycle but avoiding using the full radial profile to lower the computational burden. The resolution of profiles' sampling was set to 0.25px (using nearest-neighbor interpolation method) to ensure a good tradeoff between sharp definition and computational burden. v_i was empirically set to 25 and 50 for the endo and epicardial energy functionals, respectively, in order to balance both energy components and give higher importance to the similarity measure (SAD).

4. Results

4. Results

4.1 Data

To assess the performance of the proposed framework, we used the cine steady state free precession (SSFP) MR SAX datasets available for the MICCAI 2009 Cardiac MR Left Ventricle Segmentation Challenge [128]. The database includes 45 cardiac MRI datasets obtained with a 1.5T GE Signa MRI, during 10- to 15-s breath holds with a temporal resolution of 20 phases over the cardiac cycle. Per patient, six to twelve images were obtained from the atrioventricular ring to the apex (thickness = 8mm, FOV = 320mm×320mm, matrix = 256×256), with an isotropic pixel spacing ranging from 1.29 to 1.56mm. The database contains 32 males (mean age, 59 ± 15.2 years; range, 23 – 83 years) and 13 females (mean age, 67 ± 12.8 years; range, 46 – 88 years). The data includes 12 patients with heart failure and myocardial infarction (HF-I), 12 with heart failure without myocardial infarction (HF-NI), 12 with hypertrophic cardiomyopathy (HYP) and 9 normal cases (N). Moreover, it provides a ground truth, drawn by an experienced cardiologist, in all slices for endocardium and epicardium at the ED phase and for endocardium at the ES phase. All reported results consider manual contours drawn to include TPMs in the LV cavity. The present database was chosen as it enables a direct comparison against other state-of-the-art methods which have reported their segmentation performance in this same database.

4.2 Evaluation Metrics

In order to evaluate the accuracy and robustness of the proposed framework, each module of the methodology was tested and validated in the following sections.

The evaluation code provided in [128] is used to assess the segmentation performance against reference manual contours, evaluating the Dice metric, the average perpendicular distance (APD) and the percentage of “good contours” (contours for which the APD is less than 5mm). In order to understand the maximum local error of the framework, we also compute the Hausdorff distance, which is defined as the maximum perpendicular distance between contours. The APD measures the perpendicular distance from the automatically segmented contour to the corresponding manual contour, averaged over all contour points [Figure 4.1A and C]. A lower value indicates a better match and increased proximity between contours. The Dice metric [42], in its turn, measures the similarity between manual and automatic segmentation by measuring their area overlap [Figure 4.1B and D]. Its value ranges from 0 to 1, with higher values implying

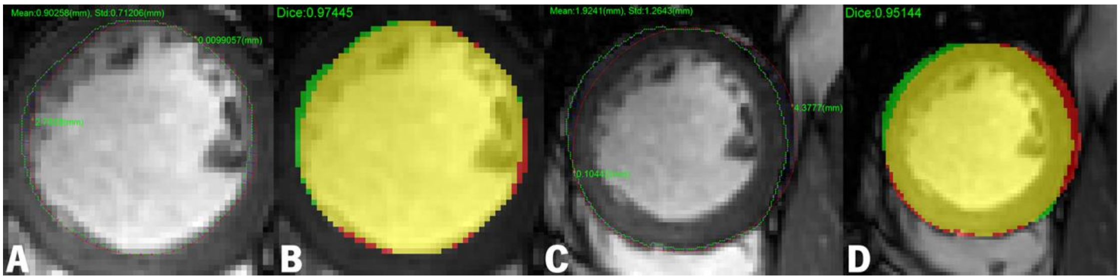
Mean:0.90258(mm), Std:0.71206(mm)
0.0099057(mm)
Dice:0.97445
Mean:1.9241(mm), Std:1.2643(mm)
4.3777(mm)
Dice:0.95144
A
B
C
D

Figure 4.1 - Evaluation metrics used for segmentation performance assessment.
Average perpendicular distance (APD) measured between automatic and manual contours for **(A)** endocardium and **(C)** epicardium. The Hausdorff distance (maximum perpendicular distance) is also reported for local maximum error evaluation. Dice metric measured for **(B)** endocardial and **(D)** epicardium (green area: reference manual contour; red area: automatically segmented contour; yellow: intersection between them).

better match between automatic and manual segmentations. In practice, it is computed using the following expression:

$$Dice = \frac{2A_{am}}{A_a + A_m} \tag{4.1}$$

where A_a, A_m and A_{am} represent, respectively, the areas of the automatically segmented contour, the reference manual contour and the intersection between them.

Each measure was computed slice by slice and a mean value for all slices of a dataset was calculated. However, the original evaluation code only considers "good contours" when computing these means (excluding the remaining slices). Besides this limitation, it also removes the slices only present in one of the cardiac phases (ED or ES), disregarding longitudinal contraction. Taking into account the interest in future comparisons with methods that also use this database, the results obtained with the original code are reported. Nevertheless, to overcome both limitations and fully understand the framework performance, the segmentation metrics were also computed considering all available contours in a customized evaluation code.

Moreover, to assess the clinical added value of the proposed 3D+time automatic segmentation, we compute several cardiac indices used in daily clinical practice to assess both global LV morphology and function. In this sense, the end-diastolic volume, end-systolic volume, stroke volume, left ventricular mass and ejection fraction were estimated for each CMR dataset. Linear regression and Bland-Altman analysis [129] were performed to assess the correlation between reference clinical indices and the automatically computed ones. Again, the evaluation code presents the aforementioned limitations preventing the correct evaluation. To allow future comparisons, such results are still reported for both LVM and EF, as stated in [128]. Nonetheless, the customized code is also used to report clinically correct values using all contours initially consider by the expert during manual segmentation.

At last, the average computational time for each step of the proposed approach was also measured, along with the average total computational time to segment a dataset. The reported CPU times were obtained using MATLAB code running on a 2.4 GHz dual-core laptop.

4.3 Automatic Mid-ventricular Initialization

We developed a novel automatic initialization procedure for LV detection and initialization in mid-ventricular SAX cuts, based on a multilevel Otsu thresholding and an elliptical annular template matching. In order to evaluate its performance, both modules, LV localization and template matching, were tested against their original counterparts.

The feasibility of the proposed LV localization approach was tested against the method in [67] by considering a correct location when the identified object's centroid was less than 5px away from the reference LV center. The proposed automatic LV localization method was able to retrieve the correct LV centroid in all 45 mid-ventricular slices. In contrast, the method in [67] was only able to locate the LV in 36 cases. In Figure 4.2, two example SAX images are presented and their corresponding conventional and multilevel Otsu thresholding applied over the defined ROI. Note that the results for the method in [67] were obtained using the parameters defined by the authors (a ROI with 110px and an objects' area threshold of 40px).

In its turn, the proposed automatic initialization algorithm, using an elliptical annular

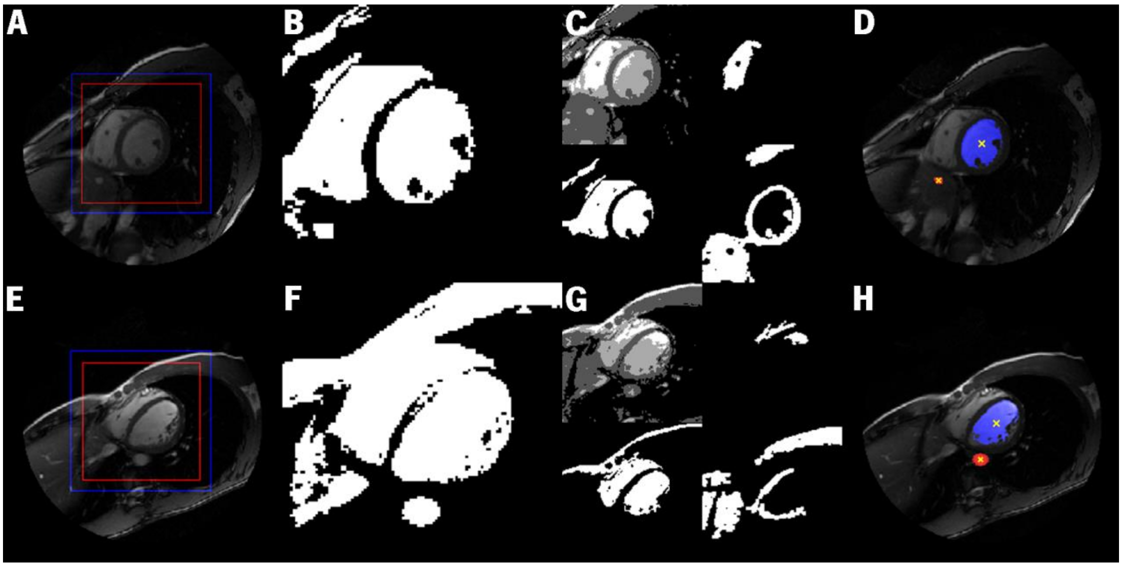

Figure 4.2 - Comparison between proposed LV localization procedure and method in [67] for datasets N-7 and HF-NI-15.
(A) and **(E)** Original image and used ROI; **(B)** and **(F)** conventional Otsu thresholding [67]; **(C)** and **(G)** multilevel Otsu thresholding and class decomposition for LV object search (from left to right and top to bottom: multilevel Otsu thresholding, brightest class, two brightest classes combined, third brightest class); **(D)** and **(H)** LV object and its centroid (red: Lu *et al.* method [67]; blue: proposed method).

template matching procedure, was compared quantitatively against the original circular template matching in [110] by considering a poor initialization when the Hausdorff distance to the reference contours was over 10px for the endo and/or epicardium. The Hausdorff distance was chosen for evaluation metric in this case, as during the subsequent segmentation the region-based energy only computes its statistics in a local window of size 15×15 and 11×11 for endo and epicardium, respectively. Therefore, a maximum perpendicular distance over 10px would correspond to a region outside the convergence basin of the algorithm. This can be easily understood by considering that the local windows where the statistical parameters are estimated act as the line of sight of the contour evolution process. Thus, if the maximum perpendicular distance is too high, it prevents the correct segmentation of the interface, since the contour is not able to "see" the correct boundary position.

Figure 4.3 shows two examples of the performance of the proposed elliptical annular template matching algorithm for one circular and one elliptical shaped left ventricle. The proposed approach return an appropriate initialization (i.e., Hausdorff distance lower than 10px) in 41 out of 45 cases, thus yielding a feasibility 91.1%, against a feasibility of 71.1% (32/45) for the original method [110]. The 4 wrongly initialized images [Figure 4.4] will be discarded for the subsequent 2D segmentation analysis, but later included in the 3D and 3D+time analysis as it was found that the proposed stack initialization is able to recover from these incorrect or sub-optimal initializations.

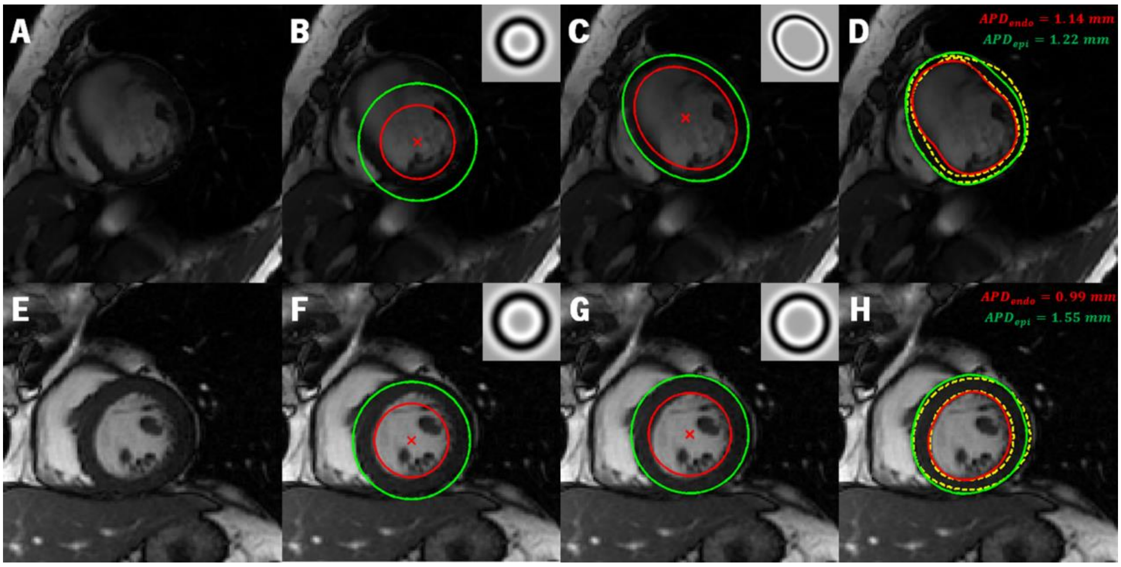

Figure 4.3 - Automatic template matching initialization and segmentation result for the proposed energy in two mid-ventricular SAX images (from datasets HF-NI-13 and HYP-3).
(A) and **(E)** Original image ROI; **(B)** and **(F)** circular template matching in [110] and optimal kernel; **(C)** and **(G)** proposed elliptical annular template matching algorithm and optimal kernel; **(D)** and **(H)** segmentation result for endo and epicardial contours (red: endocardium; green: epicardium; yellow: ground truth).

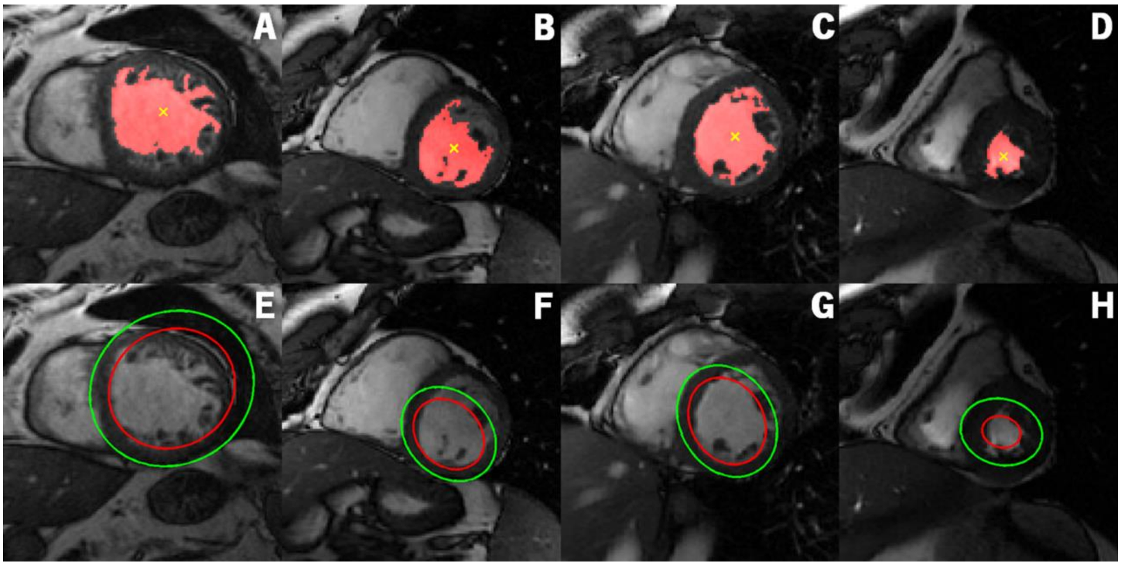

Figure 4.4 - LV localization and elliptical template matching limitations.
(A) - (D) LV cavity object detected using the proposed LV localization algorithm; **(E) - (H)** Corresponding initial contours obtained using the proposed elliptical annular template matching algorithm. The presented mid-ventricular slices are from the following datasets: **(A)** and **(E)** HF-NI-4; **(B)** and **(F)** HF-NI-31; **(C)** and **(G)** HF-NI-33; **(D)** and **(H)** HF-HYP-40.

4.4 Coupled Myocardial 2D Segmentation

After obtaining two initial contours from the proposed initialization algorithm, the coupled myocardial segmentation is applied to find the true contours in the mid-ventricular slice. At this point, we pretend to evaluate the proposed 2D energy functional, designed specifically for CMR images, using the localized Chan-Vese energy in [98] as benchmark. In order to understand the influence of an automatic initialization, we performed this comparison with both automatic and manual initializations. In the latter case, both contours were manually initialized as two concentric ellipses fitted to 6 input points introduced by a non-expert user. One should note that the chosen benchmark was applied using the proposed coupled formulation and with the same BEAS-related parameters (spacing, local regions size, etc.). Thus, the evaluated differences will regard the weighted formulation and the specific energy for each contour (SLY and LCV for endo and epicardium, respectively).

The performance of the proposed 2D segmentation approach against the chosen benchmark in the 41 mid-ventricular SAX images is shown in Table 4.1. Two segmentation examples using the presented modified energy functionals are presented in Figure 4.3D and H. Moreover, Figure 4.5 presents 4 mid-ventricular slices segmented using the CMR-targeted energy and chosen benchmark, so as to visually depict the major conceptual differences between them. In Figure 4.6 and Figure 4.7, several segmentation examples are presented to evaluate the robustness against initialization, illustrating the initial contours used (automatically or manually obtained) and the final contours obtained after contours' evolution.

In Appendix A, a combined local and global region-based formulation for the myocardial region taking advantage of its homogeneity in mid-ventricular slices is presented. Moreover, the influence of each added feature in the energy functional is also studied, ultimately giving insights about the importance of a CMR-targeted energy. Later, when also considering basal and apical slices, partial volume effects and intensity inhomogeneities (due to the MRI bias field) prevent the introduction of the myocardial homogeneity assumption in the 3D segmentation. Therefore, and for consistency, we chose not to include it also in the 2D segmentation (thus only presented in Appendix A).

Table 4.1 - 2D Segmentation performance for endo and epicardium (# = 41, $\mu \pm \sigma$).

	Initialization	**Energy**	**Dice**		**APD** (mm)		**Hausdorff** (mm)	
			Endo	**Epi**	**Endo**	**Epi**	**Endo**	**Epi**
A	Manual	[98]	0.93 ± 0.04	0.93 ± 0.02	1.98 ± 0.90	2.51 ± 1.01	4.51 ± 1.80	5.60 ± 1.60
B	Manual	Proposed	0.95 ± 0.03	0.96 ± 0.02	1.31 ± 0.58	1.56 ± 0.58	3.58 ± 1.70	4.18 ± 1.46
C	Automatic	[98]	0.90 ± 0.08	0.92 ± 0.04	2.65 ± 1.73	2.87 ± 1.21	6.30 ± 3.53	6.82 ± 2.93
D	Automatic	Proposed	0.93 ± 0.05†*	0.94 ± 0.03†*	1.91 ± 1.36†*	2.21 ± 0.95†*	5.19 ± 3.56†*	5.81 ± 2.93†*

No significant difference was found against A.
† $p < 0.05$, paired t-test against B.
* $p < 0.05$, paired t-test against C.

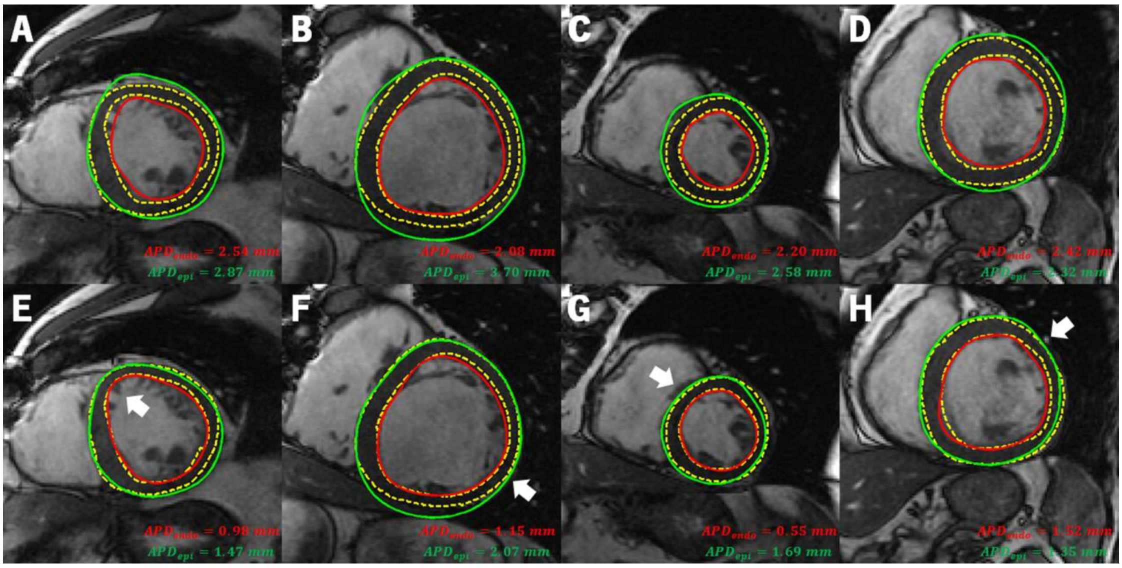
A
$APD_{endo} = 2.54\ mm$
$APD_{epi} = 2.87\ mm$
B
$APD_{endo} = 2.08\ mm$
$APD_{epi} = 3.70\ mm$
C
$APD_{endo} = 2.20\ mm$
$APD_{epi} = 2.58\ mm$
D
$APD_{endo} = 2.42\ mm$
$APD_{epi} = 2.32\ mm$
E
$APD_{endo} = 0.98\ mm$
$APD_{epi} = 1.47\ mm$
F
$APD_{endo} = 1.15\ mm$
$APD_{epi} = 2.07\ mm$
G
$APD_{endo} = 0.55\ mm$
$APD_{epi} = 1.69\ mm$
H
$APD_{endo} = 1.52\ mm$
$APD_{epi} = 1.35\ mm$

Figure 4.5 - 2D segmentation results for (A)-(D) the chosen benchmark energy from [98] and (E)-(F) the proposed modified energy functional in 4 example mid-ventricular SAX images.
The presented mid-ventricular slices are from the following datasets: **(A)** and **(E)** HF-I-7; **(B)** and **(F)** HF-I-9; **(C)** and **(G)** HF-I-40; **(D)** and **(H)** HF-NI-3 (red: endocardium; green: epicardium; yellow: ground truth). The white arrows highlight interesting regions of improvements with the added energy features.

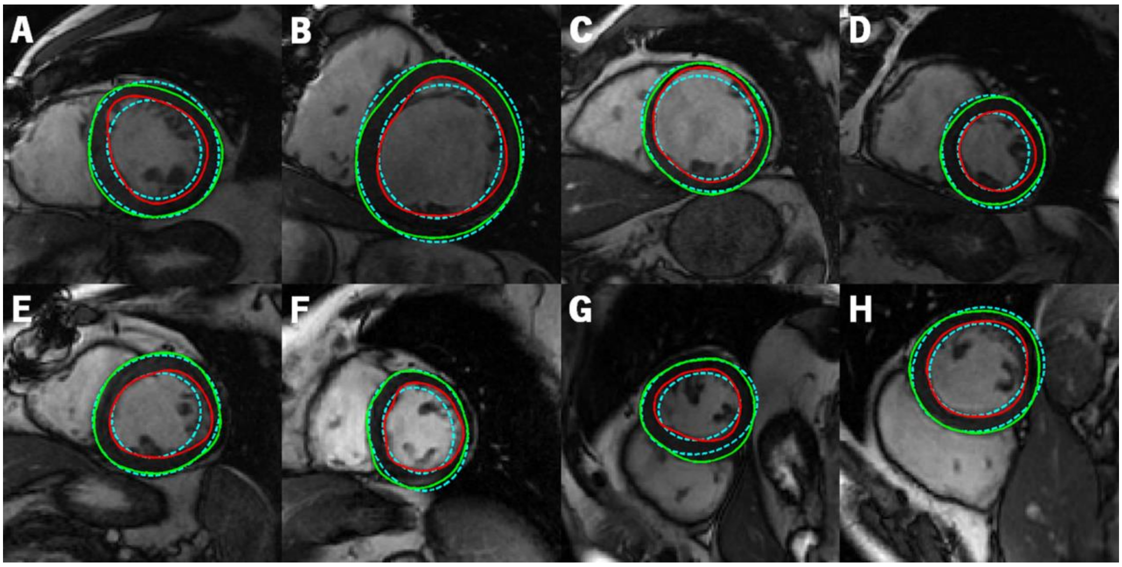

Figure 4.6 - Segmentation results for 8 mid-ventricular SAX images, after automatic initialization. The presented mid-ventricular slices are from the following datasets: **(A)** HF-I-7; **(B)** HF-I-9; **(C)** HF-I-11; **(D)** HF-I-40; **(E)** HF-NI-7; **(D)** HYP-1; **(D)** HYP-37; **(D)** N-9 (red: endocardium; green: epicardium; cyan: initial contours).

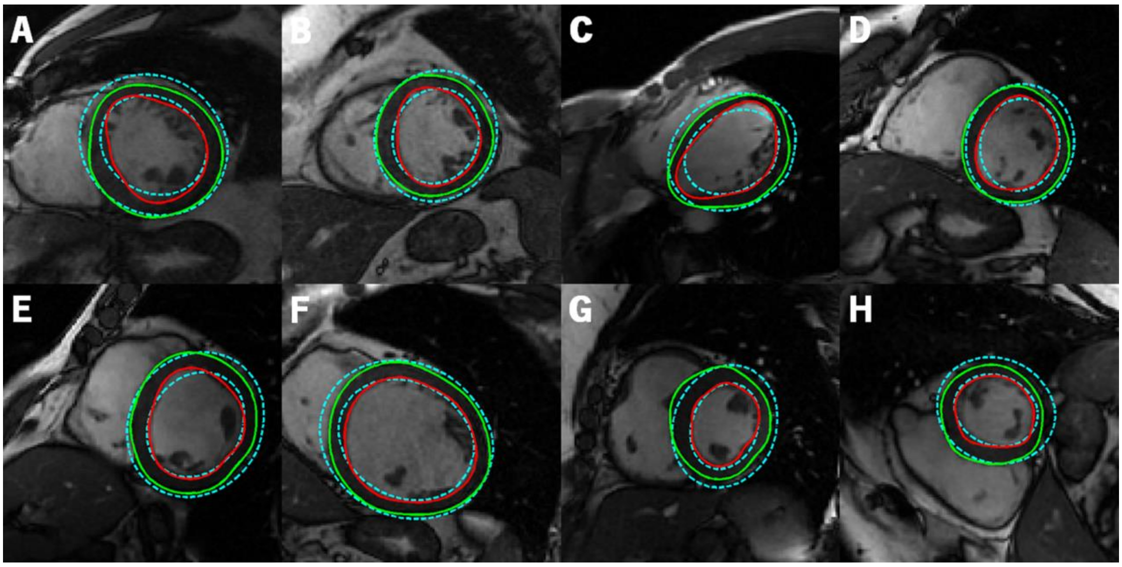

Figure 4.7 - Segmentation results for 8 mid-ventricular SAX images, after manual initialization. The presented mid-ventricular slices are from the following datasets: **(A)** HF-I-7; **(B)** HF-I-12; **(C)** HF-NI-15; **(D)** HF-NI-31; **(E)** HF-NI-34; **(D)** HF-NI-36; **(D)** HYP-6; **(D)** N-6 (red: endocardium; green: epicardium; cyan: initial contours).

4.5 Coupled Myocardial 3D Segmentation

Table 4.2 summarizes the performance for the 3D segmentation, computed using both original evaluation code (OC) and customized code (CC). Again, both automatic and manual initializations were considered for comparison. Note that the manual initialization is only applied in the mid-ventricular slice (as in the 2D segmentation results) and the proposed automatic stack initialization is afterward used. As stated in Section 4.3, all 45 datasets are included in the performance evaluation.

Table 4.2 - 3D segmentation performance for endo and epicardium (# = 45, $\mu \pm \sigma$).

Initialization		**Dice**		**APD** (mm)		**Hausdorff** (mm)		**Good Contours** (%)	
		Endo	**Epi**	**Endo**	**Epi**	**Endo**	**Epi**	**Endo**	**Epi**
OC	Manual	0.94 ± 0.03	0.94 ± 0.03	1.46 ± 0.48	1.77 ± 0.36	3.80 ± 1.03	4.58 ± 0.91	98.2 ± 5.4	97.6 ± 6.4
	Automatic	0.93 ± 0.03	0.94 ± 0.02	1.50 ± 0.47	1.80 ± 0.41	3.97 ± 1.24	4.65 ± 1.14	97.4 ± 8.2	95,4 ± 9.6
CC	Manual	0.92 ± 0.04	0.93 ± 0.03	1.56 ± 0.60	1.89 ± 0.53	4.02 ± 1.34	4.80 ± 1.19	98.2 ± 5.4	97.6 ± 6.4
	Automatic	0.92 ± 0.04	0.93 ± 0.03	1.70 ± 0.89	2.06 ± 0.84†	4.34 ± 1.91	5.14 ± 1.79	97.4 ± 8.2	95,4 ± 9.6

† $p < 0.05$, paired t-test against manually initialized results (for corresponding evaluation code).

Original code (OC) only considers “good contours”, while the customized code (CC) uses all segmented slices.

To also assess the overall performance distribution rather than only average results, Figure 4.8 presents the boxplots for each metric for both endo and epicardial contours using the customized code. Moreover, the spatial error distribution from basal to apical slices of both APD and Hausdorff distance metrics are illustrated in Figure 4.9. Note that the Dice metric distribution is not presented as it is influenced by the relative size of the object (which is smaller in apical slices) and thus not suitable for comparison between slices (i.e., smaller areas have an implicitly smaller Dice for the same APD). The distribution was obtained by normalizing the slices z level into the range 0 to 1 and dividing the resultant errors dispersion into 5 equal classes.

At last, Figure 4.10 gives three segmentation examples with several slices from base to apex, with their respective 3D surfaces illustrated in Figure 4.11. In the latter image, the inter-slice data was interpolated for better visualization. In addition, the estimated misalignment was correct prior 3D visualization, thus yielding a spatially smoothed surface.

Further, in Appendix B, the influence of the edge-based term in the epicardial energy functional, and the importance of its combination with a region-based term, is inspected. Moreover, in Appendix C, the choice of the parameters that influence the 3D segmentation performance (as described in Section 3.7) is addressed and the influence of their variation is investigated.

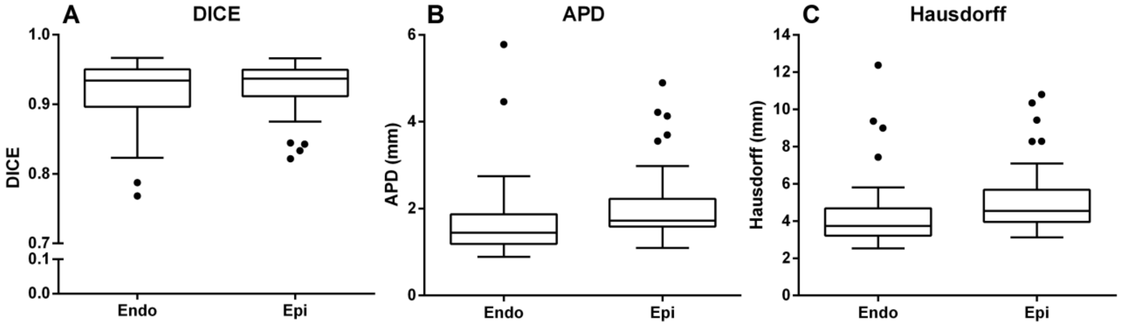

Figure 4.8 - Boxplots of computed (A) Dice metric, (B) APD and (C) Hausdorff distance for both endo and epicardial contours using the proposed automatic 3D segmentation (# = 45).

The ends of whiskers represent the lowest and highest datum still within 1.5 times the inter-quartile range of the lower and upper quartile, respectively. Any data value larger is considered an outlier and plotted as a dot. The plotted results were computed using the customized code, where all slices are included.

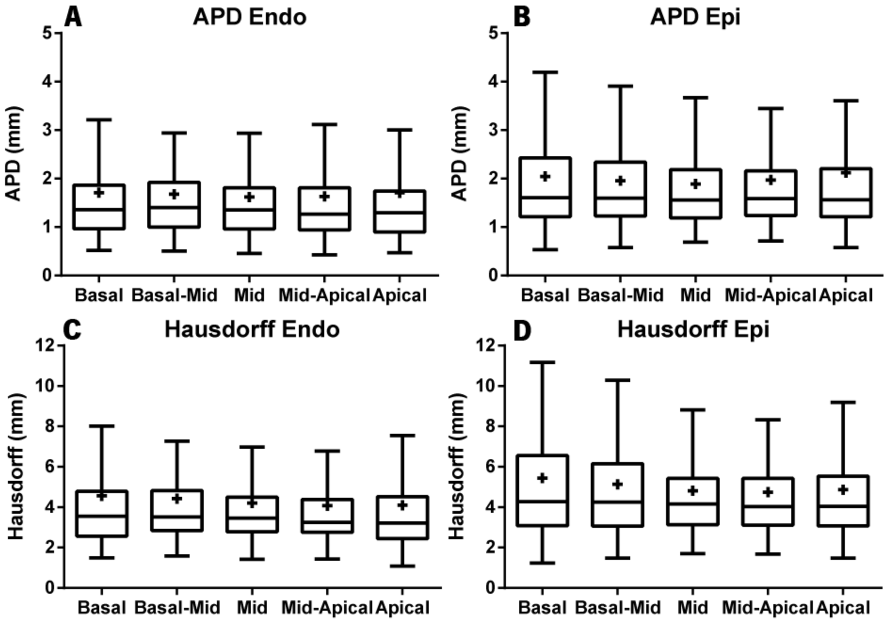

Figure 4.9 - Boxplots for APD and Hausdorff metrics distribution from basal to apical slices using the proposed automatic 3D segmentation (# = 45).
(A) APD for endocardial contour; **(B)** APD for epicardial contour; **(C)** Hausdorff distance for endocardial contour; **(D)** Hausdorff distance for epicardial contour. The ends of the whiskers represent the lowest and higher datum still within 1.5 times the inter-quartile range of the lower and upper quartile, respectively. The crosses represent the mean values for each metric. The results were computed using the customized code, where all slices are included.

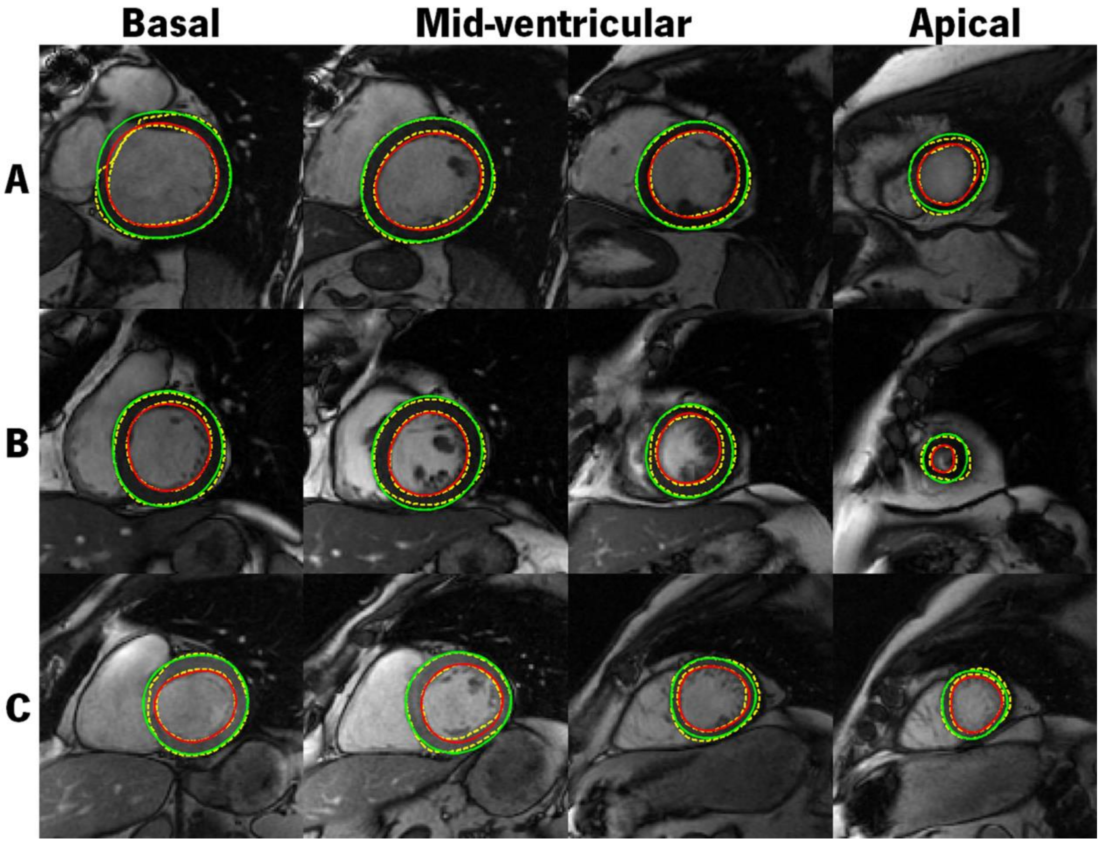

Figure 4.10 - Automatic 3D segmentation results for three example CMR datasets.
The presented slices are from the following datasets: **(A)** HF-I-5, **(B)** HYP-3 and **(C)** N-2 (red: endocardium; green: epicardium; yellow: ground truth).

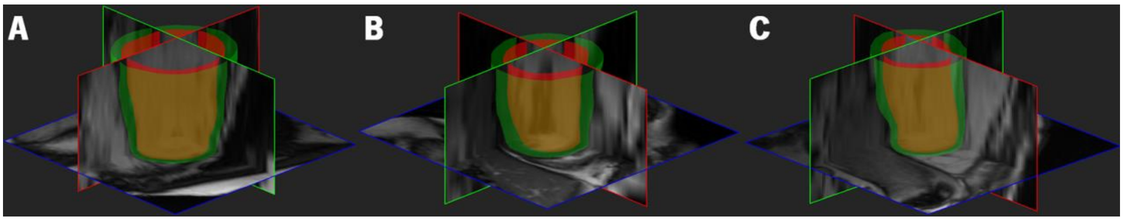

Figure 4.11 - 3D LV surface from the three datasets presented in Figure 4.10.
The presented surfaces are from the following datasets **(A)** HF-I-5, **(B)** HYP-3 and **(C)** N-2.

4.6 3D+time Tracking

To propagate both endocardial and epicardial contours over all cardiac phases, two tracking methodologies were presented, namely BEAS profile matching (BEASPM) and global anatomical affine optical flow (OFT). We proposed to compare these two opposed methodologies in order to evaluate the possible differences between a local and a global tracking algorithm. Again, the tracking performance at this stage will be assessed. To this end, besides the endo and epicardial manual contours at the ED phase, the endocardial manual contours in ES phase were also considered. Note that the MICCAI challenge database does not provide the epicardial reference contour in ES phase. Moreover, one should note that to allow direct comparison between the expert contours and ours, the ES phase and its corresponding basal and apical slices are chosen based on the manual contours. While the ES phase could be automatically determined using the LV cavity's volume (smaller one), the basal and apical slices couldn't be defined without long-axis views (which are not provided in the used database).

Regarding this 3D+time myocardial segmentation, Table 4.3 and Table 4.4 present the overall segmentation plus tracking performance (computed using our customized code) for the local and global tracking methods, respectively, for all 45 datasets and also categorized by pathology. Based on the similarity between automatic and manual initializations in the 3D segmentation results [Table 4.2], we chose not to include this comparison in the 3D+time case. Figure 4.12 gives an example tracking result over the cardiac cycle for both methods. The corresponding 3D LV surface evolution from ED phase to ES phase for the same dataset is illustrated in Figure 4.13, computed using the global optical flow method. Moreover, a complete 3D LV surface evolution, illustrating the full cardiac cycle, is presented in Figure 4.14.

The comparison of the proposed approach against state-of-the-art methods that used the same database [43-45, 66, 78, 130-133] is presented in Table 4.5, with both tracking methodologies reported and using the original evaluation code for metrics computation. Moreover, the average total computational time to segment a dataset using either methodology is also presented. One should note that other authors also reported their results using the MICCAI database [46, 134-136], but their performance was inferior to the ones here included.

Table 4.3 - 3D+time segmentation performance for endo and epicardial contours using BEAS profile matching, categorized by pathology and average result (# = number of datasets, $\mu \pm \sigma$).

	#	**Dice**		**APD** (mm)		**Hausdorff** (mm)		**Good Contours** (%)	
		Endo	**Epi**	**Endo**	**Epi**	**Endo**	**Epi**	**Endo**	**Epi**
HF-I	12	$0.92 \pm 0.05^{*\dagger}$	0.94 ± 0.03	1.88 ± 1.18	1.93 ± 0.96	4.48 ± 2.28	5.09 ± 1.91	95.3 ± 10.6	95.1 ± 12.6
HF-NI	12	$0.91 \pm 0.03^{\ddagger\S}$	0.92 ± 0.04	2.00 ± 0.55	2.17 ± 0.86	5.22 ± 1.82	5.37 ± 2.09	96.4 ± 4.7	93.8 ± 9.4
HYP	12	$0.85 \pm 0.05^{*\ddagger}$	0.91 ± 0.03	2.09 ± 0.42	2.14 ± 0.63	4.61 ± 0.88	5.18 ± 1.36	96.8 ± 5.1	98.3 ± 3.7
N	9	$0.86 \pm 0.04^{\dagger\S}$	0.92 ± 0.03	2.15 ± 0.73	2.01 ± 0.83	5.07 ± 1.53	4.87 ± 1.65	94.9 ± 8.9	94.0 ± 9.9
Total	45	0.89 ± 0.05	0.93 ± 0.03	2.02 ± 0.78	2.06 ± 0.84	4.83 ± 1.75	5.14 ± 1.79	95.9 ± 7.7	95.4 ± 9.6

[*] $p < 0.05$, unpaired t-test between HF-I and HYP; [†] $p < 0.05$, unpaired t-test between HF-I and N; [‡] $p < 0.05$, unpaired t-test between HF-NI and HYP; [§] $p < 0.05$, unpaired t-test between HF-NI and N.

Metrics computed using the customized code, which considers all available contours.

Table 4.4 - 3D+time segmentation performance for endo and epicardial contours using global optical flow tracking, categorized by pathology and average results (# = number of datasets, $\mu \pm \sigma$).

	#	**Dice**		**APD** (mm)		**Hausdorff** (mm)		**Good Contours** (%)	
		Endo	**Epi**	**Endo**	**Epi**	**Endo**	**Epi**	**Endo**	**Epi**
HF-I	12	$0.92 \pm 0.05^{*\dagger}$	0.94 ± 0.03	1.93 ± 1.28	1.93 ± 0.96	4.66 ± 2.38	5.09 ± 1.91	93.3 ± 12.0	95.1 ± 12.6
HF-NI	12	$0.91 \pm 0.03^{\ddagger\S}$	0.92 ± 0.04	2.01 ± 0.57	2.17 ± 0.86	5.42 ± 2.01	5.37 ± 2.09	94.2 ± 3.6	93.8 ± 9.4
HYP	12	$0.81 \pm 0.06^{*\ddagger}$	0.91 ± 0.03	2.40 ± 0.61	2.14 ± 0.63	4.95 ± 0.93	5.18 ± 1.36	90.1 ± 9.6	98.3 ± 3.7
N	9	$0.85 \pm 0.05^{\dagger\S}$	0.92 ± 0.03	2.25 ± 0.79	2.01 ± 0.83	5.22 ± 1.58	4.87 ± 1.65	93.2 ± 8.6	94.0 ± 9.9
Total	45	0.87 ± 0.07	0.93 ± 0.03	2.14 ± 0.88	2.06 ± 0.84	5.05 ± 1.79	5.14 ± 1.79	92.7 ± 9.5	95.4 ± 9.6

[*] $p < 0.05$, unpaired t-test between HF-I and HYP; [†] $p < 0.05$, unpaired t-test between HF-I and N; [‡] $p < 0.05$, unpaired t-test between HF-NI and HYP; [§] $p < 0.05$, unpaired t-test between HF-NI and N.

Metrics computed using the customized code, which considers all available contours.

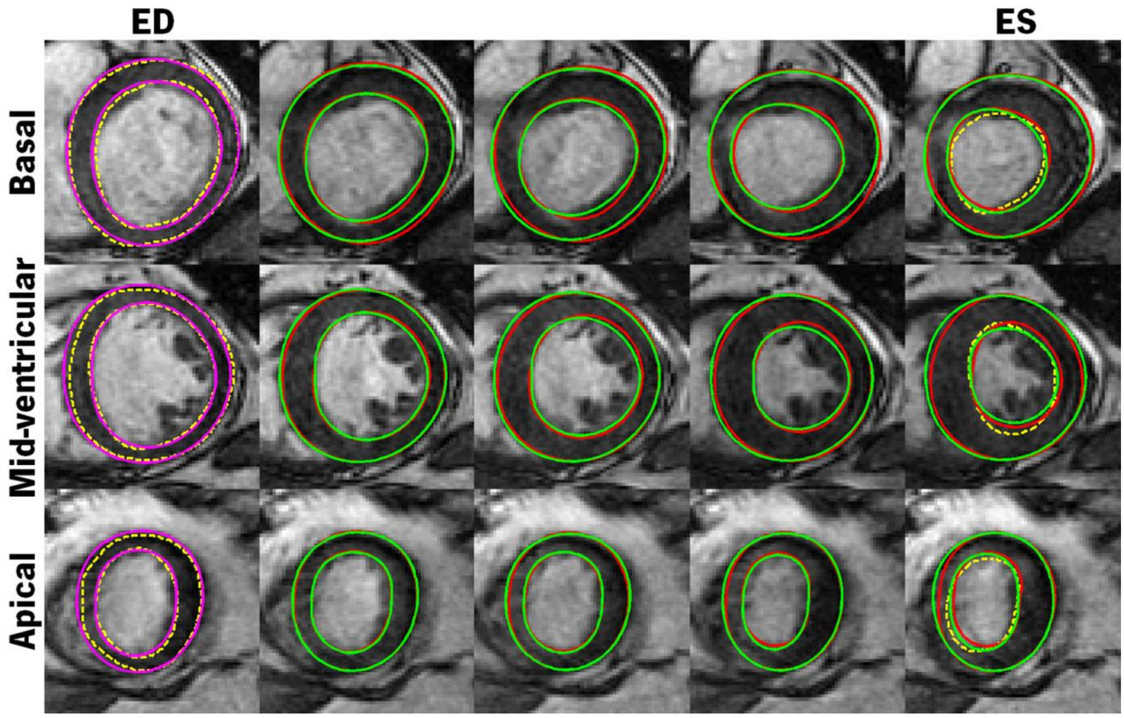

Figure 4.12 - Automatic 3D+time segmentation result using BEAS profile matching (BEASPM) and global optical flow method (OFT) for an example CMR dataset.

The presented SAX slices are from the HF-I-12 dataset, at phases number 20, 16, 13, 11 and 9 (magenta: automatic contour at ED phase; red: BEASPM; green: OFT; yellow: ground truth).

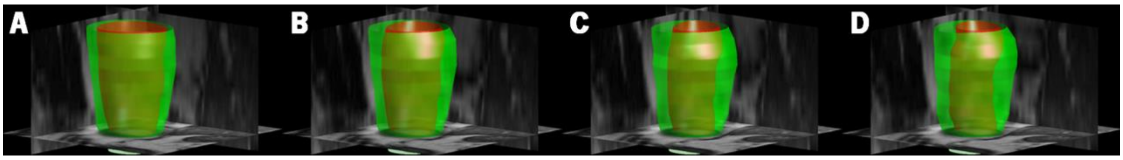

Figure 4.13 - 3D LV surface evolution from ED phase to ES phase using global optical flow method for an example CMR dataset.
The presented surfaces are from the HF-I-12 dataset, at phases **(A)** 20, **(B)** 16, **(C)** 11 and **(D)** 9.

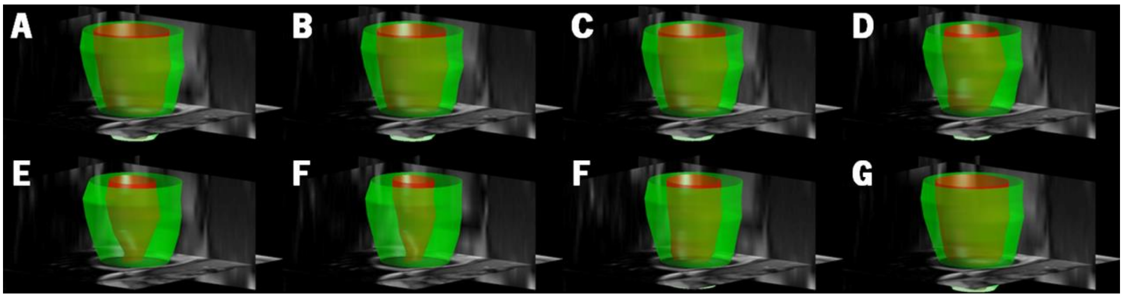

Figure 4.14 - Complete 3D LV surface evolution using global optical flow method for an example CMR dataset.
The illustrated surfaces represent a full cardiac cycle and are from the HYP-3 dataset, at phases **(A)** 20 (ED), **(B)** 17, **(C)** 14 **(D)** 11, **(E)** 10, **(F)** 8(ES), **(G)** 4, **(H)** 1.

Table 4.5 - Comparison of segmentation performance between proposed approaches and state-of-the-art (# = number of datasets).

Method	#	**Time (s)**	**Dice**		**APD** (mm)		**Good Contours** (%)	
			Endo	**Epi**	**Endo**	**Epi**	**Endo**	**Epi**
Proposed with BEASPM	45	15.9 ± 3.1	0.90 ± 0.04	0.94 ± 0.02	1.79 ± 0.42	1.80 ± 0.41	95.9 ± 7.7	95.4 ± 9.6
Proposed with OFT	45	11.1 ± 2.8	0.90 ± 0.05	0.94 ± 0.02	1.76 ± 0.45	1.80 ± 0.41	92.7 ± 9.5	95.4 ± 9.6
Constantinides *et al.* [78]	30	-	0.89 ± 0.04	0.92 ± 0.02	2.04 ± 0.47	2.35 ± 0.57	90.4	92.6
Constantinides *et al.* [45]	45	≈ 60	0.86 ± 0.05	0.91 ± 0.03	2.44 ± 0.56	2.80 ± 0.71	80 ± 16	71 ± 26
Hu *et al.* [43]	45	153.9 ± 32.1	0.89 ± 0.03	0.94 ± 0.02	2.24 ± 0.40	2.19 ± 0.49	91.1 ± 9.4	91.2 ± 8.5
Huang *et al.* [66]	45	-	0.89 ± 0.04	0.93 ± 0.02	2.16 ± 0.46	2.22 ± 0.43	79.2 ± 19.0	83.9 ± 16.8
Jolly [130]	30	≈ 60	0.88 ± 0.04	0.93 ± 0.02	2.26 ± 0.59	1.97 ± 0.48	95.6 ± 8.8	97.3 ± 5.8
Liu *et al.* [44]	45	129.5 ± 30.4	0.88 ± 0.03	0.94 ± 0.02	2.36 ± 0.39	2.19 ± 0.49	91.2 ± 8.5	90.8 ± 10.7
Schaerer *et al.* [131]	45	-	0.87 ± 0.04	0.92 ± 0.02	2.97 ± 0.38	3.14 ± 0.33	-	-
Uzunbas *et al.* [132]	15	≈ 45	0.82 ± 0.06	0.91 ± 0.03	2.98 ± 0.88	1.78 ± 0.35	-	-
Wijnhout *et al.* [133]	15	≈ 60	0.89 ± 0.03	0.93 ± 0.01	2.29 ± 0.57	2.28 ± 0.39	86.4 ± 11.0	94.2 ± 7.0

Metrics computed using original evaluation code, which considers only “good contours” for metrics computation.
BEASPM – BEAS profile matching; OFT – global optical flow tracking.

To better understand the computational burden of each module of the proposed framework, the average computational time for each step is reported in Table 4.6, along with the average total computational time to segment a dataset using each proposed tracking algorithm.

Concerning the validation of clinical parameters, the correlation coefficient obtained by regression analysis, and both bias and limits of agreement (LOA) obtained by Bland-Altman analysis are presented in Table 4.7 for both tracking methods and for both versions of evaluation code (OC and CC). Figure 4.15 and Figure 4.16 present the linear regression and Bland-Altman plots, respectively, obtained for EDV, ESV, LVM and EF using BEAS profile matching (computed using the customized code). Global optical flow tracking plots are not presented due to their similarity with local tracking method (see Table 4.5).

Table 4.6 - Average computational time for each step of the proposed approach (# = 45, $\mu \pm \sigma$).

Method	**Time** (s)	
LV Location	0.10 ± 0.02	
Template Matching	1.16 ± 0.37	
2D Segmentation	0.22 ± 0.05	
Stack Initialization	0.55 ± 0.10	
3D Segmentation	6.21 ± 2.41	
Profile Matching	7.62 ± 0.80	-
Anatomical OFT	-	2.89 ± 0.49
Total	15.86 ± 3.06	11.13 ± 2.76

Table 4.7 - Linear regression and Bland-Altman analysis for clinical cardiac indices for both tracking methodologies (# = 45).

	Code		**EDV**			**ESV**			**SV**			**LVM**			**EF**	
		R	**Bias**	**LOA**	**R**	**Bias**	**LOA**	**R**	**Bias**	**LOA**	**R**	**Bias**	**LOA**	**R**	**Bias**	**LOA**
BEASPM	OC	-	-	-	-	-	-	-	-	-	0.906	-0.01	35.76	0.962	1.11	10.49
	CC	0.985	-2.46	29.46	0.991	-3.31	24.57	0.924	0.85	21.01	0.951	5.51^{*}	27.70	0.976	1.03	9.25
OFT	OC	-	-	-	-	-	-	-	-	-	0.906	-0.01	35.76	0.977	2.45^{*}	9.47
	CC	0.985	-2.46	29.46	0.988	-3.83	28.96	0.855	1.38	15.82	0.951	5.51^{*}	27.70	0.976	3.00^{*}	10.97

* $p < 0.05$, paired t-test against zero.

Original code (OC) only considers “good contours”, while the customized code (CC) uses all segmented slices.

BEASPM – BEAS profile matching; OFT – global optical flow tracking.

Limits of agreement (LOA) represented as ±1.96σ.

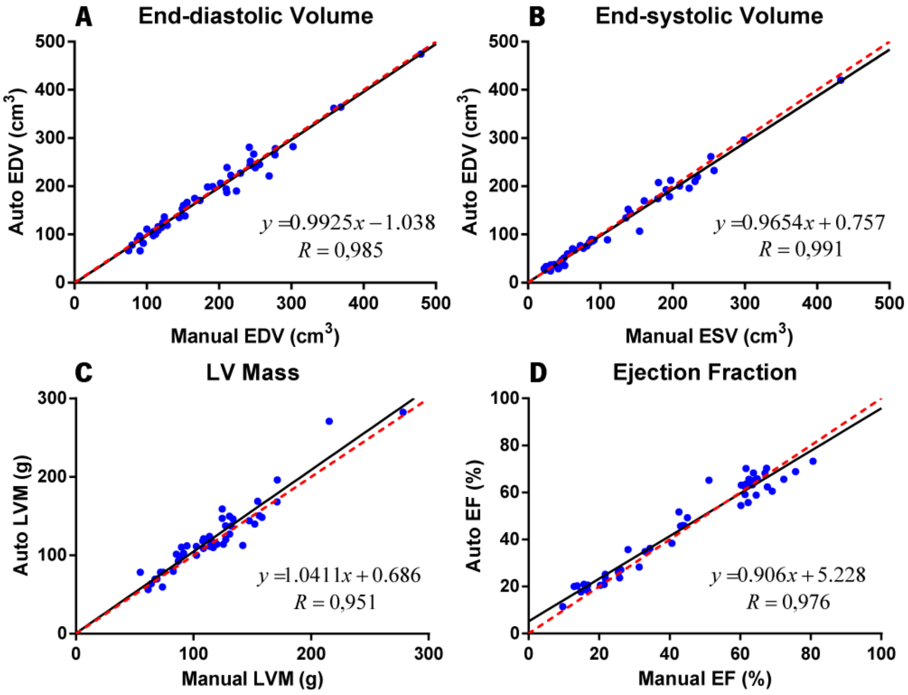

Figure 4.15 - Linear regression for (A) end-diastolic volume (EDV); (B) end-systolic volume (ESV); (C) left ventricular mass (LVM); and (D) ejection fraction (EF) using BEAS profile matching.

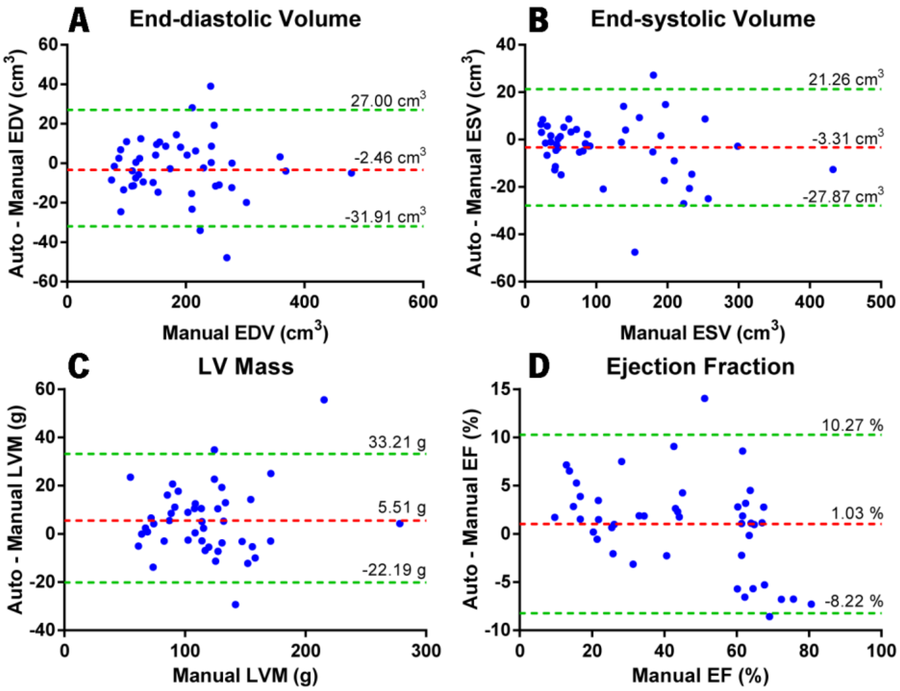

Figure 4.16 - Bland-Altman analysis for (A) end-diastolic volume (EDV); (B) end-systolic volume (ESV); left ventricular mass (LVM); and (D) ejection fraction (EF) using BEAS profile matching.

5. Discussion

5. Discussion

5.1 Automatic Mid-ventricular Initialization

The first module of the proposed framework intends to achieve an automatic initialization for endo and epicardial contours in a mid-ventricular slice at the ED phase. To accomplish this, the methods in [67] and [110] were modified and combined to detect the elliptical left ventricular myocardial shape in SSFP sequences.

The proposed method for automatic LV localization was found to be superior to the method of Lu *et al.* [67], retrieving a correct LV centroid for the 45 mid-ventricular slices (against only 36 using the original method). These results are mainly due to the multilevel Otsu thresholding employed, which decreases the method's dependency on the image signal intensities by describing it with an increased number of classes [Figure 4.2]. Moreover, by adding the distance to the image's center in the cost function, the robustness was improved by avoiding misinterpretation when other circular objects exist in the image [Figure 4.2]. Although we added an assumption of 4 classes and had to perform the subsequent class decomposition, the method seems generic and we expect it to remain valid if applied to other datasets. Moreover, although this methodology is designed for cine SSFP sequences where the blood appears brighter, the left ventricle localization in dark-blood sequences would be straightforward by simply redefining the assumption of a brighter cavity (inverting it to a darker one).

On the other hand, the proposed elliptical annular template matching algorithm provided a higher feasibility than the original circular template matching method in [110], with 91.1% (41/45) of feasibility against 71.1% (32/45). Thus, it was found to be superior in estimating the initial contours, as it allows searching for elliptical shapes rather than only circular ones. This fact is particularly relevant considering that several cardiomyopathies lead to significant geometrical distortion of the normal LV ellipsoidal shape. Moreover, the proposed approach avoids the need for an image normalization step and an intensity-based search, since it uses the normalized cross-correlation of an object with a dark ring template. Again, such assumptions could be easily adapted to dark-blood sequences by simply inverting the intensity transitions between searched object and background in the computed kernels. Despite the increased feasibility, according to the chosen validation criterion, four cases were considered wrongly initialized [Figure 4.4]. The analysis of these cases showed that, in part, it is a result from incomplete object detection in the previous LV localization step [Figure 4.4B-D]. Note that the LV centroid is correct, but the presence of TPMs hampers the complete cavity detection. In fact, when in combination, the presence of loose papillary muscles can help misguide our template matching towards a partial LV cavity [Figure 4.4B-C]. At last, in one dataset, the presence of a thin myocardial wall close to the lungs leaded to a wrong detection of the myocardium (i.e., the lungs' dark signal intensity can be interpreted as myocardium when lacking a sufficiently thick wall) [Figure 4.4A].

In sum, the proposed algorithms achieved a high feasibility and robustness against the diversity of image characteristics (e.g., artifacts, surrounding structures, presence of TPMs, image contrast, etc.), providing consistent initializations for the subsequent steps of the proposed approach.

5.2 Coupled Myocardial 2D Segmentation

The second module focuses on segmenting the initialized mid-ventricular slices using the BEAS framework. A CMR-targeted energy was designed to accomplish this task, by including a weighted energy formulation and specific region-based energies for each contour according to their characteristics. The SLY energy was chosen for the endocardium to take advantage of the known intensity relation between cavity and myocardium. On the other hand, the LCV energy was chosen for the epicardium based on the unpredictability of the outer region and due to the similar intensity means between myocardium and surrounding tissues. Moreover, a coupled formulation is used, searching for a combined global optimum with separate control over the myocardium shape and thickness.

According to Table 4.1, the proposed automatic initialization reduces the segmentation accuracy compared to a manual initialization (C against A and D against B). Nonetheless, when combined with the proposed energy, it preserves the segmentation accuracy while avoiding the need for a manual initialization (D against A – no significant difference). When analyzing the proposed energy only (D against C and B against A), the accuracy increased in the three measured metrics for both endo and epicardial contours. Figure 4.5 visually presents such increased accuracy. In fact, the weighted formulation pushes the epicardium closer to the myocardium, avoiding being trapped in outer boundaries (e.g., between pericardium and lungs or in RV trabeculae) [Figure 4.5E-H]. Moreover, it also helps delineating the endocardium by surpassing the presence of trabeculae and papillary muscles [Figure 4.5A and C]. At last, note that each contour evolves towards a well-defined boundary according to the region-based energies principles. However, occasionally, the physician draws the contours differently based on his notion of trabeculae and based on the remaining spatiotemporal information at other slices (which are not used at this stage) [Figure 4.5B]. Such situation can lead to differences in the segmentation when compared to manually drawn contours, without effectively being an ill-defined segmentation. The same remarks on the energy features were observed in Figure 4.6 and Figure 4.7, with the CMR-targeted energy being able to surpass the presence of TPMs and to evolve towards the true boundaries by taking advantage of the respective energy principles. Such results reinforce the robustness of the proposed energy against initialization (in the present case, for both automatic and manual ones).

In summary, the proposed energy functional for 2D segmentation shown to be efficient and robust to obtain a first mid-ventricular delineation for further initialization and segmentation, even in a database with a wide range of pathological cases, anatomy and image contrast.

5.3 Coupled Myocardial 3D Segmentation

The two previous modules (first conceptual block of the framework) focused on obtaining an accurate and automatic segmentation for a mid-ventricular slice at the ED phase. In the second conceptual block, a full 3D segmentation at the ED phase is intended. To this end, two modules were designed and presented: an automatic stack initialization and a 3D segmentation algorithm.

Concerning the proposed automatic stack initialization, it was able to retrieve fairly close coarse delineations for both endo and epicardial contours. In fact, it even recovers from the four wrongly initialized images in the previous step, allowing us to include them in the subsequent 3D and 3D+time analysis. The ability to include these images may be linked to the robustness of the EM algorithm and the simple but powerful principle of thresholding. In other words, even if the initial 2D mid-ventricular segmentation has a less accurate result, the applied mask and subsequent EM algorithm still allow a good estimation of the intensity distributions for the LV cavity and myocardial wall. After properly estimating the two gaussian distributions parameters, both myocardial and cavity intensity thresholds are also appropriately defined. Consequently, the initial contours obtained for all slices from base to apex are fairly close to the real boundaries, which permit the proposed 3D localized energy functional to obtain an accurate result during segmentation. Moreover, the proposed method is at the same time able to adequately correct occasional misalignment between slices. Such feature is possible due to the center re-estimation during contour growing, which adapts itself to dataset-specific motion artifacts [Figure 3.10].

Thus, during segmentation a true three-dimensional modeling of the LV surface is possible, allowing a 3D spatial continuous delineation to be obtained.

Regarding the subsequent segmentation, the proposed BEAS extension and associated hybrid energy functional proved to give accurate results in all 4 metrics used [Table 4.2]. In fact, the accuracy was higher compared to the 2D mid-ventricular segmentation [Table 4.1], with negligible difference between manual and automatic initializations. This last result is mainly due to the robustness of the automatic stack initialization procedure, which is fairly insensitive against the 2D segmentation obtained in the previous stage (as stated above). Analyzing Table 4.2, we observe that a high percentage of “good contours” was obtained, with an average of 97.4% and 95.4% for endo and epicardial contours, respectively. Usually, the slices considered bad were in the apex (due to its small size and low contrast with its background) or in basal slices in the presence of left ventricular outflow tract. The latter problem was still not directly addressed in the proposed framework, being only avoided in most cases by the smoothing factor chosen (see Figure 4.10A). Nevertheless, it increases the measured distances and is the main contributor to the reported average Hausdorff distance. Note the increased average and standard deviation in this metric when considering all slices (CC compared to OC), although only a few percentages of contours are added. As expected, the reported values for the customized code are worse due to the inclusion of slices considered poorly segmented. Such results reinforce the need to look together for the performance metrics and percentage of “good contours” when using the original evaluation code.

Figure 4.8 gives an overview of the proposed methodology performance in segmenting the ED phase, with approximately 75% of the studied datasets with a Dice metric higher than 0.90 for both endo and epicardial contours. At the same time, these datasets also present an APD under 2 mm for both contours and a maximum local error around 4 - 5 mm. Taking into account the observed outliers, it is important to note that two of these are from the four cases having a poor 2D initialization. The other outliers are associated with datasets with considerable heterogeneity between slices, hampering the correct automatic initialization of apical and basal slices further away from the initial mid-ventricular slice when using our threshold-based strategy.

Regarding the errors distribution from base to apex, the analysis of Figure 4.9 allows to conclude that although the median value is not significantly different across the entire LV, the average value (crosses) show a tendency for higher errors in basal and apical slices, rather than in mid-ventricular ones. Such result is primarily linked to the occurrence of poorly segmented slices at the two ends of the LV (due to the LVOT in basal slices and to PVE in apical ones, as stated above). Notwithstanding, overall the segmentation is robust independently from the slice level.

Figure 4.10 confirms the robustness of the proposed 3D segmentation against different myocardial intensities, contrast and presence of TPMs (note the second mid-ventricular slice in Figure 4.10B). Moreover, the illustrated LV surfaces in Figure 4.11 reinforce the interest of the misalignment correction step and the three-dimensional spatial continuity of the segmentations. The analysis of the importance of each proposed feature (Appendix B) lead to the conclusion that the added weights influence the result most, followed by the SLY energy used for the endocardium and the edge-based energy term in the epicardium. Moreover, the 3D segmentation results showed to be stable against variations in the chosen parameters (Appendix C), which gives crucial insights about the robustness of the present algorithm.

5.4 3D+time Tracking

The third and last conceptual block of the proposed framework aims to track endo and epicardial contours throughout the cardiac cycle, in order to obtain these contours at the ES phase for clinical parameters computation. In Section 3.6, we presented two methods for LV CMR tracking, i.e. the BEAS profile matching and the global optical flow tracking, whose results were presented in Section 4.6. According to these results, an accurate tracking was achieved in the 3D+time approach, independently of the tracking methodology used [Table 4.3, Table 4.4]. However, a decrease in the endocardium accuracy for the 3 measured metrics is detected compared to the aforementioned 3D results [Table 4.2]. This remark is in part related with the greater difficulty in distinguishing the compacted TPMs from the myocardial tissue in ES slices. Note that the epicardial results are unchanged as they are not evaluated in the ES phase due to lack of manual contouring. Nevertheless, the percentage of “good contours” is still high for the endocardium, with an average 95.9% for BEASPM and 92.3% for OFT. Moreover, the APD for both endocardium and epicardium are kept around 2 mm when considering all contours in both ED and ES phases (CC). When dividing the studied datasets by pathology, no significant difference is found between average APD between these groups. Regarding the Dice metric, significant differences were found for the endocardial contour between some groups. However, this can be related to the different cavity size between groups of subjects, since the differences in average APD are not significant. In sum, these results suggest that the proposed algorithm is robust against different pathologies and ventricle's anatomy and function. Additionally, the achieved LV surfaces are spatially smooth and remain so throughout the cardiac cycle [Figure 4.13, Figure 4.14]. As expected, the left ventricle starts relaxed, contracts until the end-systole phase, and relaxes back until it acquires its initial state [Figure 4.14].

The comparison between local and global tracking methods is not conclusive, although a trend for higher performance of BEASPM over OFT is observed for the studied datasets. Figure 4.12 depicts some differences between methods but these are not consistent or significant. Note that BEASPM tracks the LV motion locally, but the implicit smoothing associated with BEAS formulation keeps it properly delineated and without jittered contours. On the other hand, OFT searches for motion locally but integrates it in a global affine motion transformation (hence its designation of global tracking). These principles can explain the similarities in the tracking between both methods. Notwithstanding, OFT has the tendency of tracking the endocardial border close to the LV blood pool, disregarding the appearance of more pronounced TPMs after contraction (note the significant bias in EF in Table 4.7). BEASPM, due to the pattern tracking principle and motion penalization, is better suited to keep the contour around TPMs throughout the cardiac cycle. However, OFT is more generic will less parameters to define (only generic ones that mostly affect CPU time and not accuracy), while BEASPM can be more influenced by the dataset's pixel spacing, temporal resolution and contrast throughout the frames [80]. Concerning the measured computational times, OFT is faster than BEASPM, mainly because the latter requires local evolution of both endo and epicardial contours (see Table 4.6). In summary, the difference between local and global tracking performance is inconclusive until further evaluation on different datasets with higher variability of resolution, contrast and ventricle's contraction.

One should note that the proposed framework does not track the mitral valve plane throughout the cardiac cycle. Instead, we ask the user to input two points in the basal and apical slices at ES phase (in fact, they are obtained looking to the reference manual contours). This strategy was employed to allow direct comparison between the expert contours and the automatic ones (to obtain the above performance metrics). In practice, the ES phase could be automatically determined using the LV cavity's volume (smaller one), which could be different from the manually selected one. Note that the ES phase was visually chosen during manual contouring, which does not mean it is completely correct (see Section 2.1). Concerning the basal and apical slices, they cannot be reliably defined without long-axis views (remember the different arbitrary criterions possible for SAX-derived base identification - Section 2.1). As the main goal of this thesis was to design a segmentation framework for SAX CMR images (LAX views are not always acquired), the information on the mitral valve plane cannot be reliably estimated and we chose to ask for user input to overcome this limitation. In the future, we intend to include the possibility of using LAX views (if acquired) to avoid user input and to track the LV longitudinal contraction automatically. Such strategy was reported as more robust and viable for LV base identification [36, 58].

According to Table 4.5, the proposed framework proved to be competitive to the state-of-the-art frameworks that used the MICCAI database for validation, providing leading results for both accuracy and computational times. This observation was valid for all segmentation performance measures employed, with a smaller average APD, superior Dice metric and higher percentage of "good contours". Note that the original evaluation code only considers "good contours" for computation of mean, implying that our results are more accurate even including a higher percentage of slices. At the same time, the framework showed to be very fast [Table 4.6], presenting an average total computational time of 15.86 ± 3.06s or 11.16 ± 2.76s per dataset (around 0.06 – 0.09s per image) in a MATLAB implementation. A faster framework can be achieved if implemented in a compiled language, such as C++. Moreover, since a fully manual contouring takes between 6 to 20 min for only ED and ES phases [29, 36, 37], the proposed framework already seems to be fast and accurate enough to be of interest in daily clinical practice. Additionally, it can add clinical relevant information by using the full 3D+time delineations to compute the volumes changes and corresponding change velocities throughout the cardiac cycle [16].

Linear regression revealed a high correlation for all clinical cardiac indices, ultimately showing the accuracy and interest of the proposed framework for automatic assessment of LV morphology and global function [Table 4.7, Figure 4.15]. Again, no major difference was found between both tracking methodologies, with BEASPM having a slightly better correlation for ESV while OFT presents a higher correlation for SV. Regarding Bland-Altman's limits of agreement [Figure 4.16], the reported values are slightly higher than other frameworks in the literature [38, 41]. Nonetheless, these methods require some level of user interaction for the segmentation process [41] or were only validated on patients with a specific pathology [38]. In our case, a fully automatic framework is being proposed and validated on a database with both healthy subject and patients, which demands a generic framework. Additionally, the method in [38] takes about 1h to segment a 4D dataset in a C++ implementation, while in [41] 181.3s are required in average using a MATLAB implementation. In the present work, the proposed framework requires less than 16s for the segmentation of a 4D dataset.

5.5 Preliminary conclusions

In summary, a novel fully automatic 3D+time segmentation framework for CMR datasets was presented, studied and validated. The proposed approach showed to be efficient, accurate, robust and fast compared to the available state-of-the-art frameworks, presenting leading results in both accuracy and average computational time in the common database used for comparative purposes. The average computational time to analyze a dataset was in average under 16s, with an overall correlation with reference contours of, approximately, 0.99, 0.99, 0.92, 0.95 and 0.98 for EDV, ESV, SV, LVM and EF, respectively. Such results show the appeal of the proposed framework for automatic assessment of LV morphology and global function in daily clinical practice. Nevertheless, we intend to validate the proposed framework on a different database with “real-world” variability in both contrast and anatomical and functional characteristics to further understand the interest and general robustness of the proposed methodology. Such clinical validation is presented in the following chapter.

6. Clinical Validation

6. Clinical Validation

In the present chapter, we intend to further evaluate the proposed framework in order to assess its potential clinical added value. To this end, a feasibility study and practical validation in a clinical setting is presented using a large database acquired for an ongoing multi-center clinical trial. This data corresponds to patients with suspicion of ongoing (chronic) myocardial ischemic disease and has been acquired in different laboratories across Europe, while being analyzed in a core lab whose expertize focuses on MR imaging. The present validation is crucial to test the robustness of the presented framework against clinical variability, where considerable shape, function and image brightness variations of the left ventricle across subjects are observed [Figure 6.1]. Moreover, taking into account the often sub-optimal image quality in the clinical setting [36], this study allows a complete assessment of the algorithm performance.

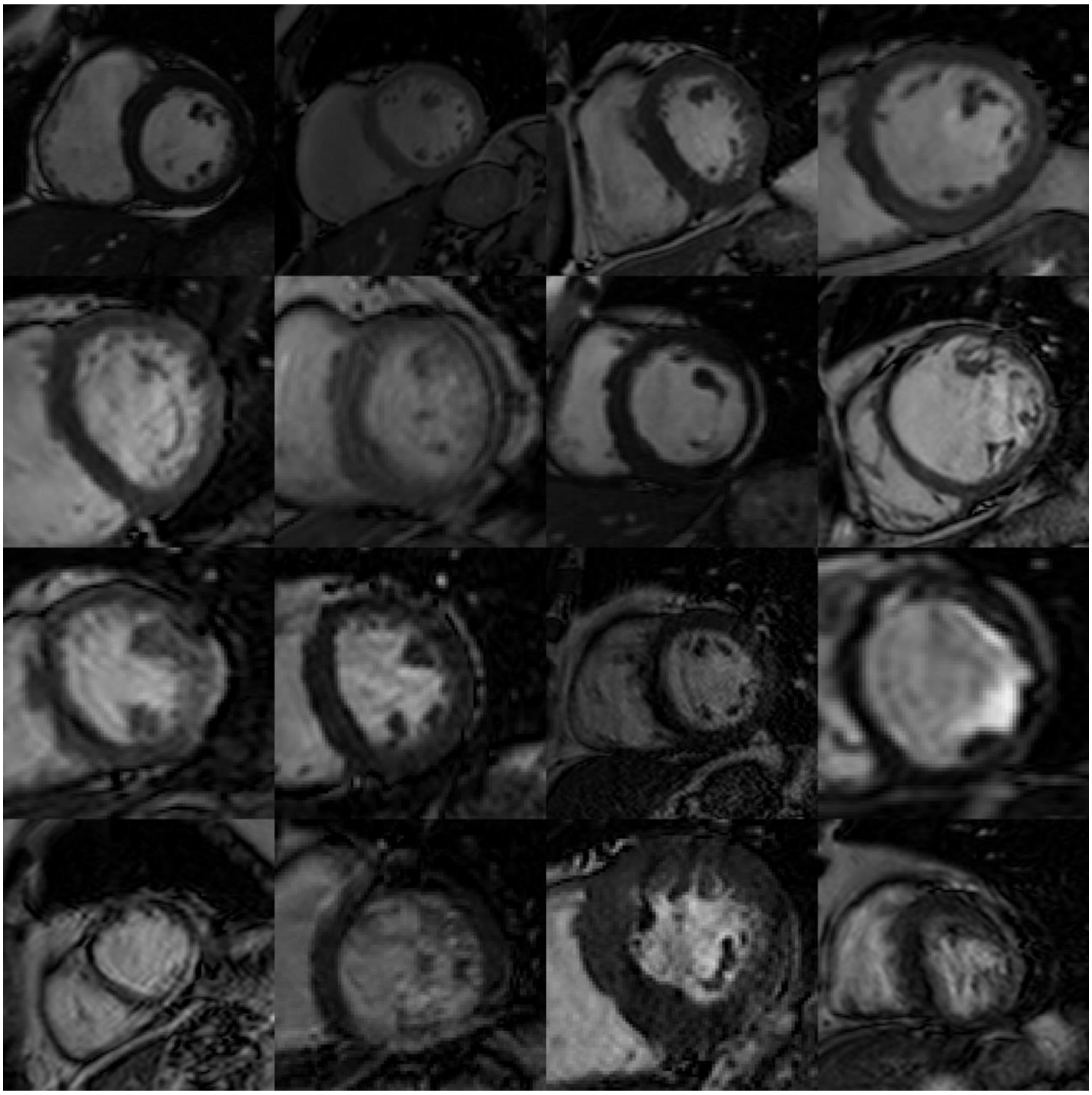

Figure 6.1 - Left ventricle variability at mid-ventricular slice across subjects in the clinical trial data.

6.1 Data

The clinical trial database currently includes 318 cardiac MRI datasets, with a temporal resolution of 30 phases over the cardiac cycle. Per patient, six to thirteen 2D SAX slices were obtained from the atrioventricular ring to the apex, with an isotropic pixel spacing ranging from 1.11 to 1.56mm. For each dataset, reference contours, drawn by an experienced cardiologist, are available for all slices for both endocardium and epicardium at the ED and ES phases. Furthermore, reference clinical values for EDV, ESV, SV, LVM and EF from blinded core lab analysis are also available. All reported results consider manual contours drawn to include TPMs in the LV cavity.

6.2 Experiments

To quantify the applicability of the proposed framework for automatic LV segmentation, its global feasibility was tested by considering a successful initialization when the detected and delineated object roughly corresponds to the LV. In other words, if any of the initialization steps (LV localization, template matching or stack initialization) fails to correctly detect and/or roughly delineate the LV (by visual inspection), one considers the current analysis incorrect.

On the other hand, to evaluate the accuracy of the segmentation, the customized evaluation code employed in the technical validation (Section 4.2) was used. The evaluation code calculates the Dice metric, the average perpendicular distance (APD), the percentage of “good contours” (contours for which the APD is less than 5mm) and the Hausdorff distance.

Moreover, the cardiac indices used in daily clinical practice, namely EDV, ESV, SV, LVM and EF, are also estimated for each dataset. Linear regression and Bland-Altman analysis [129] were then performed to assess the correlation and agreement between reference clinical indexes and the automatically computed ones.

Finally, the average total computational time required to segment a 4D dataset was measured. The reported CPU times were obtained using MATLAB code running on a 2.4 GHz dual-core laptop.

6.2 Results

Based on the abovementioned criterion, the proposed framework yielded a feasibility of 95% (302/318). From the 16 datasets (5.0%) considered incorrectly analyzed, 7 were related to the LV localization step (2.2%), 5 to the template matching procedure (1.6%) and 4 to the stack initialization (1.2%). Figure 6.2 presents one example for each of the causes mentioned.

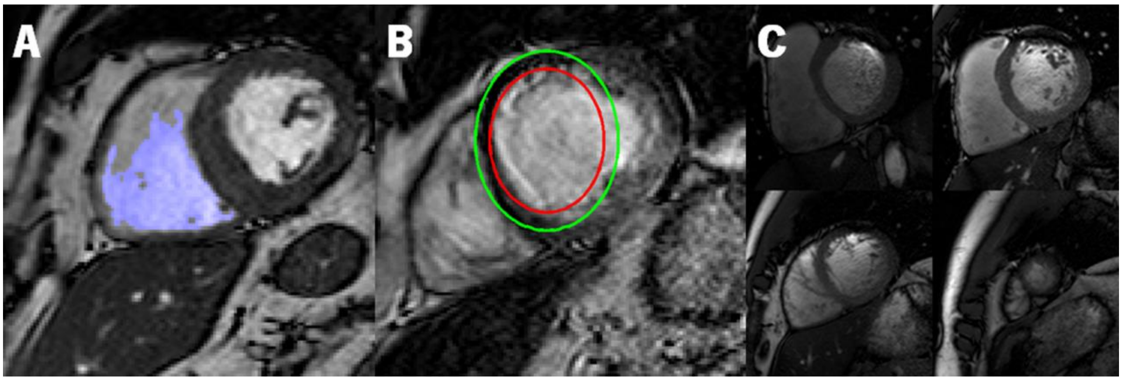

Figure 6.2 - Causes of incorrect analysis of datasets in the clinical trial database.
(A) LV localization failure due to non-centered LV; **(B)** elliptical template matching failure due to non-uniform wall thickness and sub-optimal image quality; and **(C)** dataset with considerable heterogeneity across slices in the ED phase, which lead to incorrect automatic stack initialization due to improper thresholds definition.

Concerning the 3D+time myocardial segmentation, Table 6.1 presents the overall segmentation plus tracking performance, considering all 302 correctly initialized datasets, for both local and global tracking methods. Based on the results in Table 6.1 and linear regression between automatic and reference clinical values for BEASPM (data not shown), OFT outperforms BEASPM in the clinical trial database, showing increased robustness and stability against clinical variability. Note that for clinical indices computation, the endocardial contour delineation in the ES phase is used, while the epicardial one is discarded. Therefore, taking into account that OFT performed better for the endocardium, it is reasonable to conclude that OFT best fits the needs of the clinical practice. Consequently, the remaining results will focus only on this approach.

To also assess the overall performance distribution rather than only average results, Figure 6.3 presents the boxplots for each metric for both endocardial and epicardial contours in the full 3D+time analysis. Moreover, the spatial error distribution from basal to apical slices of both APD and Hausdorff distance metrics are illustrated in Figure 6.4.

Figure 6.5 illustrates three example segmentations in the ED phase using the proposed 3D segmentation algorithm. Figure 6.6 and Figure 6.7 present two segmentation and tracking results. Moreover, two complete 3D LV surface evolutions, illustrating the full cardiac cycle, are presented in Figure 6.8 and Figure 6.9.

Table 6.1 - 3D+time segmentation performance for endo and epicardial contours for the clinical trial database (# = 302, $\mu \pm \sigma$).

Method	**Dice**		**APD** (mm)		**Hausdorff** (mm)		**Good Contours** (%)	
	Endo	**Epi**	**Endo**	**Epi**	**Endo**	**Epi**	**Endo**	**Epi**
BEASPM	0.86 ± 0.05	0.90 ± 0.03	2.25 ± 0.90	2.69 ± 0.88	4.99 ± 1.71	5.77 ± 1.68	90.7 ± 10.7	89.4 ± 9.3
OFT	0.88 ± 0.04	0.90 ± 0.04	1.91 ± 0.71	2.76 ± 0.90	4.59 ± 1.65	5.95 ± 1.76	93.8 ± 6.8	88.7 ± 9.2

All differences between methods are significant ($p < 0.05$, paired t-test).

Regarding the automatically computed clinical parameters, the correlation coefficient obtained by regression analysis, and both bias and limits of agreement (LOA) obtained by Bland-Altman analysis are presented in Table 6.2 for all 5 clinical indices considered. Moreover, Figure 6.10 and Figure 6.11 present the linear regression and Bland-Altman plots, respectively, obtained for EDV, ESV, LVM and EF.

Finally, the average computational time to segment a 4D dataset was 11.00 ± 2.83s.

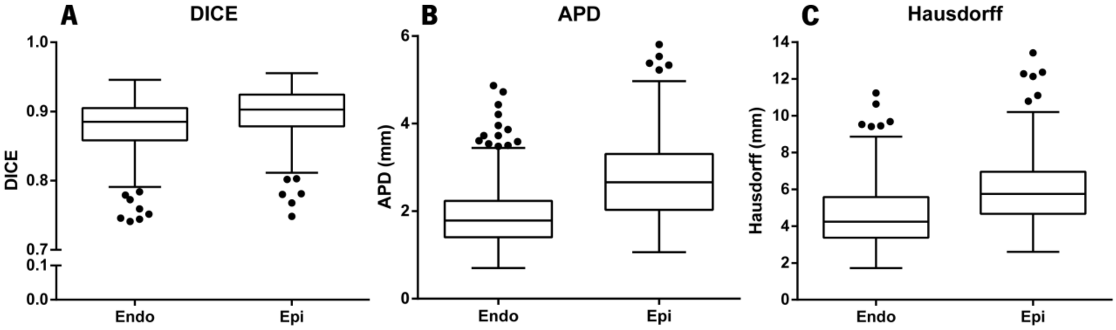

Figure 6.3 - Boxplots of computed (A) Dice metric, (B) APD and (C) Hausdorff distance for both endo and epicardial contours using the proposed 3D+time framework (# = 302).

The ends of whiskers represent the lowest and highest datum still within 1.5 times the inter-quartile range of the lower and upper quartile, respectively. Any data value larger is considered an outlier and plotted as a dot. The results were obtained using global anatomical optical flow method.

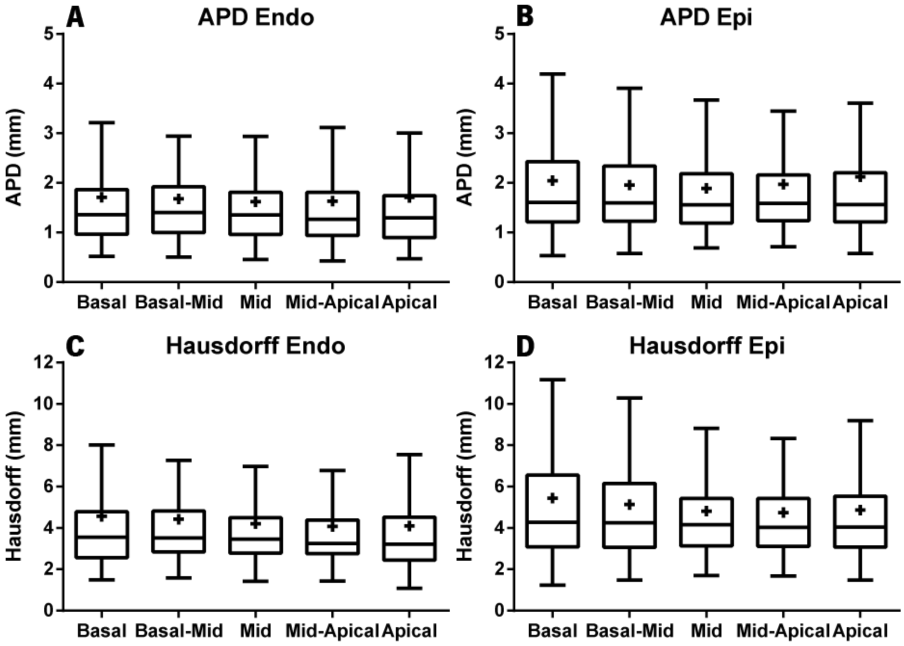

Figure 6.4 - Boxplots for APD and Hausdorff metrics distribution from basal to apical slices using the proposed automatic 3D+time framework (# = 302).

(A) APD for endocardial contour; **(B)** APD for epicardial contour; **(C)** Hausdorff distance for endocardial contour; **(D)** Hausdorff distance for epicardial contour. The ends of the whiskers represent the lowest and higher datum still within 1.5 times the inter-quartile range of the lower and upper quartile, respectively. The crosses represent the mean values for each metric. The results were obtained using global anatomical optical flow method.

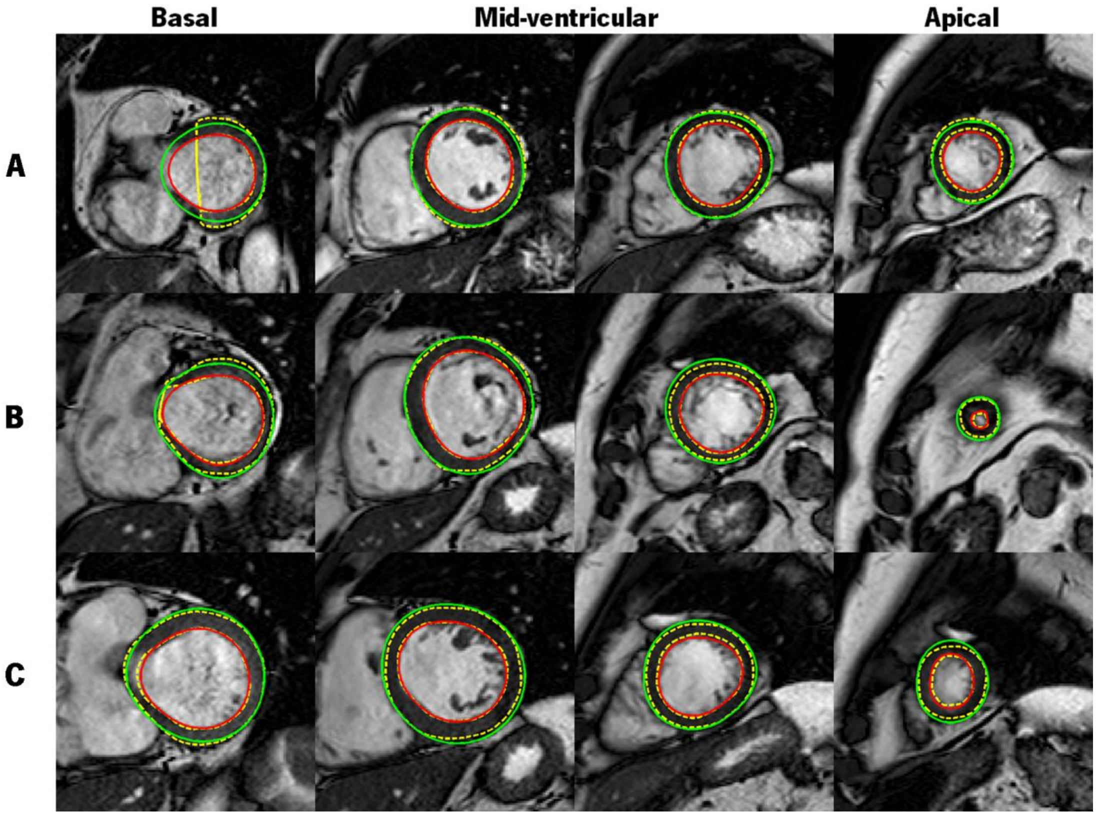
Basal
Mid-ventricular
Apical
A
B
C

Figure 6.5 - Automatic 3D segmentation results for 3 CMR datasets from the clinical trial database.
The presented slices are from the following datasets: **(A)** 5165, **(B)** 6690 and **(C)** 6694 (red: endocardium; green: epicardium; yellow: ground truth).

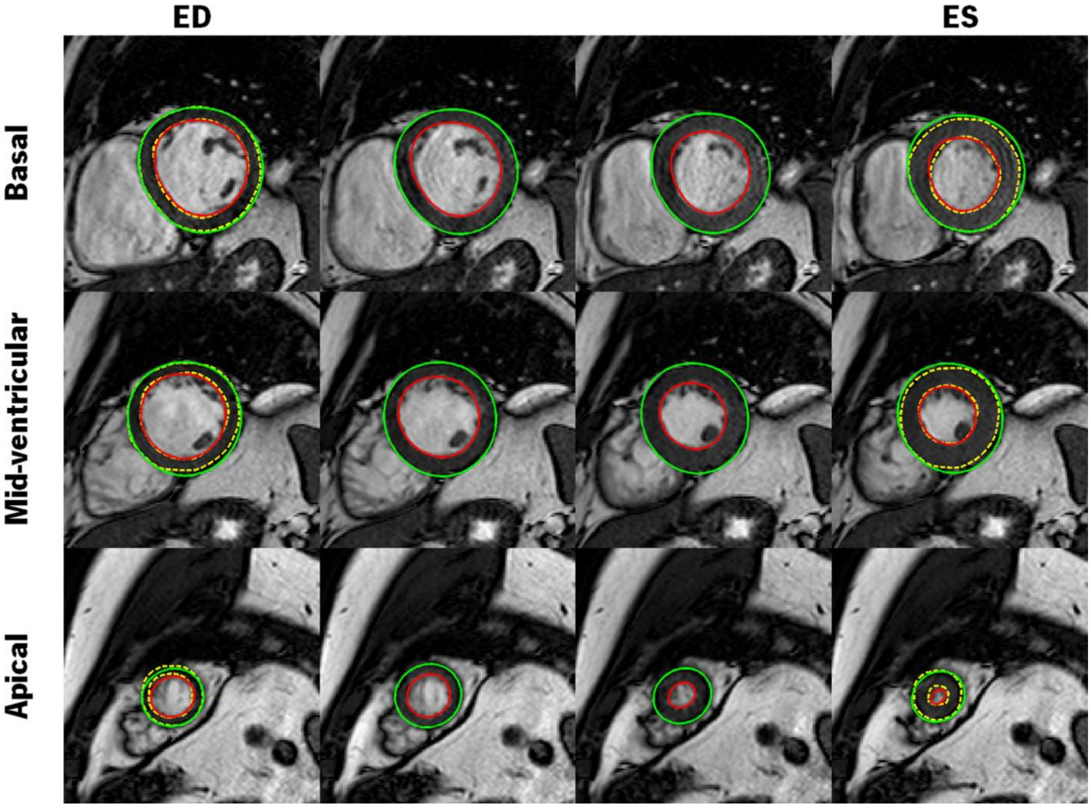
ED
ES
Basal
Mid-ventricular
Apical

Figure 6.6 - Automatic 3D+time segmentation and tracking result using global optical flow method for dataset 5192 from the clinical trial database.
The SAX slices are from phases 1, 4, 8 and 12 (red: endocardium; green: epicardium; yellow: ground truth).

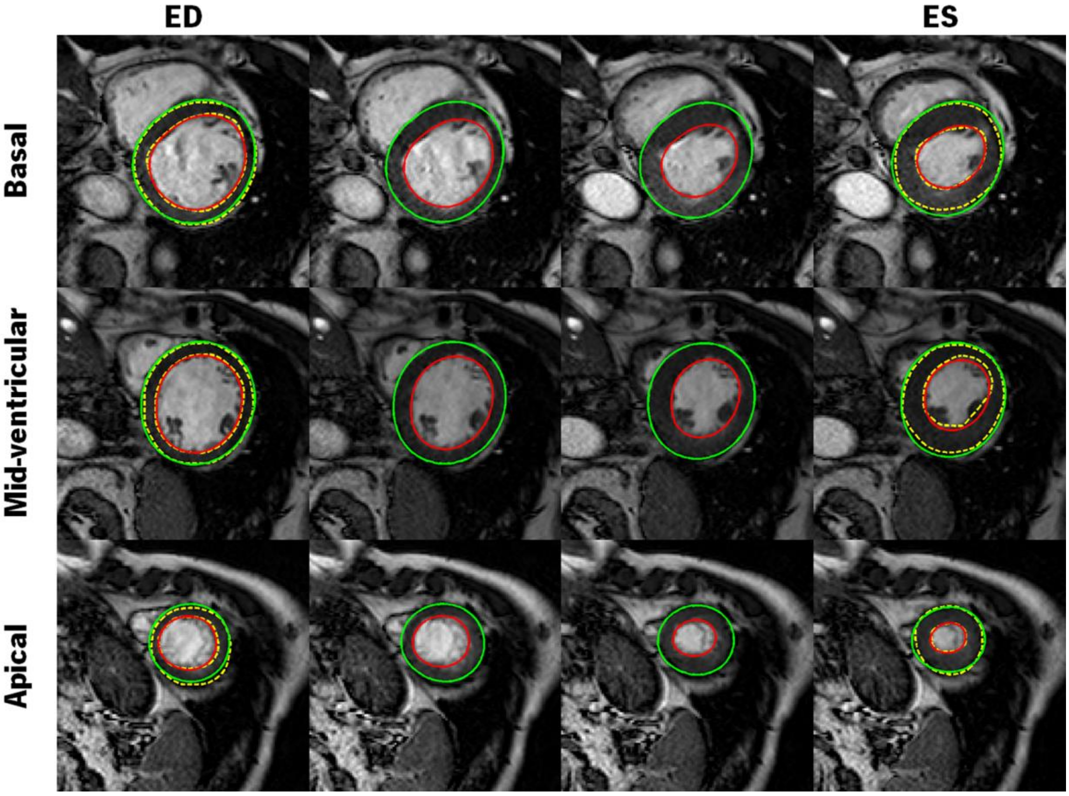

Figure 6.7 - Automatic 3D+time result for dataset 6509 from the clinical trial database.
The SAX slices are from phases 1, 4, 8 and 12 (red: endocardium; green: epicardium; yellow: ground truth).

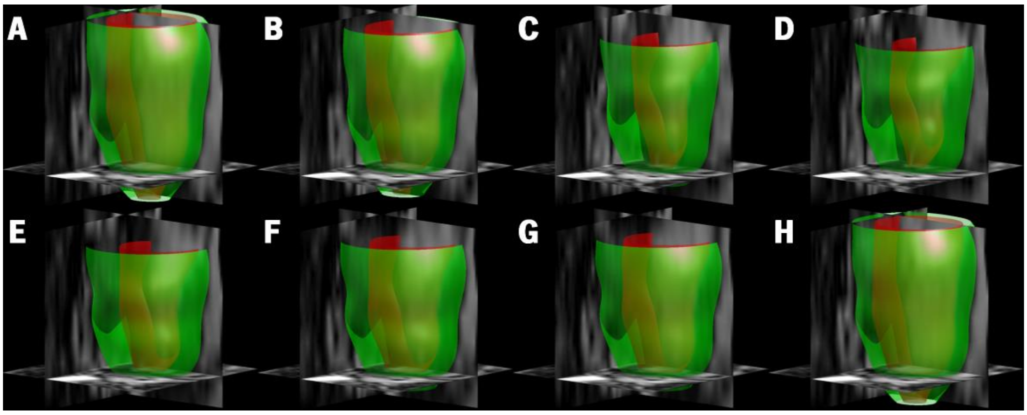

Figure 6.8 - Complete 3D LV surface evolution for dataset 5050 from the clinical trial database.
The illustrated surfaces represent a full cardiac cycle, more precisely at phases **(A)** 1 (ED), **(B)** 5, **(C)** 10 **(D)** 14 (ES), **(E)** 17, **(F)** 21, **(G)** 25, **(H)** 30.

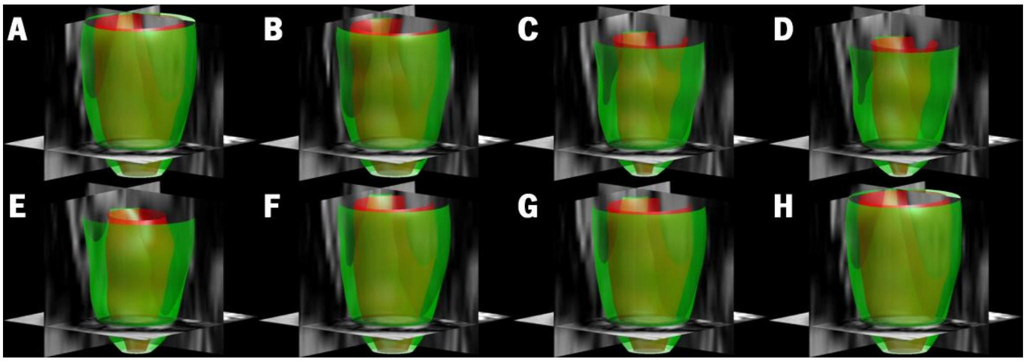

Figure 6.9 - Complete 3D LV surface evolution for dataset 5145 from the clinical trial database.
The illustrated surfaces represent a full cardiac cycle, more precisely at phases **(A)** 1 (ED), **(B)** 5, **(C)** 9 **(D)** 12 (ES), **(E)** 15, **(F)** 20, **(G)** 25, **(H)** 30.

Table 6.2 - Linear regression and Bland-Altman analysis for the clinical indices studied (# = 302).

	EDV			ESV			SV			LVM			EF	
R	Bias	LOA	R	Bias	LOA	R	Bias	LOA	R	Bias	LOA	R	Bias	LOA
0.985	-4.08*	17.60	0.981	1.18*	19.09	0.906	-5.26*	17.80	0.840	20.41*	39.94	0.920	-1.53*	9.66

* $p < 0.05$, paired t-test against zero.

Limits of agreement (LOA) represented as ±1.96σ.

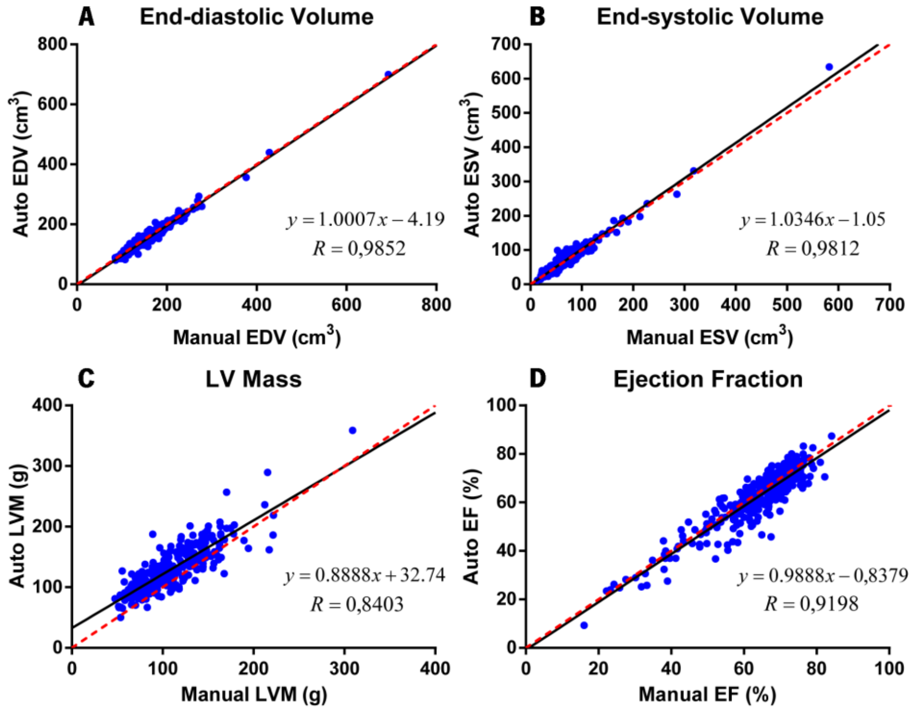

Figure 6.10 - Linear regression for (A) end-diastolic volume (EDV); (B) end-systolic volume (ESV); (C) left ventricular mass (LVM); and (D) ejection fraction (EF).

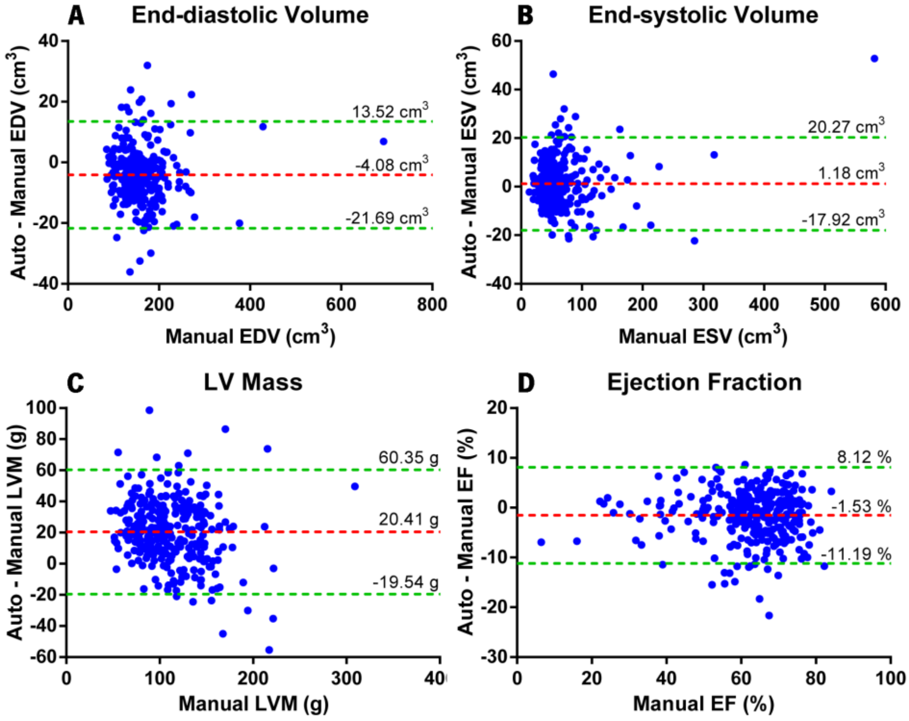

Figure 6.11 - Bland-Altman analysis for (A) end-diastolic volume (EDV); (B) end-systolic volume (ESV); left ventricular mass (LVM); and (D) ejection fraction (EF).

6.3 Discussion

6.3.1 Feasibility study

The proposed framework intends to provide a fully automatic segmentation of CMR datasets to be used in clinical practice. Understandably, its feasibility, and thus its ability to analyze a given dataset independent of the acquisition system, image quality or subject-specific anatomy and function, is one of the most crucial characteristic to be evaluated to understand the potential added value of such solution. In the large multi-center database used, the proposed framework achieved 95% feasibility, which is a high and, hence, extremely interesting result.

Concerning the 5% remaining datasets, it was found that the different initialization steps are the causes of such incorrect detection and/or delineation. Figure 6.2 allow us to understand some of the difficulties involved. When performing the LV localization algorithm, based on multilevel Otsu thresholding and search procedure, one of the fundamental assumptions is that the LV is (nearly) centered in the image. However, in the used database, the original images were cropped in the core lab for manual evaluation. In this process, the clinician was not concerned in centering the LV, which originated images with non-centered LV like the one in Figure 6.2A. This was one of the main causes of LV localization failure (4/7). Note that such cropping procedure also prevented a comprehensive evaluation of the robustness of the proposed LV localization method. Other causes for failure were related with sub-optimal image quality, including high heterogeneity inside blood pool and low contrast with myocardium. Importantly, if the correct object is manually chosen, the remaining segmentation is performed successfully in the majority of these cases.

Another cause for the analysis failure was associated with the proposed elliptical template matching procedure (5/318). In this situation, the main reason for incorrect object detection was related with the subject-specific anatomy and sub-optimal image quality. In fact, in 3 datasets, a thin myocardial wall in combination with low contrast between myocardium, lungs and surrounding tissues prevents a correct matching. Regarding the myocardial wall thickness, one should note that the proposed method assumes a constant thickness for the creation of the kernels. Therefore, it has a tendency to fit the template to the thinner part of the myocardial wall, disregarding the remaining thicker walls (which is the case of Figure 6.2B). The remaining datasets failed due to low contrast (1/5) or pronounced presence of papillary muscles (1/5).

Finally, the automatic stack initialization was also identified as one of the causes for failure (4/318), with the main reason related with extreme heterogeneities between slices at ED phase (see example in Figure 6.2C). Other possible causes were related with the pronounced presence of TPMs (or loose papillary muscles in the cavity, 1/4) and problems with basal slices when only approximately 50% of the cavity was surrounded by myocardium (1/4).

6.3.2 Segmentation Accuracy

The segmentation accuracy was assessed for the correctly initialized datasets (302/318) using both local and global tracking methods. Based on the results in Table 6.1, both methods presented accurate results, with OFT performing better for the endocardium and with comparable results for the epicardium.

Taking into account the results obtained for the MICCAI database [Table 4.3, Table 4.4], the endocardial results seem comparable, presenting similar average Dice metric, APD and Hausdorff distance for both OFT and BEASPM. In contrast, it seems that there is a difference in the epicardial results between the two databases. Nevertheless, one should note that in the current analysis both ED and ES phases were manually segmented, while in the MICCAI database only the endocardial contour was analyzed in the ES phase. Therefore, and based on the results for the 3D segmentation in the clinical trial database (data not shown), the observed decrease is related with the tracking stage and not with the proposed 3D BEAS segmentation. In this sense, it is possible to conclude that the presented algorithms track better the endocardium than the epicardium. Such conclusion is plausible as the interface between the LV cavity and the myocardium has higher contrast than the interface with the surrounding structures. In the OFT approach, higher contrast in the data (and so less data uncertainty) allows better estimation of the local motions, explaining the increased accuracy for the endocardium. On the other hand, BEASPM tries to find the best fitting between reference and target profiles, which fundamentally means higher robustness when more defined features (related with higher contrast) are present.

In a direct comparison between BEASPM and OFT, the latter seems to perform better. In a clinical setting, the quantification of the cardiac indices is paramount. Such parameters require the delineation of both contours in the ED phase and the endocardium in the ES phase. Therefore, the tracking algorithm affects directly the endocardial contour in the ES phase, and, consequently, the quantification of ESV, SV and EF. As aforementioned, OFT presented higher accuracy for the endocardial contour [Table 6.1], allowing one to conclude that it fits better the needs of clinical practice.

Figure 6.3 gives an overview of the proposed framework performance in segmenting a full dataset, with near 80% of the studied datasets with a Dice metric higher than 0.85 for both endo and epicardial contours. At the same time, these datasets also present an APD under 2.5 and 3.5 mm for both endocardial and epicardial contours, respectively, and a maximum local error around 6 - 7 mm. Regarding the errors distribution from basal to apical slices, the analysis of Figure 6.4 allow us to conclude that there is a tendency for higher errors in basal and apical slices, rather than in mid-ventricular ones (note the median and mean values). As stated in Section 5.3, this result is linked to the occurrence of poorly segmented slices at the two ends of the LV due to the LVOT in basal slices and to PVE in apical ones. Notwithstanding, overall the segmentation proved to be accurate and robust independently from the slice level, as concluded during the technical evaluation.

Such result is also confirmed by the examples in Figure 6.5. Yet, in the basal slice of the first dataset (A), it is clear the abovementioned sub-optimal accuracy in the LVOT. Note that the segmentation is quite accurate in terms of myocardial wall delineation, however the clinician tends to consider the septal portion as outflow tract and its volume is removed from the cavity. The proposed framework still not directly mimics this preference of the clinician, thus being responsible for a decrease in the global performance. Regarding the tracking robustness, Figure 6.6 and Figure 6.7 presented two example segmentations over the cardiac cycle in three different slice levels, showing accurate delineations. The overall aspect of the LV surface is also illustrated in Figure 6.8 and Figure 6.9. In these figures, the longitudinal contraction was taken into account based on the apical and basal slice levels and the common assumption of near incompressibility of the left ventricular myocardium (i.e., approximately constant mass) [137].

Overall, the current analysis allowed us to conclude that the segmentation accuracy observed in the technical evaluation was kept during the present clinical validation, even with the considerable amount of image quality, anatomy and function variability.

6.3.3 Clinical indices validation

In addition to the framework's feasibility and accuracy (in terms of Dice metric, APD and Hausdorff distance), the ability to automatically quantify the cardiac indices with comparable values to the physician is of utmost importance for success when introducing a methodology in daily clinical practice. In this sense, the correlation between manual and automatically calculated cardiac parameters was assessed [Table 6.2, Figure 6.10, Figure 6.11]. A high correlation for both volumetric measurements (i.e. EDV and ESV, 0.985 and 0.981, respectively) was obtained, resulting also in appealing correlations for stroke volume and ejection fraction (0.906 and 0.920, respectively). However, the values obtained were slightly lower than the ones found for the

MICCAI database. Notwithstanding, one should have in mind that the clinical trial database included a substantially higher number of datasets, with a broader range of variability in image characteristics and subjects' anatomy, which complicates the analysis and intrinsically demands for a generic approach. Regarding left ventricular mass, the correlation was lower, with wider limits of agreement [Figure 6.11C]. Such result is mainly related to the sub-optimal image quality and low contrast present in these datasets, but also due to the different edge selection approach employed by the core lab specialist.

Comparing to the recent study of Miller *et al.* [36] about the impact of "real-world" variability in the analysis methodologies used for manual contouring, our results present similar correlations to the ones reported. In fact, according to their study, the variability among physicians can reach correlations of about 0.93 to 0.99 for EDV and ESV or about 0.91 to 0.96 for EF, which shows the competitiveness of the proposed framework for automatic contouring. Globally, the results were promising for the distinct cardiac indices, reinforcing the potential of the proposed methodology for left ventricular morphology and global function assessment. In combination, the average computational time to segment a full 4D dataset (around 11s, with a MATLAB code) is exciting when compared to the manual analysis time (between 6 to 20min [29, 36, 37], for the ED and ES phases only), which may facilitate the introduction of the proposed framework in clinical practice. Actually, the current analysis time can even be sped up if the algorithm is implemented in C++ or on GPU, which ultimately shows that a one second analysis is highly feasible.

In summary, given that these results were obtained in a large multi-center database, with "real-world" clinical variability and subject to blinded core lab analysis, this is the most accurate picture of the potential performance of the algorithm in daily clinical practice. Thus, without a doubt, these results reassure the feasibility, accuracy, quality and robustness of the proposed framework for fast fully automatic 3D+time myocardial segmentation and global function assessment in daily clinical practice.

7. Main Conclusions

7. Main Conclusions

The present work aimed to develop a fast fully automatic 3D+time LV myocardial segmentation framework for CMR datasets with accurate shape delineation and low computational burden. To this extent, we proposed a novel framework presenting 3 conceptual blocks: 1) an automatic 2D mid-ventricular initialization and segmentation; 2) an automatic stack initialization followed by a 3D segmentation at the ED phase; and 3) a tracking procedure to delineate both endo and epicardial contours throughout the cardiac cycle. To this end, a fast automatic initialization approach capable of detecting LV elliptical annular shapes was presented through the combination of a LV localization method and an elliptical annular template matching algorithm. Moreover, an adapted version of the BEAS framework to CMR images is proposed for both 2D and 3D segmentations. In this sense, we integrated dedicated energy terms for accurate segmentation and we made use of a cylindrical coordinate system that better fits the topology of CMR data. An automatic stack initialization using a threshold-based BEAS formulation was also presented for 3D initialization and misalignment correction. Finally, and to propagate both contours over all cardiac phases, a local and a global tracking method, i.e. a profile matching based BEAS and global anatomical affine optical flow method, were presented and compared.

The proposed framework has been validated on 45 CMR datasets from a publicly available database and on 318 CMR datasets from an ongoing multi-center clinical trial. The framework showed competitive results against the state-of-the-art methods, presenting leading results in both accuracy and average computational time in the common database used for comparative purposes. Moreover, the results in the large scale clinical validation confirmed the high feasibility and robustness of the proposed framework for accurate left ventricular morphology and global function assessment. In combination with the low computational burden of the method, the current methodology seems promising to be used in daily clinical practice.

In the future, we intend to include the possibility of using LAX views (if acquired). Such solution would allow increasing the feasibility of the automatic initialization and the robustness of the tracking, by allowing LV base identification and tracking throughout the cardiac cycle. Moreover, we intend to include new terms in the proposed CMR-targeted energy, namely a shape-prior term, to further increase the robustness of the segmentation, particularly in the epicardial contour. In addition, and taking into account the increased accuracy of the OFT method, we intend to design a more localized optical flow tracking methodology to increase its accuracy while keeping the near real-time performance of the framework.

References

References

[1] S. S. Mader and P. Galliart, *Understanding human anatomy and physiology*, 5th ed. Boston: McGraw-Hill Higher Education, 2005.

[2] K. M. Van De Graaff, *Human anatomy*, 6th ed. Boston: McGraw-Hill, 2002.

[3] G. J. Tortora and B. Derrickson, *Principles of anatomy and physiology*, 12th ed. Hoboken, NJ: John Wiley & Sons, 2010.

[4] A. J. Vander, J. H. Sherman, and D. S. Luciano, *Human physiology : the mechanisms of body function*, 8th ed. Boston: McGraw-Hill, 2001.

[5] A. Despopoulos and S. Silbernagl, *Color atlas of physiology*, 6th ed. Stuttgart ; New York: Thieme, 2009.

[6] D. L. Longo and T. R. Harrison, *Harrison's principles of internal medicine*, 18th ed. New York: McGraw-Hill, 2012.

[7] World Health Organization, "Cardiovascular diseases," in *Fact sheet* vol. 317, ed, 2012.

[8] J. Mackay, G. A. Mensah, World Health Organization., and Centers for Disease Control and Prevention (U.S.), *The atlas of heart disease and stroke*. Geneva: World Health Organization, 2004.

[9] M. G. Khan, *Encyclopedia of heart diseases*: Academic Press, 2005.

[10] World Health Organization, "Global status report on noncommunicable diseases 2010," 2011.

[11] A. S. Go, D. Mozaffarian, V. L. Roger, E. J. Benjamin, J. D. Berry, W. B. Borden, D. M. Bravata, S. Dai, E. S. Ford, and C. S. Fox, "Heart Disease and Stroke Statistics—2013 Update. A Report From the American Heart Association," *Circulation,* vol. 127, pp. 143-152, 2013.

[12] M. Nichols, N. Townsend, P. Scarborough, R. Luengo-Fernandez, J. Leal, A. Gray, and M. Rayner, "European cardiovascular disease statistics 2012," *European Heart Network, Brussels, European Society of Cardiology, Sophia Antipolis,* p. P104, 2012.

[13] Centers for Disease Control and Prevention (U.S.). (2010, 1st July 2013). *National Hospital Discharge Survey*. Available: http://www.cdc.gov/nchs/fastats/insurg.htm

[14] World Health Organization, *World health statistics 2012*: World Health Organization, 2012.

[15] P. Leeson, *Cardiovascular imaging*: OUP Oxford, 2011.

[16] J. Bogaert, S. Dymarkowski, and A. M. Taylor, *Clinical Cardiac MRI*: Springer-Verlag Berlin Heidelberg, 2005.

[17] R. Y. Kwong, *Cardiovascular magnetic resonance imaging*: Springer, 2006.

[18] V. Dilsizian and G. M. Pohost, *Cardiac CT, PET and MR*: Wiley-Blackwell, 2011.

[19] P. Suetens, *Fundamentals of medical imaging*, 2nd ed.: Cambridge University Press, 2009.

[20] S. G. Myerson, J. Francis, and S. Neubauer, *Cardiovascular magnetic resonance*: Oxford University Press, 2010.

[21] E. Nicol, J. Stirrup, A. D. Kelion, and S. P. Padley, *Cardiovascular computed tomography*: OUP Oxford, 2011.

[22] J. L. Zamorano, *The ESC textbook of cardiovascular imaging*: Springer, 2010.

[23] E.-S. H. Ibrahim, "Imaging sequences in cardiovascular magnetic resonance: current role, evolving applications, and technical challenges," *The International Journal of Cardiovascular Imaging,* vol. 28, pp. 2027-2047, 2012.

[24] T. Karamitsos and S. Neubauer, "Cardiovascular magnetic resonance imaging," *Medicine,* vol. 38, pp. 384-389, 2010.

[25] D. J. Pennell, "Cardiovascular magnetic resonance," *Circulation,* vol. 121, pp. 692-705, 2010.

[26] F. Grothues, G. C. Smith, J. C. Moon, N. G. Bellenger, P. Collins, H. U. Klein, and D. J. Pennell, "Comparison of interstudy reproducibility of cardiovascular magnetic resonance with two-dimensional echocardiography in normal subjects and in patients with heart failure or left ventricular hypertrophy," *The American journal of cardiology,* vol. 90, pp. 29-34, 2002.

[27] C. A. Miller, K. Pearce, P. Jordan, R. Argyle, D. Clark, M. Stout, S. G. Ray, and M. Schmitt, "Comparison of real-time three-dimensional echocardiography with cardiovascular magnetic resonance for left ventricular volumetric assessment in unselected patients," *European Heart Journal–Cardiovascular Imaging,* vol. 13, pp. 187-195, 2012.

[28] A. F. Frangi, W. J. Niessen, and M. A. Viergever, "Three-dimensional modeling for functional analysis of cardiac images, a review," *Medical Imaging, IEEE Transactions on,* vol. 20, pp. 2-5, 2001.

[29] C. Petitjean and J. N. Dacher, "A review of segmentation methods in short axis cardiac MR images," *Medical image analysis,* vol. 15, pp. 169-184, 2011.

[30] R. O. Bonow, T. G. Ganiats, C. T. Beam, K. Blake, D. E. Casey, S. J. Goodlin, K. L. Grady, R. F. Hundley, M. Jessup, and T. E. Lynn, "ACCF/AHA/AMA-PCPI 2011 Performance Measures for Adults With Heart FailureA Report of the American College of Cardiology Foundation/American Heart Association Task Force on Performance Measures and the American Medical Association–Physician Consortium for Performance Improvement," *Journal of the American College of Cardiology,* vol. 59, pp. 1812-1832, 2012.

[31] W. G. Hundley, D. A. Bluemke, J. P. Finn, S. D. Flamm, M. A. Fogel, M. G. Friedrich, V. B. Ho, M. Jerosch-Herold, C. M. Kramer, and W. J. Manning, "ACCF/ACR/AHA/NASCI/SCMR 2010 Expert Consensus Document on Cardiovascular Magnetic Resonance A Report of the American College of Cardiology Foundation Task Force on Expert Consensus Documents," *Circulation,* vol. 121, p. 2462, 2010.

[32] P. Pibarot, É. Larose, and J. Dumesnil, "Imaging of Valvular Heart Disease," *Canadian Journal of Cardiology,* 2013.

[33] S. Yamada, H. Ishii, H. Takahashi, T. Aoyama, Y. Morita, H. Kasuga, K. Kimura, Y. Ito, R. Takahashi, and T. Toriyama, "Prognostic value of reduced left ventricular ejection fraction at start of hemodialysis therapy on cardiovascular and all-cause mortality in end-stage renal disease patients," *Clinical Journal of the American Society of Nephrology,* vol. 5, pp. 1793-1798, 2010.

[34] J. K. Ghali, Y. Liao, B. Simmons, A. Castaner, G. Cao, and R. S. Cooper, "The prognostic role of left ventricular hypertrophy in patients with or without coronary artery disease," *Annals of internal medicine,* vol. 117, pp. 831-836, 1992.

[35] J. Anderson, A. N. Weaver, B. D. Horne, H. U. Jones, G. K. Jelaco, J. A. Cha, H. E. Busto, J. Hall, K. Walker, and D. D. Blatter, "Normal cardiac magnetic resonance measurements and interobserver discrepancies in volumes and mass using the papillary muscle inclusion method," *The Open General and Internal Medicine Journal,* vol. 1, pp. 6-12, 2007.

[36] C. A. Miller, P. Jordan, A. Borg, R. Argyle, D. Clark, K. Pearce, and M. Schmitt, "Quantification of left ventricular indices from SSFP cine imaging: Impact of real-world variability in analysis methodology and utility of geometric modeling," *Journal of Magnetic Resonance Imaging,* 2012.

[37] G. L. Hautvast, C. J. Salton, M. L. Chuang, M. Breeuwer, C. J. O'Donnell, and W. J. Manning, "Accurate computer-aided quantification of left ventricular parameters:

Experience in 1555 cardiac magnetic resonance studies from the Framingham Heart Study," *Magnetic Resonance in Medicine,* vol. 67, pp. 1478-1486, 2012.

[38] L. Cordero-Grande, G. Vegas-Sánchez-Ferrero, P. Casaseca-de-la-Higuera, J. Alberto San-Román-Calvar, A. Revilla-Orodea, M. Martín-Fernández, and C. Alberola-López, "Unsupervised 4D myocardium segmentation with a Markov Random Field based deformable model," *Medical image analysis,* vol. 15, pp. 283-301, 2011.

[39] A. M. Sigmund, A. Usman, M. Wasielewski, A. R. Akhavan, S. Giri, M. A. Stratton, J. Collins, and J. Carr, "Semi-automatic inline calculation of left ventricular function using cardiac MRI (CMR)," *Journal of Cardiovascular Magnetic Resonance,* vol. 15, p. P80, 2013.

[40] M. Wasielewski, A. A. Usman, P. J. Weale, and J. Carr, "Manual verses automatic inline ventricular function assessment using MRI," *Journal of Cardiovascular Magnetic Resonance,* vol. 13, p. P354, 2011.

[41] A. Eslami, A. Karamalis, A. Katouzian, and N. Navab, "Segmentation by retrieval with guided random walks: Application to left ventricle segmentation in MRI," *Medical image analysis,* 2012.

[42] I. Ben Ayed, H.-m. Chen, K. Punithakumar, I. Ross, and S. Li, "Max-flow segmentation of the left ventricle by recovering subject-specific distributions via a bound of the Bhattacharyya measure," *Medical image analysis,* vol. 16, pp. 87-100, 2012.

[43] H. Hu, H. Liu, Z. Gao, and L. Huang, "Hybrid segmentation of left ventricle in cardiac MRI using gaussian-mixture model and region restricted dynamic programming," *Magnetic resonance imaging,* 2012.

[44] H. Liu, H. Hu, X. Xu, and E. Song, "Automatic Left Ventricle Segmentation in Cardiac MRI Using Topological Stable-State Thresholding and Region Restricted Dynamic Programming," *Academic Radiology,* 2012.

[45] C. Constantinides, E. Roullot, M. Lefort, and F. Frouin, "Fully automated segmentation of the left ventricle applied to cine MR images: Description and results on a database of 45 Subjects," in *Engineering in Medicine and Biology Society (EMBC), 2012 Annual International Conference of the IEEE*, 2012, pp. 3207-3210.

[46] J. Ulén, P. Strandmark, and F. Kahl, "An Efficient Optimization Framework for Multi-Region Segmentation based on Lagrangian Duality," 2012.

[47] D. Barbosa, T. Dietenbeck, J. Schaerer, J. D'hooge, D. Friboulet, and O. Bernard, "B-Spline Explicit Active Surfaces: An Efficient Framework for Real-Time 3-D Region-Based Segmentation," *Image Processing, IEEE Transactions on,* vol. 21, pp. 241-251, 2012.

[48] V. A. Hegde, J. R. Mikolich, M. Doyle, V. K. Rathi, J. A. Yamrozik, R. B. Williams, and R. Biederman, "Cardiac magnetic resonance imaging in today's economic climate; a cost effectiveness analysis," *Journal of Cardiovascular Magnetic Resonance,* vol. 13, p. M12, 2011.

[49] D. J. Pennell, U. P. Sechtem, C. B. Higgins, W. J. Manning, G. M. Pohost, F. E. Rademakers, A. C. van Rossum, L. J. Shaw, and E. K. Yucel, "Clinical indications for cardiovascular magnetic resonance (CMR): Consensus Panel report," *European heart journal,* vol. 25, pp. 1940-1965, 2004.

[50] K. Alfakih, S. Plein, H. Thiele, T. Jones, J. P. Ridgway, and M. U. Sivananthan, "Normal human left and right ventricular dimensions for MRI as assessed by turbo gradient echo and steady-state free precession imaging sequences," *Journal of Magnetic Resonance Imaging,* vol. 17, pp. 323-329, 2003.

[51] S. Clay, K. Alfakih, A. Radjenovic, T. Jones, and J. P. Ridgway, "Normal range of human left ventricular volumes and mass using steady state free precession MRI in the radial long

axis orientation," *Magnetic Resonance Materials in Physics, Biology and Medicine,* vol. 19, pp. 41-45, 2006.

[52] A. Maceira, S. Prasad, M. Khan, and D. Pennell, "Normalized left ventricular systolic and diastolic function by steady state free precession cardiovascular magnetic resonance," *Journal of Cardiovascular Magnetic Resonance,* vol. 8, pp. 417-426, 2006.

[53] J. C. Moon, C. H. Lorenz, J. M. Francis, G. C. Smith, and D. J. Pennell, "Breath-hold FLASH and FISP Cardiovascular MR Imaging: Left Ventricular Volume Differences and Reproducibility1," *Radiology,* vol. 223, pp. 789-797, 2002.

[54] L. Sugeng, V. Mor-Avi, L. Weinert, J. Niel, C. Ebner, R. Steringer-Mascherbauer, F. Schmidt, C. Galuschky, G. Schummers, and R. M. Lang, "Quantitative Assessment of Left Ventricular Size and Function Side-by-Side Comparison of Real-Time Three-Dimensional Echocardiography and Computed Tomography With Magnetic Resonance Reference," *Circulation,* vol. 114, pp. 654-661, 2006.

[55] J. Gutteling, L. Theunissen, and P. Wijn, "Comparison of Cardiac MR and 3D Echocardiography Left Ventricular Analysis," in *World Congress on Medical Physics and Biomedical Engineering, September 7-12, 2009, Munich, Germany*, 2009, pp. 50-52.

[56] A. Bailly, J. Lipiecki, P. Chabrot, A. Alfidja, J. Garcier, S. Ughetto, J. Ponsonnaille, and L. Boyer, "Assessment of left ventricular volumes and function by cine-MR imaging depending on the investigator's experience," *Surgical and radiologic anatomy,* vol. 31, pp. 113-120, 2009.

[57] S. E. Luijnenburg, D. Robbers-Visser, A. Moelker, H. W. Vliegen, B. J. Mulder, and W. A. Helbing, "Intra-observer and interobserver variability of biventricular function, volumes and mass in patients with congenital heart disease measured by CMR imaging," *The International Journal of Cardiovascular Imaging,* vol. 26, pp. 57-64, 2010.

[58] P. Berkovic, M. Hemmink, P. M. Parizel, C. J. Vrints, and B. P. Paelinck, "MR image analysis: Longitudinal cardiac motion influences left ventricular measurements," *European journal of radiology,* vol. 73, pp. 260-265, 2010.

[59] T. Papavassiliu, H. P. Kühl, M. Schröder, T. Süselbeck, O. Bondarenko, C. K. Böhm, A. Beek, M. M. Hofman, and A. C. van Rossum, "Effect of endocardial trabeculae on left ventricular measurements and measurement reproducibility at cardiovascular MR imaging1," *Radiology,* vol. 236, pp. 57-64, 2005.

[60] M. C. Hogan, S. E. Petersen, L. E. Hudsmith, J. M. Francis, S. Neubauer, and M. D. Robson, "Effects of steady state free precession parameters on cardiac mass, function, and volumes," *The International Journal of Cardiovascular Imaging,* vol. 23, pp. 583-589, 2007.

[61] M. L. Chuang, P. Gona, G. L. Hautvast, C. J. Salton, S. J. Blease, S. B. Yeon, M. Breeuwer, C. J. O'Donnell, and W. J. Manning, "Impact of left ventricular trabeculations and papillary muscles on measures of cavity volume and ejection fraction," *Journal of Cardiovascular Magnetic Resonance,* vol. 13, p. P36, 2011.

[62] M. Lynch, O. Ghita, and P. F. Whelan, "Segmentation of the left ventricle of the heart in 3-D+ t MRI data using an optimized nonrigid temporal model," *Medical Imaging, IEEE Transactions on,* vol. 27, pp. 195-203, 2008.

[63] T. Chen, J. Babb, P. Kellman, L. Axel, and D. Kim, "Semiautomated segmentation of myocardial contours for fast strain analysis in cine displacement-encoded MRI," *Medical Imaging, IEEE Transactions on,* vol. 27, pp. 1084-1094, 2008.

[64] I. Ben Ayed, S. Li, and I. Ross, "Embedding overlap priors in variational left ventricle tracking," *Medical Imaging, IEEE Transactions on,* vol. 28, pp. 1902-1913, 2009.

[65] A. Goshtasby and D. A. Turner, "Segmentation of cardiac cine MR images for extraction of right and left ventricular chambers," *Medical Imaging, IEEE Transactions on,* vol. 14, pp. 56-64, 1995.

[66] S. Huang, J. Liu, L. C. Lee, S. K. Venkatesh, L. L. San Teo, C. Au, and W. L. Nowinski, "An image-based comprehensive approach for automatic segmentation of left ventricle from cardiac short axis cine mr images," *Journal of Digital Imaging,* vol. 24, pp. 598-608, 2011.

[67] Y. Lu, P. Radau, K. Connelly, A. Dick, and G. A. Wright, "Segmentation of left ventricle in cardiac cine MRI: An automatic image-driven method," in *Functional Imaging and Modeling of the Heart*, ed: Springer, 2009, pp. 339-347.

[68] R. Van der Geest, E. Jansen, V. Buller, and J. Reiber, "Automated detection of left ventricular epi-and endocardial contours in short-axis MR images," in *Computers in Cardiology 1994*, 1994, pp. 33-36.

[69] D. T. Gering, "Automatic segmentation of cardiac MRI," in *Medical Image Computing and Computer-Assisted Intervention-MICCAI 2003*, ed: Springer, 2003, pp. 524-532.

[70] A. Pednekar, U. Kurkure, R. Muthupillai, S. Flamm, and I. A. Kakadiaris, "Automated left ventricular segmentation in cardiac MRI," *Biomedical Engineering, IEEE Transactions on,* vol. 53, pp. 1425-1428, 2006.

[71] X. Wang, Q. Hu, and P. A. Heng, "Left ventricle segmentation with mixture of Gaussian active contours," in *Biomedical Imaging (ISBI), 2012 9th IEEE International Symposium on*, 2012, pp. 230-233.

[72] C. A. Cocosco, W. J. Niessen, T. Netsch, E. j. Vonken, G. Lund, A. Stork, and M. A. Viergever, "Automatic image-driven segmentation of the ventricles in cardiac cine MRI," *Journal of Magnetic Resonance Imaging,* vol. 28, pp. 366-374, 2008.

[73] M. Lynch, O. Ghita, and P. F. Whelan, "Automatic segmentation of the left ventricle cavity and myocardium in MRI data," *Computers in Biology and Medicine,* vol. 36, pp. 389-407, 2006.

[74] N. Paragios and R. Deriche, "Geodesic active regions and level set methods for supervised texture segmentation," *International journal of computer vision,* vol. 46, pp. 223-247, 2002.

[75] C. Li, X. Jia, and Y. Sun, "Improved semi-automated segmentation of cardiac CT and MR images," in *Biomedical Imaging: From Nano to Macro, 2009. ISBI'09. IEEE International Symposium on*, 2009, pp. 25-28.

[76] C. Pluempitiwiriyawej, J. M. Moura, Y.-J. L. Wu, and C. Ho, "STACS: New active contour scheme for cardiac MR image segmentation," *Medical Imaging, IEEE Transactions on,* vol. 24, pp. 593-603, 2005.

[77] J. Woo, P. J. Slomka, C.-C. Jay Kuo, and B.-W. Hong, "Multiphase Segmentation using an Implicit Dual Shape Prior: Application to Detection of Left Ventricle in Cardiac MRI," *Computer vision and image understanding,* 2013.

[78] C. Constantinides, Y. Chenoune, N. Kachenoura, E. Roullot, E. Mousseaux, A. Herment, and F. Frouin, "Semi-automated cardiac segmentation on cine magnetic resonance images using GVF-Snake deformable models," *The MIDAS Journal-Cardiac MR Left Ventricle Segmentation Challenge,* 2009.

[79] R. El Berbari, I. Bloch, A. Redheuil, E. Angelini, E. Mousseaux, F. Frouin, and A. Herment, "An automated myocardial segmentation in cardiac MRI," in *Engineering in Medicine and Biology Society, 2007. EMBS 2007. 29th Annual International Conference of the IEEE*, 2007, pp. 4508-4511.

[80] G. Hautvast, S. Lobregt, M. Breeuwer, and F. Gerritsen, "Automatic contour propagation in cine cardiac magnetic resonance images," *Medical Imaging, IEEE Transactions on,* vol. 25, pp. 1472-1482, 2006.

[81] X. Papademetris, A. J. Sinusas, D. P. Dione, R. T. Constable, and J. S. Duncan, "Estimation of 3-D left ventricular deformation from medical images using biomechanical models," *Medical Imaging, IEEE Transactions on,* vol. 21, pp. 786-800, 2002.

[82] Q. Pham, F. Vincent, P. Clarysse, P. Croisille, and I. Magnin, "A FEM-based deformable model for the 3D segmentation and tracking of the heart in cardiac MRI," in *Image and Signal Processing and Analysis, 2001. ISPA 2001. Proceedings of the 2nd International Symposium on*, 2001, pp. 250-254.

[83] M. Sermesant, C. Forest, X. Pennec, H. Delingette, and N. Ayache, "Deformable biomechanical models: Application to 4D cardiac image analysis," *Medical image analysis,* vol. 7, pp. 475-488, 2003.

[84] N. Paragios, M. Rousson, and V. Ramesh, "Knowledge-based registration & segmentation of the left ventricle: A level set approach," in *Applications of Computer Vision, 2002.(WACV 2002). Proceedings. Sixth IEEE Workshop on*, 2002, pp. 37-42.

[85] S. C. Mitchell, J. G. Bosch, B. P. F. Lelieveldt, R. J. van der Geest, J. H. C. Reiber, and M. Sonka, "3-D active appearance models: segmentation of cardiac MR and ultrasound images," *Medical Imaging, IEEE Transactions on,* vol. 21, pp. 1167-1178, 2002.

[86] H. C. Van Assen, M. G. Danilouchkine, A. F. Frangi, S. n. Ord s, J. J. Westenberg, J. H. Reiber, and B. P. Lelieveldt, "SPASM: a 3D-ASM for segmentation of sparse and arbitrarily oriented cardiac MRI data," *Medical image analysis,* vol. 10, pp. 286-303, 2006.

[87] S. C. Mitchell, B. P. F. Lelieveldt, R. J. van der Geest, H. G. Bosch, J. Reiver, and M. Sonka, "Multistage hybrid active appearance model matching: segmentation of left and right ventricles in cardiac MR images," *Medical Imaging, IEEE Transactions on,* vol. 20, pp. 415-423, 2001.

[88] H. Zhang, A. Wahle, R. K. Johnson, T. D. Scholz, and M. Sonka, "4-D cardiac MR image analysis: left and right ventricular morphology and function," *Medical Imaging, IEEE Transactions on,* vol. 29, pp. 350-364, 2010.

[89] B. P. Lelieveldt, R. J. van der Geest, J. H. Reiber, J. G. Bosch, S. C. Mitchell, and M. Sonka, "Time-continuous segmentation of cardiac image sequences using active appearance motion models," in *Information Processing in Medical Imaging*, 2001, pp. 446-452.

[90] M. Lorenzo-Valdés, G. I. Sanchez-Ortiz, R. Mohiaddin, and D. Rueckert, "Atlas-based segmentation and tracking of 3D cardiac MR images using non-rigid registration," in *Medical Image Computing and Computer-Assisted Intervention—MICCAI 2002*, ed: Springer, 2002, pp. 642-650.

[91] X. Zhuang, K. Rhode, S. Arridge, R. Razavi, D. Hill, D. Hawkes, and S. Ourselin, "An atlas-based segmentation propagation framework using locally affine registration–application to automatic whole heart segmentation," in *Medical Image Computing and Computer-Assisted Intervention–MICCAI 2008*, ed: Springer, 2008, pp. 425-433.

[92] X. Zhuang, K. S. Rhode, R. S. Razavi, D. J. Hawkes, and S. Ourselin, "A registration-based propagation framework for automatic whole heart segmentation of cardiac MRI," *Medical Imaging, IEEE Transactions on,* vol. 29, pp. 1612-1625, 2010.

[93] J. Cousty, L. Najman, M. Couprie, S. Clément-Guinaudeau, T. Goissen, and J. Garot, "Segmentation of 4D cardiac MRI: Automated method based on spatio-temporal watershed cuts," *Image and Vision Computing,* vol. 28, pp. 1229-1243, 2010.

[94] A. P. Dempster, N. M. Laird, and D. B. Rubin, "Maximum likelihood from incomplete data via the EM algorithm," *Journal of the Royal Statistical Society. Series B (Methodological),* pp. 1-38, 1977.

[95] M. Kass, A. Witkin, and D. Terzopoulos, "Snakes: Active contour models," *International journal of computer vision,* vol. 1, pp. 321-331, 1988.

[96] S. Osher and J. A. Sethian, "Fronts propagating with curvature-dependent speed: algorithms based on Hamilton-Jacobi formulations," *Journal of computational physics,* vol. 79, pp. 12-49, 1988.

[97] V. Caselles, F. Catté, T. Coll, and F. Dibos, "A geometric model for active contours in image processing," *Numerische mathematik,* vol. 66, pp. 1-31, 1993.

[98] S. Lankton and A. Tannenbaum, "Localizing region-based active contours," *Image Processing, IEEE Transactions on,* vol. 17, pp. 2029-2039, 2008.

[99] C. Xu and J. L. Prince, "Snakes, shapes, and gradient vector flow," *Image Processing, IEEE Transactions on,* vol. 7, pp. 359-369, 1998.

[100] T. F. Cootes, C. J. Taylor, D. H. Cooper, and J. Graham, "Active shape models-their training and application," *Computer vision and image understanding,* vol. 61, pp. 38-59, 1995.

[101] T. F. Cootes, G. J. Edwards, and C. J. Taylor, "Active appearance models," in *Computer Vision—ECCV'98*, ed: Springer, 1998, pp. 484-498.

[102] M. M. Hadhoud, M. I. Eladawy, and A. Farag, "Region of Interest Localization of Cardiac Structure from Cine MRI Images," in *Information Technology: New Generations (ITNG), 2012 Ninth International Conference on*, 2012, pp. 14-17.

[103] J. Huang, X. Huang, D. Metaxas, and L. Axel, "Dynamic texture based heart localization and segmentation in 4-d cardiac images," in *Biomedical Imaging: From Nano to Macro, 2007. ISBI 2007. 4th IEEE International Symposium on*, 2007, pp. 852-855.

[104] J. Ringenberg, M. Deo, V. Devabhaktuni, D. Filgueiras-Rama, G. Pizarro, B. Ibañez, O. Berenfeld, P. Boyers, and J. Gold, "Automated segmentation and reconstruction of patient-specific cardiac anatomy and pathology from in vivo MRI," *Measurement Science and Technology,* vol. 23, p. 125405, 2012.

[105] C. A. Cocosco, T. Netsch, J. Sénégas, D. Bystrov, W. J. Niessen, and M. A. Viergever, "Automatic cardiac region-of-interest computation in cine 3D structural MRI," in *International Congress Series*, 2004, pp. 1126-1131.

[106] C. Constantinides, Y. Chenoune, E. Mousseaux, E. Roullot, and F. Frouin, "Automated heart localization for the segmentation of the ventricular cavities on cine magnetic resonance images," in *Computing in Cardiology, 2010*, 2010, pp. 911-914.

[107] X. Lin, B. R. Cowan, and A. A. Young, "Automated detection of left ventricle in 4D MR images: experience from a large study," in *Medical Image Computing and Computer-Assisted Intervention–MICCAI 2006*, ed: Springer, 2006, pp. 728-735.

[108] L. Tautz, O. Friman, A. Hennemuth, A. Seeger, and H.-O. Peitgen, "Automatic Detection of a Heart ROI in Perfusion MRI Images," in *Bildverarbeitung für die Medizin 2011*, ed: Springer, 2011, pp. 259-263.

[109] R. J. Van der Geest, V. G. Buller, E. Jansen, H. J. Lamb, L. H. Baur, E. E. van der Wall, A. de Roos, and J. H. Reiber, "Comparison between manual and semiautomated analysis of left ventricular volume parameters from short-axis MR images," *Journal of computer assisted tomography,* vol. 21, pp. 756-765, 1997.

[110] C. Ciofolo, M. Fradkin, B. Mory, G. Hautvast, and M. Breeuwer, "Automatic myocardium segmentation in late-enhancement MRI," in *Biomedical Imaging: From Nano to Macro, 2008. ISBI 2008. 5th IEEE International Symposium on*, 2008, pp. 225-228.

[111] J. E. McManigle, R. V. Stebbing, and J. A. Noble, "Modified Hough transform for left ventricle myocardium segmentation in 3-D echocardiogram images," in *Biomedical Imaging (ISBI), 2012 9th IEEE International Symposium on*, 2012, pp. 290-293.

[112] O. Bernard, D. Friboulet, P. Thévenaz, and M. Unser, "Variational B-spline level-set: a linear filtering approach for fast deformable model evolution," *Image Processing, IEEE Transactions on,* vol. 18, pp. 1179-1191, 2009.

[113] Q. Duan, E. D. Angelini, and A. F. Laine, "Real-time segmentation by active geometric functions," *Computer methods and programs in biomedicine,* vol. 98, pp. 223-230, 2010.

[114] S. Osher and R. Fedkiw, *Level set methods and dynamic implicit surfaces* vol. 153: Springer, 2003.

[115] S. Osher and N. Paragios, *Geometric level set methods in imaging, vision, and graphics*: Springer, 2003.

[116] T. F. Chan and L. A. Vese, "Active contours without edges," *Image Processing, IEEE Transactions on,* vol. 10, pp. 266-277, 2001.

[117] N. Otsu, "A threshold selection method from gray-level histograms," *Automatica,* vol. 11, pp. 23-27, 1975.

[118] D. Barbosa, O. Bernard, O. Savu, T. Dietenbeck, B. Heyde, P. Claus, D. Friboulet, and J. D'hooge, "Coupled B-spline active geometric functions for myocardial segmentation: A localized region-based approach," in *Ultrasonics Symposium (IUS), 2010 IEEE*, 2010, pp. 1648-1651.

[119] Y. Shi and W. C. Karl, "A real-time algorithm for the approximation of level-set-based curve evolution," *Image Processing, IEEE Transactions on,* vol. 17, pp. 645-656, 2008.

[120] H.-Y. Lee, N. C. Codella, M. D. Cham, J. W. Weinsaft, and Y. Wang, "Automatic left ventricle segmentation using iterative thresholding and an active contour model with adaptation on short-axis cardiac MRI," *Biomedical Engineering, IEEE Transactions on,* vol. 57, pp. 905-913, 2010.

[121] J. Canny, "A computational approach to edge detection," *Pattern Analysis and Machine Intelligence, IEEE Transactions on,* pp. 679-698, 1986.

[122] L. D. Cohen and I. Cohen, "Finite-element methods for active contour models and balloons for 2-D and 3-D images," *Pattern Analysis and Machine Intelligence, IEEE Transactions on,* vol. 15, pp. 1131-1147, 1993.

[123] D. Barbosa, B. Heyde, T. Dietenbeck, D. Friboulet, J. D'hooge, and O. Bernard, "Fast left ventricle tracking in 3D echocardiographic data using anatomical affine optical flow," in *Functional Imaging and Modeling of the Heart (FIMH2013)*, 2013, pp. 191-199.

[124] L. Spreeuwers and M. Breeuwer, "Detection of left ventricular epi-and endocardial borders using coupled active contours," in *International Congress Series*, 2003, pp. 1147-1152.

[125] A. Elen, J. Hermans, H. Hermans, F. Maes, and P. Suetens, "A 3d+ time spatio-temporal model for joint segmentation and registration of sparse cardiac cine MR image stacks," in *Statistical Atlases and Computational Models of the Heart. Imaging and Modelling Challenges*, ed: Springer, 2012, pp. 198-206.

[126] J.-Y. Bouguet, "Pyramidal implementation of the affine lucas kanade feature tracker description of the algorithm," *Intel Corporation,* 2001.

[127] B. D. Lucas and T. Kanade, "An iterative image registration technique with an application to stereo vision," in *Proceedings of the 7th international joint conference on Artificial intelligence*, 1981.

[128] P. Radau, Y. Lu, K. Connelly, G. Paul, A. Dick, and G. Wright, "Evaluation framework for algorithms segmenting short axis cardiac MRI," *MIDAS J.—Cardiac MR Left Ventricle Segmentation Challenge,* 2009.

[129] D. G. Altman and J. M. Bland, "Measurement in medicine: the analysis of method comparison studies," *The statistician,* pp. 307-317, 1983.

[130] M. Jolly, "Fully automatic left ventricle segmentation in cardiac cine mr images using registration and minimum surfaces," in *MICCAI 2009 Workshop on Cardiac MR Left Ventricle Segmentation Challenge. MIDAS Journal*, 2009.

[131] J. Schaerer, C. Casta, J. Pousin, and P. Clarysse, "A dynamic elastic model for segmentation and tracking of the heart in MR image sequences," *Medical image analysis,* vol. 14, pp. 738-749, 2010.

[132] M. G. Uzunbas, S. Zhang, K. M. Pohl, D. Metaxas, and L. Axel, "Segmentation of myocardium using deformable regions and graph cuts," in *Biomedical Imaging (ISBI), 2012 9th IEEE International Symposium on*, 2012, pp. 254-257.

[133] J. Wijnhout, D. Hendriksen, H. Assen, and R. der Geest, "LV challenge LKEB contribution: Fully automated myocardial contour detection," *The MIDAS Journal,* vol. 43, 2009.

[134] M. Hüllebrand, A. Hennemuth, D. Messroghli, T. Kühne, and O. Friman, "Semi-Automatic 4D Fuzzy Connectedness Segmentation of Heart Ventricles in Cine MRI," in *Bildverarbeitung für die Medizin 2011*, ed: Springer, 2011, pp. 3-7.

[135] L. Marak, J. Cousty, L. Najman, and H. Talbot, "4D Morphological segmentation and the MICCAI LV-segmentation grand challenge," in *MICCAI 2009 Workshop on Cardiac MR Left Ventricle Segmentation Challenge*, 2009, pp. 1-8.

[136] S. O'Brien, O. Ghita, and P. Whelan, "Segmenting the left ventricle in 3D using a coupled ASM and a learned non-rigid spatial model," *The MIDAS Journal,* vol. 49, 2009.

[137] K. Tsuiki and E. L. Ritman, "Direct evidence that left ventricular myocardium is incompressible throughout systole and diastole," *The Tohoku journal of experimental medicine,* vol. 132, p. 119, 1980.

Appendixes

Appendixes

Appendix A: Combined global and local region-based energy

In Section 3.3, a CMR-targeted energy was proposed based on a weighted region-based energy functional with two different energies for the endocardium and epicardium. On the one hand, a signed localized Yezzi (SLY) energy was proposed for the endocardium, taking advantage of the known relative signal intensity of the cavity and myocardium. On the other hand, an unsigned localized Chan-Vese energy (LCV) was used for the epicardium, based on the low contrast between cardiac muscle and surrounding tissues and their relative homogeneity.

In this appendix, a new energy feature is presented, which explicitly takes advantage of the myocardial region homogeneity in mid-ventricular slices. The strategy (henceforward referred as myoGL) is to combine global and local principles for the computation of local statistics in the myocardium. This method is only applied to the myocardial region as it is the only one with fair homogeneity in mid-ventricular slices. The presence of TPMs and heterogeneities due to blood flow in the cavity and the diversity of structures adjacent to the LV (lungs, RV, pericardium and abdominal organs) prevent global modeling of the inner and outer regions, respectively.

Based on the proposed energy for 2D segmentation (equations (3.6) to (3.10)), the proposed strategy requires a new equation for the computation of the mean intensity of the myocardial region, which is now given by $u_{gl,myo} = (u_{x,myo} + u_{g,myo})/2$. Note $u_{x,myo}$ as the local mean intensity of the myocardial region (as used previously) and $u_{g,myo}$ as the global mean intensity estimated using the entire myocardium. The latter tries to introduce a global term in the energy formulation, in order to overcome possible initialization problems and thus increasing the methods' robustness.

With the aim of evaluating the proposed energy feature, the segmentation performance was assessed in the 41 mid-ventricular SAX images considered in Section 4.4. Again, for comparative purposes, a non-weighted localized Chan-Vese energy [98] applied for both boundaries is used as benchmark. At the same time, we also intend to study the influence of the added weights, as well as the different energies considered for the two contours. Table A.1 presents the segmentation accuracy (using the automatic initialization) for different combinations of features in the proposed energy functional. A paired t-test was performed to assess if there was a statistical difference between the combinations tested (always between a given combination and the previous ones).

Table A.1 - 2D Segmentation performance for endo and epicardium with multiple combinations of the proposed features in the energy functional (# = 41, $\mu \pm \sigma$).

	Energy	w_i	myoGL	**Dice**		**APD** (mm)		**Hausdorff** (mm)	
				Endo	**Epi**	**Endo**	**Epi**	**Endo**	**Epi**
A	LCV	1.0	No	0.90 ± 0.07	0.92 ± 0.03	2.51 ± 1.61	2.83 ± 1.19	5.85 ± 3.17	6.82 ± 2.86
B	LCV	0.3	No	$0.93 \pm 0.05^{\ddagger}$	$0.94 \pm 0.03^{\ddagger}$	$1.81 \pm 1.19^{\ddagger}$	$2.13 \pm 0.91^{\ddagger}$	$4.55 \pm 2.86^{\ddagger}$	$5.53 \pm 2.70^{\ddagger}$
C	SLY/LCV	0.3	No	$0.93 \pm 0.05^{\ddagger}$	$0.94 \pm 0.03^{\ddagger}$	$1.91 \pm 1.36^{\ddagger}$	$2.21 \pm 0.95^{\ddagger}$	$5.19 \pm 3.56^{\ddagger\dagger}$	$5.81 \pm 2.93^{\ddagger}$
D	LCV	0.3	Yes	$0.94 \pm 0.04^{\ddagger}$	$0.94 \pm 0.02^{\ddagger}$	$1.68 \pm 0.98^{\ddagger}$	$1.90 \pm 0.76^{\ddagger\dagger *}$	$4.37 \pm 2.92^{\ddagger *}$	$4.99 \pm 2.62^{\ddagger\dagger *}$
E	SLY/LCV	0.3	Yes	$0.94 \pm 0.04^{\ddagger *}$	$0.94 \pm 0.02^{\ddagger\dagger *}$	$1.60 \pm 1.05^{\ddagger *}$	$1.96 \pm 0.74^{\ddagger\dagger *}$	$4.20 \pm 2.61^{\ddagger *}$	$5.07 \pm 2.47^{\ddagger\dagger *}$

‡ $p < 0.05$, paired t-test against A.
† $p < 0.05$, paired t-test against B.
* $p < 0.05$, paired t-test against C.
No significant difference was found against D.

The analysis of Table A.1 allow us to conclude that any of the features introduced lead to a statistical increase of the accuracy when compared to the benchmark energy (note the result of the paired t-test against A for cases B to E). Moreover, it is also possible to conclude that the weighted formulation was responsible for the largest improvement. Regarding the localized energies used, there is no significant difference for both Dice and APD for the 2D segmentation in the proposed energy (C against B and E against D). However, a significant improvement was observed in the 3D segmentation (Appendix B), which proves the added value of using the SLY energy to take advantage of the known relative intensity between cavity and cardiac muscle. Concerning the presented combined local and global formulation for the myocardial region, one is able to observe a significant improvement for the epicardial contour and a tendency for higher accuracy for the endocardium. However, as stated in Section 4.4, such result was not observed for the 3D segmentation (data not shown), due to partial volume effects in apical slices and low contrast between myocardium and surrounding structures. Thus, and for consistency, this strategy was also removed in the 2D segmentation.

In summary, the present analysis shows the importance of designing an energy specific for CMR images, taking advantage of the *a priori* knowledge about these images. The proposed energy has proven to be superior to the benchmark energy, increasing the segmentation accuracy and the robustness against initialization.

Appendix B: Influence of energy features in 3D segmentation accuracy

In order to improve the segmentation accuracy in the proposed 3D BEAS segmentation, we presented a hybrid energy functional for the epicardium, by adding to our previous 2D epicardial energy an edge-based term. The main purpose was to address the problem of local minima close to the epicardial boundary, as well as to minimize the effect of low contrast in the segmentation performance. Nonetheless, the advantage of such strategy was still not properly evaluated. Moreover, the reason behind a hybrid energy (instead of a pure edge-based one) was also not addressed in the main body of the text for the sake of space.

In this appendix, we intend to investigate the interest in a hybrid energy for the epicardial boundary energy, but also to better understand the importance of each individual energy features used. Table A.2 presents the segmentation accuracy (using the proposed automatic initialization and applying in all 45 datasets used in Section 4.5) for different combinations of features in the proposed energy functional. The analysis addressed the introduction of the weighted formulation, the introduction of the two different energy principles for each contour (SLY and LCV), as well as the importance of the edge-based term (without it, only with it and combined with region-based term). A paired t-test was performed to assess if there was a statistical difference between the combinations tested (always between a given combination and the previous ones).

As stated in Appendix A, Table A.2 corroborates the fact that the weighted formulation is the energy feature that influences the performance most. Again, a significant increase of all measures is observed for both endo and epicardial contours (B against A). Moreover, Table A.2 definitely proves that the use of the SLY energy for the endocardium leads to a significant increase in the segmentation accuracy (C against B). Concerning the proposed hybrid epicardial energy, a significant improvement in the epicardium results are observed, which reinforces the interest in using the edge-based term in combination with the LCV energy (E against D and C). Importantly, note that, if used alone, the edge-based term lead to a decrease in the segmentation performance (D against C). Such result shows that, although CMR presents clear-sighted edges, it is not viable to use only edge information during segmentation.

In summary, based on the successive performance increases, the present analysis leads

Table A.2 - 3D Segmentation performance for endo and epicardium with multiple combinations of the proposed features in the energy functional (# = 45, $\mu \pm \sigma$).

	Energy	w_i	R/E/H	**Dice**		**APD** (mm)		**Hausdorff** (mm)	
				Endo	**Epi**	**Endo**	**Epi**	**Endo**	**Epi**
A	LCV	1.0	R	0.85 ± 0.06	0.90 ± 0.04	3.01 ± 1.03	2.90 ± 1.02	6.81 ± 1.97	6.38 ± 1.84
B	LCV	0.3	R	0.90 ± 0.05‡	0.91 ± 0.04‡	1.92 ± 0.92‡	2.43 ± 0.89‡	4.74 ± 1.94‡	5.81 ± 1.92‡
C	SLY/LCV	0.3	R	0.92 ± 0.05‡†	0.92 ± 0.04‡†	1.71 ± 0.91‡†	2.21 ± 0.88‡†	4.37 ± 2.06‡†	5.40 ± 1.96‡†
D	SLY/LCV	0.3	E	0.91 ± 0.05$^{\ddagger *}$	0.91 ± 0.04‡	1.94 ± 0.92$^{\ddagger *}$	2.53 ± 1.02$^{\ddagger *}$	4.99 ± 1.93$^{\ddagger *}$	6.05 ± 1.98$^{\ddagger *}$
E	SLY/LCV	0.3	H	0.92 ± 0.04‡†§	0.93 ± 0.03$^{\ddagger\dagger *\S}$	1.70 ± 0.89‡†§	2.06 ± 0.84$^{\ddagger\dagger *\S}$	4.34 ± 1.91‡†§	5.14 ± 1.79$^{\ddagger\dagger *\S}$

Epicardial energy term was defined as region-based only (R), edge-based only (E) or hybrid energy (H).

‡ $p < 0.05$, paired t-test against A.

† $p < 0.05$, paired t-test against B.

* $p < 0.05$, paired t-test against C.

§ $p < 0.05$, paired t-test against D.

to the conclusion that the added weights influence the result most, followed by the SLY energy used for the endocardium and the edge-based energy term in the epicardium. Moreover, it seems that the use of edge-based information results in increased accuracy, but only if used in combination with a region-based term.

Appendix C: Sensitivity Analysis

The proposed 3D segmentation algorithm has already showed its robustness and accuracy (Section 4.5 and Appendix B). Notwithstanding, the presented method requires setting several parameters, which were empirically set or defined based on *a priori* knowledge of the object of interest (Section 3.7.2). So far, the influence of these parameters in the obtained results was not studied, raising the hypothesis of eventual parameter over-tuning and consequent critical performance sensitivity to their variation.

In this appendix, the influence of the parameters variation was assessed to study the robustness and stability of the proposed methodology. To this end, the 8 more significant parameters of the algorithm were included in the analysis, namely the inner and outer region weights (w_{in} and w_{out}), the sizes of the local squared regions for statistics computation ($[n \times n]_{endo}$ and $[n \times n]_{epi}$), the threshold values for automatic stack initialization ($T_{i,endo}$ and $T_{i,epi}$), the hyperparameter α controlling the balance between the region-based and edge-based terms, and the number of points for contour discrete representation (n_{points}). The range where the parameter influence is evaluated was defined as a ±50% variation around the aforementioned chosen parameters values (Section 3.7.2). Each dataset was then segmented using the new value of one parameter while keeping the remaining ones fixed to their original value.

Regarding the chosen parameters, the first four (region weights and sizes of local regions) influence both the 2D and 3D segmentation result, therefore affecting the initial mid-ventricular segmentation and the subsequent surface delineation in the ED phase. In between, the threshold values have a direct influence in the obtained coarse stack initialization for the subsequent 3D segmentation. The parameter α affects the hybrid epicardial energy, controlling the relative importance of both region-based and edge-based terms and thus influencing the 3D segmentation. At last, the number of points for discretization, relative to the spacing chosen for the B-splines support (h), controls the surface's smoothing. Again, the 2D segmentation, stack initialization and 3D segmentation are influenced by this parameter. Please note that, due to the

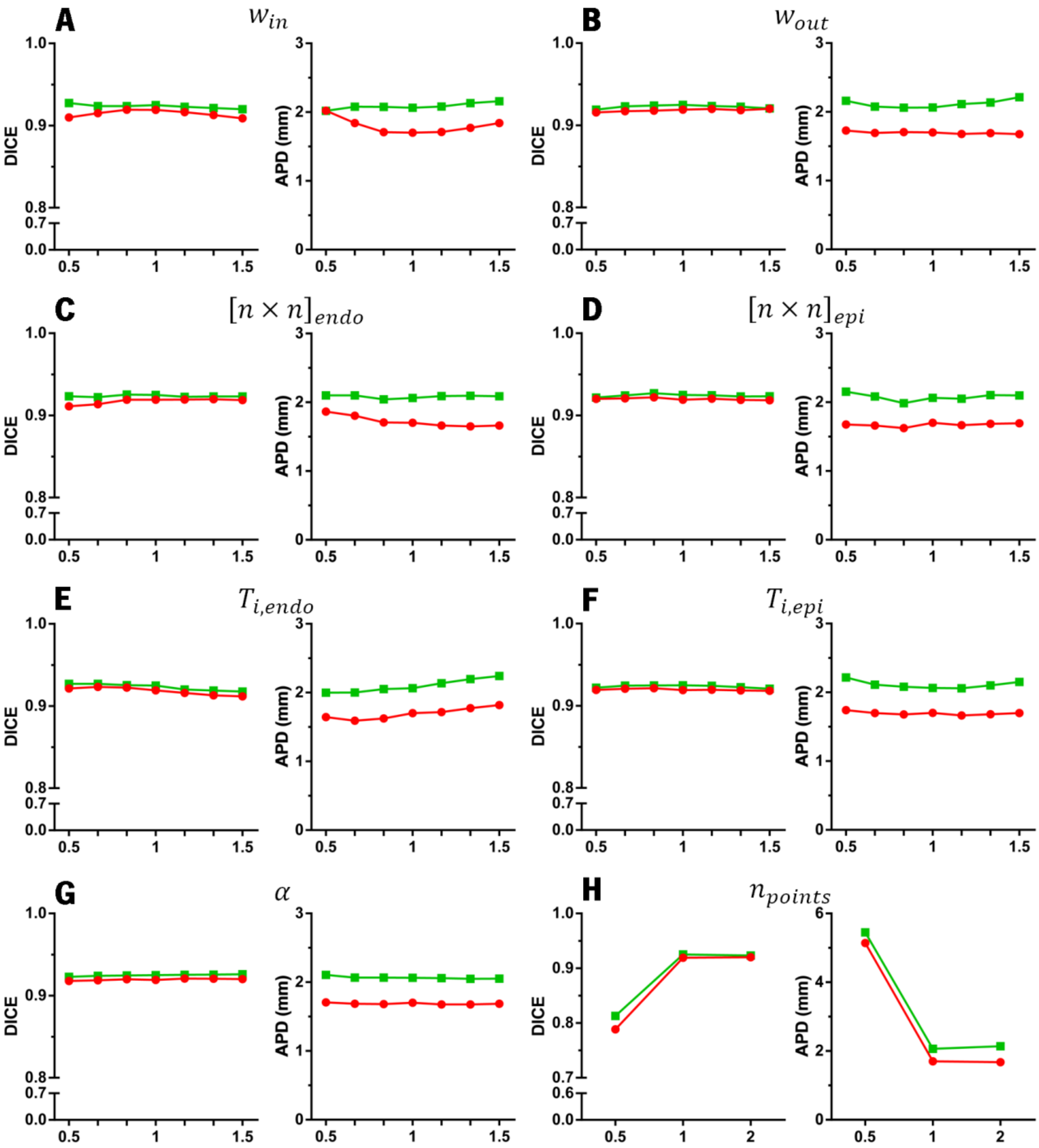

Figure A.1 - Influence of the variation of 8 parameters in the 3D segmentation performance. **(A)** and **(B)** Inner and outer region weights ([0.15; 0.45]); **(C)** and **(D)** sizes of the local region ([9×9; 21×21] and [5×5; 17×17] for endo and epicardial regions, respectively); **(E)** and **(F)** threshold for stack initialization ([92.5%; 97.5%] and [5%; 15%] for endo and epicardial thresholds, respectively); **(G)** parameter $\boldsymbol{\alpha}$ for hybrid epicardial energy ([0.025; 0.075]); and **(H)** number of points for contours discrete representation ([32; 128]), (red: endocardium; green: epicardium).

multiscale operation involved in the BEAS framework, the number of discrete contours' points should be a base-2 number. Therefore, its range was defined as a -50% to +100% variation around the initial predefined value (64 points).

Figure A.1 illustrates the influence of the variation of each parameter in the automatic 3D segmentation performance, evaluated using the average Dice metric and APD.

According to Figure A.1A, the variation of the inner region weight does not have a major impact in the segmentation performance, although there seems to be an optimal range around the chosen value. In fact, the measured variation in the accuracy was just of 1% in the average Dice metric and 0.3mm in the average APD. The same result was observed for the outer region [Figure A.1B], although with even smaller impact in the performance (0.6% and 0.15mm for Dice and APD, respectively, at the endpoints). Note that the variation of each weight also affects the other contour, due to the coupled formulation employed (Sections 3.3.1 and 3.5.1), although the performance is kept quite constant.

Regarding the size of the local region for the endocardial contour evolution [Figure A.1C], there is little influence in the outcome for the studied range. However, it was also verified that larger regions led to a small increase of the performance. This can be justified by the fact that the endocardial boundary is better defined (due to high contrast between cavity and cardiac muscle), which is favored by a larger region for higher robustness against initialization and noise. Concerning the epicardial contour, the variation of its local region size appears to have no influence [Figure A.1D], although there is a tendency for a decreased accuracy in the endpoints (note the Dice metric). Again, this result is expectable, since a larger region in the epicardium will introduce further unpredictability from the outer region, as well as a smaller region will limit the line of sight for the contours' evolution, impeding its growing and correct placement.

Concerning the threshold values for the automatic stack initialization, the analysis showed that the minimum cavity threshold ($T_{i,endo}$) is more sensitive to variations that the minimum myocardial threshold ($T_{i,epi}$) [Figure A.1E-F]. Furthermore, it was verified that smaller values for the endocardial threshold led to an increased performance. Such result may be explained by the fact that such decrease in the threshold is mimicking the purpose of the region weights (by pushing the endocardial boundary towards the myocardium).

The parameter α showed no effect on the segmentation performance [Figure A.1G]. Note, however, that even with small values it is better to have a hybrid epicardial energy than a pure region-based or edge-based one (Appendix B).

At last, the variation of the discretization showed that there is an intrinsic trade-off between a proper shape support and a smooth interface evolution. In fact, if used a small number of points (32 in the experiment), the segmented shapes are not able to capture all the shape details of the LV. For the studied case, the large spacing defined (Section 3.7.2) with such small number of points lead to segmentations close to a perfect circle, which ultimately affects both stack initialization and 3D segmentation. On the other endpoint, an increase in the number of points only resulted in a slight decrease in the accuracy. Thus, increasing the DOF of the segmented LV enables to capture finer shape details, while at the expense of a small decrease in the segmentation robustness.

Overall, the present analysis showed the robustness of the proposed framework, with only slight variations in the segmentation performance for most of the parameters analyzed. This result is of utmost importance to demonstrate its feasibility against variability.